Title
Computational Studies of Quinone Binding in Respiratory Complex I

Author
Dhananjayan, Nithin

Publication Date
2023

Peer reviewed|Thesis/dissertation

Computational Studies of Quinone Binding in Respiratory Complex I

By

NITHIN DHANANJAYAN

DISSERTATION

Submitted in partial satisfaction of the requirements for the degree of

DOCTOR OF PHILOSOPHY

in

Biophysics

in the

OFFICE OF GRADUATE STUDIES

of the

UNIVERSITY OF CALIFORNIA

DAVIS

Approved:

Professor Alexei A. Stuchebrukhov, Chair

Professor Rajiv R. P. Singh

Professor Steven M. Theg

Committee in Charge

2023

Nithin Dhananjayan

ndhananj@ucdavis.edu

ORCID iD: 0000-0003-4602-3251

Dedication

This work is dedicated to my family and loving wife without whom I would not have been able to complete this work. They have supported me through all the hardships and health issues that made completion even more difficult.

Acknowledgements

The substantive portions of this work are based on two papers already published.

The first paper is “Respiratory complex I: Bottleneck at the entrance of quinone site requires conformational change for its opening”, Panyue Wang, Nithin Dhananjayan, Muhammad A. Hagras, Alexei A. Stuchebrukhov, doi.org/10.1016/j.bbabio.2020.148326

The second paper is “Quinone binding in respiratory complex I: Going through the eye of a needle. The squeeze-in mechanism of passing the narrow entrance of the quinone site”, Nithin Dhananjayan, Panyue Wang, Igor Leontyev, Alexei A. Stuchebrukhov, doi.org/10.1007/s43630-021-00113-y

To this end I’d like to acknowledge Panyue Wang, Dr. Igor Leontyev, Assistant Professor Muhammad A. Hagras, and especially Professor Alexei A. Stuchebrukhov.

This work has been supported in part by the NIH research grant GM054052 and BSF Grant No. 2018239 A19-3374 (AAS).

I wish to also acknowledge the contribution of Dr. Kevin Demarco who took part in early studies of the subject and helped to create Fig. 3.4 of the first paper. I am grateful to Dr. James Letts and Dr. Leo Sazanov for stimulating discussion with Prof. Stuchebrukhov of complex I, and Dr. Guilherme Arantes a for valuable comment.

Abstract

This dissertation outlines research quantifying the entering and exiting the quinone reaction chamber in NADH dehydrogenase or respiratory complex I. Respiratory complex I, the first complex in the respiratory electron transport chain. The respiratory electron transport is essential for all aerobic life. The methods used to quantify the entrance and exit process are geometric modeling, steered molecular dynamics, and singular value decomposition of the process. Five structures were analyzed: bacterial, yeast, ovine mt, mice mt, and human complex I. The structures reveal an almost 30 angstrom tunnel-like chamber for quinone binding in the core part of the enzyme, at the joint between the membrane and hydrophilic arms of the enzyme. The entrance of this quinone chamber located in ND1 subunit and has an apparent bottleneck of quinone/quinol passage. The first chapter introduces complex I and how transition state theory using diffusion kinetics gives an approximate maximum for the energy of crossing the bottleneck for quinone/quinol passage. Chapter 2 introduces the techniques used to quantify the difficulty of passage as well as methods to identify modes for collective confirmational changes for bottleneck opening. Chapters 3 and 4 are reproductions of the published papers based on this work. The appendices are reproductions of the supplemental information for those two papers.

Table of Contents

1. Respiratory Complex I

NADH:ubiquinone oxidoreductase, or respiratory complex I, is a key proton-pumping enzyme involved in aerobic energy-generation inside cells[1, 2] . Structural studies[3-13] of the enzyme show molecular details that suggest possible molecular mechanisms of its redox-driven proton pumping. Complex I is an L-shaped structure with a hydrophilic domain where electron transport takes place and a membrane domain that performs proton translocation[4, 14]. In the hydrophilic domain, NADH transfers 2 electrons to flavin mononucleotide (FMN), which then transfers electrons via a chain of seven iron sulfur (FeS) clusters to a quinone molecule (Q) reducing it to a quinol[15]. The transfer of two electrons to quinone[16] is a key exergonic step, which is believed to drive local conformational changes[2, 11, 17] that transmit to the membrane domain of the complex and help to drive the proton pumping[18, 19].

In many organisms, from bacteria to human, the structure of the core part of the enzyme reveals an almost 30 angstrom tunnel-like chamber for ubiquinone binding (Q-chamber) that leads from the N-edge of the membrane up to N2 FeS cluster. Presumably, the quinone molecule migrates from the membrane into the binding chamber, diffuses up to N2 cluster, receives two electrons and migrates back – tail first, from the narrow binding cavity to the membrane[8, 18, 20-25].

In the structures for these organisms, the core part of the enzyme is very similar to bacterial enzyme; here, the entrance to Q-chamber is formed by a specific crossing of TM1, AH1, and TM6 in Nqo8 (mtND1/H E.coli) [4] and forms a narrow bottleneck that restricts the access to the Q-tunnel. The bottleneck was identified in the structure early on[4, 26], and the molecular mechanism of quinone passing the narrow bottleneck remains to be obscure, see Ref. [27]. More recent data [3, 11] indicate that both so- called “open” and “closed” states [3, 11] (not to be confused with open and closed bottleneck), the bottleneck as we identified it is about the same.

Conclusions can be drawn based on the activity of the enzyme in artificial proteo-liposomes (PL) and Km and k_{cat} of the quinones of different types in complex I [25]. Consider the efficiency parameter defined as $\kappa_{BM} = k_{cat}/K_m$. Under the condition of $k_{cat} >> k_{dis}$, the efficiency parameter is the pseudo-second-order rate constant that can be estimated as follows.

In a 3D diffusional model [28], the diffusion of quinone headgroup from the membrane interior medium to the entrance of Q-tunnel of the enzyme H-subunit as a 3D process, with$\kappa_{BM} = 4\pi r_0 \, D_q \, (N_A/10^3) P_r$. It is assumed that the binding site is a 3D half-sphere of radius r0, diffusion coefficient (for center of mass) of substrate is Dq, the factor with Avogadro number is introduced for convenient units $M^{-1}\ s^{-1}$, and CGS for r_0 and D_q. The factor P_r describes the probability that a substrate arriving at the binding site via diffusion will have a right orientation for binding. The more intricate binding site configuration is, the smaller the probability Pr.

An equivalent expression for 2D diffusion[29, 30] in the membrane plane gives qualitatively similar results. Here, $\kappa_{BM} = \frac{\pi \, D_q d_m \, (N_A/10^3) P_r}{ln(R_0/r_0)}$ where dm is the membrane width (of the order of 50 Å), and R0 is the typical distance between substrate molecules in the membrane (for [Q] = 10 mM, R_0 = 10 nm). The factor in the denominator is never too large, and realistically is in the range of 5–7 for realistic r_0 = 1 Å, or somewhat less, assuming order of magnitude values. Given these values the two expressions give qualitatively similar results for r_0=1Å. Radius r_0

characterizes the position of the center of mass of a diffusing molecule in the binding process, whereas the fitting orientation is described statistically by the probability parameter Pr.

The diffusion coefficient Dq is assumed to be in the range[21, 28] of 10−7 to 10−8 cm^2/s for the substrates of interest, but can be modified by the barrier at the bottleneck.

The above expressions describe the available data rather well. For example, for the NADH oxidation reaction of Ref. [25] both theory and experiment give $k_{cat}/K_m = 10^7$, for $r_0 = 1$ Å and Pr = 1. Similar values are obtained for AOX of Ref. [25]. However, for Q-reduction k_{cat}/K_m in Ref. [25] is much smaller and depending on the length of isoprenoid tail is in the range of 10^4 to 10^5. This significant reduction can be readily explained by an additional small factor P_r in the range of 10^{-2} to 10^{-3} or even smaller. This could be rationalized by the difficulty of passing through a narrow entrance of the Q-channel.

The barrier crossing rate by a quinone molecule at the bottleneck can be estimated from the transition state theory. The barrier crossing could be for the headgroup or one of the methyl groups of the isoprenoid tail. The rate of a single barrier crossing is given by the following expression: $k \approx \frac{D_q}{L_0^2} 10^{-\frac{V_b}{ln(10)RT}}$. The first factor (assuming a barrier width of 1 Å – 3 Å) is on the order of 108 s−1. The exponential factor should be greater than 10^{-5}, and since ln(10)RT ≈ 6 kJ/mol at room temperature, Vb ≈ 30kJ/mol or less.

Other less obvious scenarios cannot be ruled out; e.g., the case $k_{cat} << k_{dis}$. In this case $k_{cat}/K_m = \kappa_{BM} \cdot (k_{cat}/k_{dis})$, i.e. the above parameter κ_{BM} is multiplied by a small ratio (k_{cat}/k_{dis}). One could speculate that a small kcat would be expected in the Q-shuttle model due to an intricate and slow exchange of two electrons between the shuttle Q molecule and the quinones of the pool.

At the same time, the difficulty of quinone accessing the reduction catalytic site and the relatively fast reduction of the FeS chain by NADH (that provide electrons for quinone reduction) should result in a (partially) reduced state of FeS clusters in the chain, which then can serve as a buffer of electrons reducing quinone. In such conditions, the redox potential of the FeS chain would be in equilibrium with that of NADH pool, i.e. around -320 mV, and thus reduction of quinone to produce semiquinone state appears to be quite possible, despite that the redox potential of the last FeS cluster in the chain N2, which reduces quinone, by itself is much more positive [24].

1. Sazanov, L.A., A giant molecular proton pump: structure and mechanism of respiratory complex I. Nat Rev Mol Cell Biol, 2015. 16(6): p. 375-88.

2. Parey, K., et al., Respiratory complex I - structure, mechanism and evolution. Curr Opin Struct Biol, 2020. 63: p. 1-9.

3. Gutierrez-Fernandez, J., et al., Key role of quinone in the mechanism of respiratory complex I. Nat Commun, 2020. 11(1): p. 4135.

4. Baradaran, R., et al., Crystal structure of the entire respiratory complex I. Nature, 2013. 494(7438): p. 443-8.

5. Fiedorczuk, K., et al., Atomic structure of the entire mammalian mitochondrial complex I. Nature, 2016. 538(7625): p. 406-410.

6. Letts, J.A., et al., Structures of Respiratory Supercomplex I+III2 Reveal Functional and Conformational Crosstalk. Mol Cell, 2019. 75(6): p. 1131-1146 e6.

7. Zickermann, V., et al., Structural biology. Mechanistic insight from the crystal structure of mitochondrial complex I. Science, 2015. 347(6217): p. 44-9.

8. Parey, K., et al., High-resolution cryo-EM structures of respiratory complex I: Mechanism, assembly, and disease. Sci Adv, 2019. 5(12): p. eaax9484.

9. Agip, A.-N.A., et al., Mammalian respiratory complex I through the lens of cryo-EM. Annu. Rev. Biophys, 2019. 48: p. 165-184.

10. Guo, R., et al., Architecture of Human Mitochondrial Respiratory Megacomplex I2III2IV2. Cell, 2017. 170(6): p. 1247-1257 e12.

11. Kampjut, D. and L.A. Sazanov, The coupling mechanism of mammalian respiratory complex I. Science, 2020. 370(6516).

12. Bridges, H.R., et al., Structure of inhibitor-bound mammalian complex I. Nat Commun, 2020. 11(1): p. 5261.

13. Grba, D.N. and J. Hirst, Mitochondrial complex I structure reveals ordered water molecules for catalysis and proton translocation. Nat Struct Mol Biol, 2020. 27(10): p. 892-900.

14. Efremov, R.G., R. Baradaran, and L.A. Sazanov, The architecture of respiratory complex I. Nature, 2010. 465(7297): p. 441-5.

15. Sazanov, L.A. and P. Hinchliffe, Structure of the hydrophilic domain of respiratory complex I from Thermus thermophilus. Science, 2006. 311(5766): p. 1430-6.

16. Tocilescu, M.A., et al., Quinone binding and reduction by respiratory complex I. Biochim Biophys Acta, 2010. 1797(12): p. 1883-90.

17. Cabrera-Orefice, A., et al., Locking loop movement in the ubiquinone pocket of complex I disengages the proton pumps. Nat Commun, 2018. 9(1): p. 4500.

18. Stuchebrukhov, A.A., Redox-Driven Proton Pumps of the Respiratory Chain. Biophys J, 2018. 115(5): p. 830-840.

19. Stuchebrukhov, A.A., Kinetics and Efficiency of Energy-Transducing Enzymes. J Phys Chem B, 2019. 123(44): p. 9456-9465.

20. Kaila, V.R.I., Long-range proton-coupled electron transfer in biological energy conversion: towards mechanistic understanding of respiratory complex I. J R Soc Interface, 2018. 15(141).

21. Warnau, J., et al., Redox-coupled quinone dynamics in the respiratory complex I. Proc Natl Acad Sci U S A, 2018. 115(36): p. E8413-E8420.

22. Wikstrom, M., et al., New perspectives on proton pumping in cellular respiration. Chem Rev, 2015. 115(5): p. 2196-221.

23. Sharma, V., et al., Proton-coupled electron transfer and the role of water molecules in proton pumping by cytochrome c oxidase. Proc Natl Acad Sci U S A, 2015. 112(7): p. 2040-5.

24. Hagras, M.A. and A.A. Stuchebrukhov, Concerted Two-Electron Reduction of Ubiquinone in Respiratory Complex I. J Phys Chem B, 2019. 123(25): p. 5265-5273.

25. Fedor, J.G., et al., Correlating kinetic and structural data on ubiquinone binding and reduction by respiratory complex I. Proc Natl Acad Sci U S A, 2017. 114(48): p. 12737-12742.

26. Agip, A.A., et al., Cryo-EM structures of complex I from mouse heart mitochondria in two biochemically defined states. Nat Struct Mol Biol, 2018. 25(7): p. 548-556.

27. Uno, S., et al., Oversized ubiquinones as molecular probes for structural dynamics of the ubiquinone reaction site in mitochondrial respiratory complex I. Journal of Biological Chemistry, 2020. 295(8): p. 2449-2463.

28. Stuchebrukhov, A., et al., Kinetic advantage of forming respiratory supercomplexes. Biochimica Et Biophysica Acta (BBA)-Bioenergetics, 2020. 1861(7): p. 148193.

29. Georgievskii, Y., E.S. Medvedev, and A.A. Stuchebrukhov, Proton transport via the membrane surface. Biophysical journal, 2002. 82(6): p. 2833-2846.

30. Georgievskii, Y., E.S. Medvedev, and A.A. Stuchebrukhov, Proton transport via coupled surface and bulk diffusion. The Journal of chemical physics, 2002. 116(4): p. 1692-1699.

2. Methods Used

This chapter outlines the methods used in each subsequent chapters which are reproductions of the two published papers. The methods outlined are the ones that I contributed to and have more detail on some parts of the methodology and were given in the papers.

2.1 Geometry Analysis

In order to characterize the internal geometry of the ubiquinone cavity, a specific computational tool was developed to calculate the precise cross-sectional geometry of the entire reaction chamber. The algorithm first calculates a spline along the length of the cavity, and then at each point along the spline a sweep of cross-sections is probed. The full set of cross-sections along this spline provides a detailed geometrical characteristic of the entire ubiquinone reaction cavity.

In order to probe the energetics of the quinone chamber, the configurational entropy was estimated by the difference in the area between the cross-section of the ubiquinone head group1 and that of the Q-chamber along the binding coordinate. The difference between these areas was converted to a free energy entropy term and, together with the hydropathy analysis[1, 2]. This initial analysis formally results in the infinitely high barrier at the bottleneck. The static geometry of the entrance is simply too small to accommodate the head group of the ubiquinone. The menaquinone group gives similar results, i.e. the bottleneck is too small.

This initial analysis was supplemented with the analysis of variations due to B-factors. To this end, approximately 10 thousand structures of the bottleneck were generated with uncertainties given by the B-factors[3] of the residues making up the bottleneck. The upper bound uncertainty was calculated using the standard deviations taken directly from the B-factors (the actual uncertainty is smaller, and for a given resolution of 3.1 Å is about half of the upper bound). The uncertainty in the structure geometry adds about 1 Å in the boundary of the cross sections, and still is not enough for a passage of the headgroup of ubiquinone through the bottleneck.

The key finding of the geometry analysis is that the head group of quinone cannot pass through the static bottleneck without some elastic expansion or change in its conformation.

2.2 Steered Molecular Dynamics

Four structures were MD-probed: bacterial T. thermophilus[3], yeast Y. lipolytica [4], and two mammalian structures - ovine[5], and human[6, 7]. For mice[8] structure, in both so-called Active and Deactive states, the entrance to the Q-chamber is too small by visual analyses and was not further probed in MD simulations. MD simulations used Gromacs [9] simulation package with CHARMM36 forcefield[10].

The potential energy components including bond energies, dihedral energies, Lennard-Jones energies, and Coulomb energies, as evaluated by the Gromacs MD simulation package, were evaluated along the Q-pulling trajectories for the residues representing the bottleneck.

2.2.1 Pulling Simulations with system embedded in membrane

2.2.1.1 Constriction of the protein lipid structure

The protein lipid structure was constructed using charm GUI[11-13] using 4HEA (keeping chain D, F, G, I and P), POPC lipid (315 upper leaflet, 300 lower leaflet). Pre-MD equilibration was done using energy minimization, followed by NVT equilibration at 310 Kelvin, then NPT equilibration at 310 Kelvin and 1 bar. The Berendsen[14] thermostat and the Berendsen barostat were used to maintain temperature and pressure.

2.2.1.2 Incorporating Ubiquinone (Q10)

At this point, Chimera [15] was used to place Ubiquinone near the entrance of Complex I. After the structure was built, using Gromacs[9], the system was energy minimized, temperature and pressure equilibrated with the CHARMM36 forcefield [10] was used and Swiss Param generated force field[16] for Q10. During these equilibration steps the protein atoms were restrained to preserve as close to the crystal structure as possible.

2.2.1.3 Getting Q10 into the reaction chamber without distorting the protein

In order to get the initial position, keeping constraints in place Q10 was pulled into Complex I. The system was initialized to 310K and 1 bar during equilibration, and subsequent pulling in of Q10 under protein restraints. The restraints placed on the atoms of the protein for trajectory 1 and trajectory 2 were a mix of 20 and 40 KJ mol^{-1} A^{-2}. These were the force constants used by CHARMM GUI for restraining the protein while building the lipid membrane around it. For trajectory 3, the force constants used on the atoms of the protein during equilibration and pulling in of Q10 were all 40 KJ mol^{-1} A^{-2}. All the simulations were done under periodic boundary conditions and isotropic pressure coupling.

2.2.1.4 Pulling Q10 out of the reaction chamber for analysis

The production simulations then pulled the Q10 out without restraints. Three trajectories were chosen to analyze. The barostat and thermostat were maintained while pulling the quinone through the bottleneck. The Coulomb and LJ interactions have a cutoff radius of 1.2 nm. The three trajectories were generated using GROMACS 2020. The pulling rate of the three trajectories are 0.01 nm/ps, 0.01 nm/ps and 0.02 nm/ps respectively. The simulation time is 300 ps, 300 ps and 180 ps respectively. The pulling force constant for all three trajectories is 2500 kJ/mol/nm^2. The system was kept at 310K and 1 bar while the Q10 molecule was pulled out of Complex I. The restraints were removed prior to pulling out. The Q10 was pulled out using direction pulling along a vector perpendicular to the plane bottleneck by a carbon on the tail with a force of 25 KJ mol^{-1} A^{-2}. For trajectory 3, the protein was allowed to relax at 310K and 1 bar before the Q10 was pulled out.

2.2.1.5 Analyzing energies of Associated with the bottleneck in pulling trajectories

Gromacs has a means of rerunning the simulation to look at energies of specified groups using the positions of the atoms of that group from a trajectory of a previous simulation. The potential energy and its components are modeled by a topology specified for the particular group of atoms. The potential energy components include bond energies, dihedral energies, Lennard-Jones

energies, and Coulomb energies. The residues used to represent the bottleneck consists of 10 residues (142 atoms) are pictured schematically here:

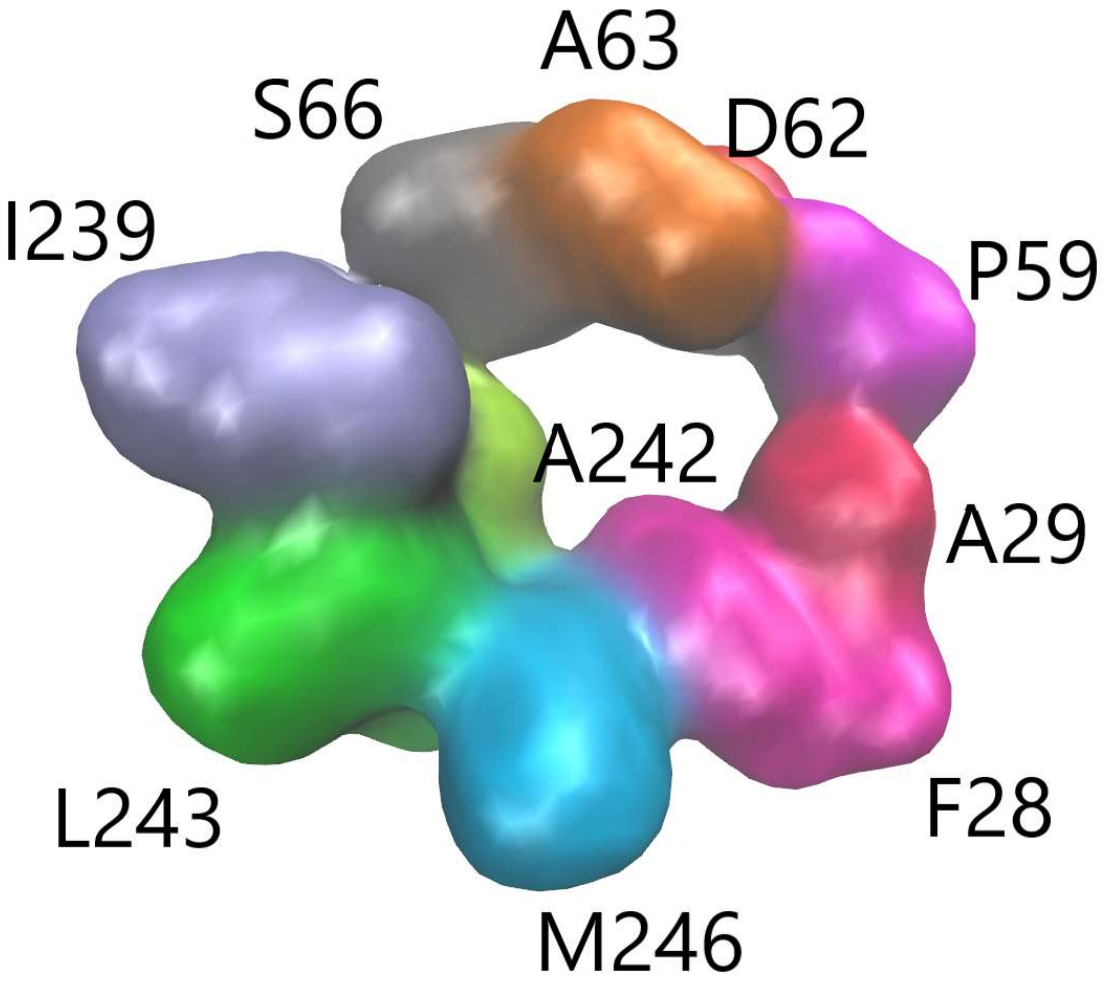

Figure 2.1: The 10 residues of the bottleneck rendered using surface rendering in VMD[17] and colored by residue.

The topology was generated using pdb2gmx based on the CHARMM36 forcefield with one minor modification. The utility added an oxygen to the C terminus of MET 246 that needed to be removed, along with any references to that oxygen in bonds and dihedrals.

The pdb2gmx forcefield was modified as follows:

Changed from	To
141 CC 246 MET C 141 0.34 12.011	141 CC 246 MET C 141 0.51 12.011
142 OC 246 MET OT1 142 - 0.67 15.9994	142 OC 246 MET O 142 - 0.51 15.9994

143 OC 246 MET OT2 143 - 0.67 15.9994	

Table 2.1 Modification of pdb2gmx generated topology

2.2.2 Pulling Simulations with restricted system

To improve statistics, focused MD simulations on a restricted system that involved only the residues of the bottleneck were used. In this case the simulation box was filled with an artificial hydrophobic (LJ)medium consisting of water with switched-off charges. Typically, the Q was pulled with a speed of 0.1 Å per ps; this is about ten times slower than the rate of water molecule diffusion in bulk water ($D_w = 10^{-5}$ cm^2/s)[18]. In a focused MD the pulling speed was further reduced by a factor of ten to simulate adiabatic conditions for free energy evaluation.

The models of bottlenecks were taken from the crystal structures and neutral charge states chosen for all residues so that the bottleneck had zero net charge. The bottleneck models were placed into artificial hydrophobic media of LJ spheres, equivalent to tip3p water with all charges set to zero. The system was then energy minimized with the bottleneck model positions restrained with 2500 KJ/mol/nm^2. The pulling simulations were then done with NVT using stochastic dynamics at 310 Kelvin.

2.2.2.1 UQ/DQ/MQ Models

The ubiquinone model UQ10 was generated using Swiss Param. The DQ/MQ and shorter tail and reduced analogues were all based on this model. To create UQ1 and UQ3 models, the UQ10 model was shortened by cutting of the tails to have either 1 or 3 isoprenoids, and a hydrogen placed where the tail was cut. The reduced models were created by taking the oxidized models and converting the ketones to enols in the headgroups. Specifically, hydrogens were bonded to the oxygens with bond length 0.096nm and strength of other single bonds in the forcefield, a bond angle of 108 degrees and force constant of 543.920 KJ/mol/rad^2. For each hydrogen, 2 proper dihedral angles (corresponding to the 2 carbons connected to the enol carbon) were added with dihedral angles of 180 degrees (trans), force constant of 4.142 KJ/mol and multiplicity of 2. Carbon-carbon single and double bonds in the ring of the head group were then shifted to match the standard ubiquinol structure using existing carbon-carbon single and double bond parameters in the headgroup. The MQ models were created by taking the corresponding UQ models, removing the methoxy groups and adding a ring corresponding to the head group of the standard menaquinone structure using the parameters that already existed in the model for similar bonds, angles, and dihedrals. The DQ models were made from the corresponding UQ models, replacing the isoprenoid tails with a simple saturated hydrocarbon chain, once again using the parameters that already existed in the model for corresponding bonds, angles, and dihedrals.

Ligand	Bottleneck	Sim. Length	# runs
UQ1	t. Thermophilus	1.5 ns	53
UQ1H2	t. Thermophilus	1.5 ns	59

UQ3-tail	t. Thermophilus	1 ns	29
UQ3	ovine	1.5 ns	15
UQ3	human	2 ns	15
UQ3	y. Lipolytica	2 ns	15
UQ3H2	y. Lipolytica	2 ns	15
MQ1	t. Thermophilus	1.5 ns	31
MQ1H2	t. Thermophilus	1.5 ns	30
DQ1	t. Thermophilus	1.5 ns	31
DQ1H2	t. Thermophilus	1.5 ns	31

Table 2.2: List of all pulling simulations through simplified bottleneck in hydrophobic media. Data shown to demonstrate statistical averaging over trajectories used in free energy calculations.

2.2.2.2 Thermodynamic work to cross the bottleneck

The Helmholtz work (or Helmholtz free energy, W) to cross the bottleneck is defined by the average force needed to pull the quinone through the bottleneck along the pulling coordinate λ:

$$\left(\frac{\partial W}{\partial \lambda}\right)_T = < F >$$

$$\Delta W = \int_{(i)}^{(f)} < F > d\,\lambda$$

The above relations assume a reversible or quasi-equilibrium (in practice very slow) change of the system. For this reason, the pulling rate was set to 0.01 Å per ps, which is about hundred times slower than the diffusion rate of water($D_w = 10^{-5}$ cm^2/s)[18]. The force <F> is assumed to be averaged over thermal fluctuations (for a given λ, and over a set of initial conditions in the initial state (i)). In our calculations, the pulling force $F(t)$ is measured along the MD pulling trajectory and averaged locally (moving average) over a short interval of 100 ps, for a typical pulling trajectory of some 1500ps. In addition, the averaging was done over some 30-60 pulling trajectories with different initial conditions. The Helmholtz work ΔW gives the energy barrier along the trajectory.

When the final state of quinone (f) is defined as a region at the top of the barrier, i.e. the position of the quinone head group inside the bottleneck, and the initial state (i) is a region inside the Q-chamber, the work described above is related to both decrease of entropy (as in isothermal contraction of gas) and increase of potential (elastic) energy of the system due to possible structure adjustment of putting the oversized quinone head group into a relatively narrow bottleneck of the cavity entrance.

In addition, the so-called Jarzynski Averaged (JA) work[19] was calculated using:

$$< \Delta W >= -RTln\left(e^{-\frac{\Delta W}{RT}}\right)$$

where Δw is the work for a given pulling trajectory, and the averaging (indicated by the brackets) is assumed over different trajectories. If the pulling work were calculated for a non-equilibrium process at constant energy, instead of constant temperature and quasi-equilibrium process considered here, the Jarzynski equality (JE) would give the proper free energy change. The conditions in the pulling simulations are different from what is assumed in the JE, and thus the above relation is not directly applicable; however, it is useful to consider this type of averaging as it emphasizes trajectories with minimal work and thus selects (or filters for) the "optimal" trajectories. JA is sensitive to qualitative changes along the trajectory, such as the entrance of the headgroup into the bottleneck or the passage of individual methyl groups of isoprenoid tail of ubiquinone, which show up as small bumps on the JA curves.

2.3 Principal Component Analysis

In order to gain insights into the collective modes, principal component analysis was used for chapter 4. Improvements for future work include constraining portions of subunit H to better reflect how the H subunit would be in the full complex. Nevertheless, it was useful to see how the subunit responds by itself.

The methodology used for principal component analysis(PCA) based on [20]. Although PCA does not require harmonicity, interpreting the eigenvectors as modes of coupled harmonic oscillations is interesting. Additionally, PCA is known to assume a linear relationships between variables and suffer from limited sampling. However, the interpretation procedure follows. This is more detail than is provided in Chapter 4.

2.3.1 From Trajectory to Modes

Denote the cartesian coordinates $x_i(n)$ where the index i accounts for all three dimensions of each atom, and n is indexes the snapshot of the trajectory at a particular time.

Let $< x_i >= \frac{1}{N}\sum_{n=0}^{N} x_i(n)$ with a total of N snapshots. If the motion is stationary, then we can subtract the averages to get an updated set of coordinates $\tilde{x_i}(n) = x_i(n) - < x_i >$. Then the covariance matrix is calculated $M_{ij} =< \tilde{x_i}\tilde{x_j} >$. If we express each $\tilde{x_i} = \sum_\lambda S_{i\lambda}Q_\lambda$ as a linear combination of collective coordinates Q_λ. $M_{ij} =< \tilde{x_i}\tilde{x_j} >= \sum_{\lambda,\mu} S_{i\lambda} < Q_\lambda Q_u > {S_{\mu j}}^T$.

Define $D_{\lambda\mu} =< Q_\lambda Q_u >$. Note also that ${S_{\mu j}}^T = S_{j\mu}$. Since M is a symmetric matrix with real entries, it can be diagonalized with $M = SDS^T$, such that the column vectors of S are othronormal. D is diagonal. This means through diagonalization we can choose Q_λ such that $D_{\lambda\mu} = \sum_\mu \delta_{\lambda\mu} < Q_\lambda^2 >$.

In addition, because the column vectors of S are orthonormal, we have $\sum_i (S_{i\lambda})^2 = 1$. We can ascribe a "participation" of coordinate x_i in Q_λ to be $P_{i\lambda} = (S_{i\lambda})^2$. The participation of an atom in a mode would then be the sum of the participations for the x, y, and z coordinates in that mode.

2.3.1 Interpretation of Modes

Looking at the Q_λ as if they were normal modes, we have $Q_\lambda = Acos(\omega_\lambda t)$. The frequency of this mode can be found from $\omega_\lambda = \sqrt{\frac{k_\lambda}{M_\lambda}}$.

The effective spring constant can be found by the average potential energy $k_\lambda = \frac{k_B T}{<Q_\lambda^2>}$.

The effective mass, M_λ, can be found using the average kinetic energy. First note, that $\dot{\tilde{x}}_\iota = \sum_\lambda S_{i\lambda} \dot{Q}_\lambda$ which means since D is diagonal,

$$\dot{\tilde{x}}_\iota^{\,2} = \left(\sum_\lambda S_{i\lambda}\dot{Q}_\lambda\right)\left(\sum_\mu S_{i\mu}\dot{Q}_\mu\right) = \sum_{\lambda,\mu} S_{i\lambda}S_{i\mu}\dot{Q}_\lambda\dot{Q}_\mu = \sum_\lambda {S_{i\lambda}}^2 \dot{Q}_\lambda^{\,2}$$

Now, rewriting average kinetic energy in the form of an effective mass for each mode:

$$< \sum_i \frac{m_i}{2} \dot{\tilde{x}}_\iota^{\,2} > = \sum_{i,\lambda} \frac{m_i}{2} {S_{i\lambda}}^2 < \dot{Q}_\lambda^2 > = \sum_\lambda \frac{M_\lambda}{2} < \dot{Q}_\lambda^2 >$$

So, $M_\lambda = \sum_i m_i {S_{i\lambda}}^2$.

Using the frequencies we get a timescales for these low frequency modes to be $T_\lambda = \frac{2\pi}{\omega_\lambda}$.

1. Berka, K., et al., MOLEonline 2.0: interactive web-based analysis of biomacromolecular channels. Nucleic Acids Res, 2012. 40(Web Server issue): p. W222-7.

2. Kyte, J. and R.F. Doolittle, A simple method for displaying the hydropathic character of a protein. Journal of molecular biology, 1982. 157(1): p. 105-132.

3. Baradaran, R., et al., Crystal structure of the entire respiratory complex I. Nature, 2013. 494(7438): p. 443-448.

4. Parey, K., et al., High-resolution cryo-EM structures of respiratory complex I: Mechanism, assembly, and disease. Science advances, 2019. 5(12): p. eaax9484.

5. Fiedorczuk, K., et al., Atomic structure of the entire mammalian mitochondrial complex I. Nature, 2016. 538(7625): p. 406-410.

6. Guo, R., et al., Architecture of human mitochondrial respiratory megacomplex I2III2IV2. Cell, 2017. 170(6): p. 1247-1257. e12.

7. Gu, J., M. Wu, and M. Yang, Cryo-EM structure of human respiratory complex I. PDB, 2017.

8. Agip, A.-N.A., et al., Mammalian respiratory complex I through the lens of cryo-EM. Annu. Rev. Biophys, 2019. 48: p. 165-184.

9. Abraham, M.J., et al., GROMACS: High performance molecular simulations through multi-level parallelism from laptops to supercomputers. SoftwareX, 2015. 1: p. 19-25.

10. Huang, J. and A.D. MacKerell, Jr., CHARMM36 all-atom additive protein force field: validation based on comparison to NMR data. J Comput Chem, 2013. 34(25): p. 2135-45.

11. Jo, S., et al., CHARMM-GUI: a web-based graphical user interface for CHARMM. J Comput Chem, 2008. 29(11): p. 1859-65.

12. Darden, T., D. York, and L. Pedersen, Particle mesh Ewald: An N· log (N) method for Ewald sums in large systems. The Journal of chemical physics, 1993. 98(12): p. 10089-10092.

13. Brooks, B.R., et al., CHARMM: the biomolecular simulation program. J Comput Chem, 2009. 30(10): p. 1545-614.

14. Berendsen, H.J., et al., Molecular dynamics with coupling to an external bath. The Journal of chemical physics, 1984. 81(8): p. 3684-3690.

15. Pettersen, E.F., et al., UCSF Chimera--a visualization system for exploratory research and analysis. J Comput Chem, 2004. 25(13): p. 1605-12.

16. Zoete, V., et al., SwissParam: a fast force field generation tool for small organic molecules. J Comput Chem, 2011. 32(11): p. 2359-68.

17. Humphrey, W., A. Dalke, and K. Schulten, VMD: visual molecular dynamics. Journal of molecular graphics, 1996. 14(1): p. 33-38.

18. Stuchebrukhov, A., et al., Kinetic advantage of forming respiratory supercomplexes. Biochim Biophys Acta Bioenerg, 2020. 1861(7): p. 148193.

19. Liphardt, J., et al., Equilibrium information from nonequilibrium measurements in an experimental test of Jarzynski's equality. Science, 2002. 296(5574): p. 1832-5.

20. David, C.C. and D.J. Jacobs, Principal component analysis: a method for determining the essential dynamics of proteins. Methods Mol Biol, 2014. 1084: p. 193-226.

3. First paper on the narrow bottleneck

This chapter is a reproduction of prior work published. “Respiratory complex I: Bottleneck at the entrance of quinone site requires conformational change for its opening”, Panyue Wang, Nithin Dhananjayan, Muhammad A. Hagras, Alexei A. Stuchebrukhov, The supplemental information will also be provided in Appendix A of the dissertation.

Abstract

The structure of the entire respiratory complex I is now known at reasonably high resolution for many species –bacteria, yeast, and several mammals, including human. The structure reveals an almost 30 angstrom tunnel-like chamber for ubiquinone binding in the core part of the enzyme, at the joint between the membrane and hydrophilic arms of the enzyme. Here we characterize the geometric bottleneck forming the entrance of the quinone reaction chamber. Computer simulations of quinone/quinol passage through the bottleneck suggest that in all structures available, from bacterial to human, this bottleneck is too narrow for the quinone or quinol to pass and that a conformational change is required to open the channel. Moreover, the bottleneck is too narrow even for isoprenoid tail free passage. The closed structure can be an artifact of the crystallization packing forces, low temperature, or other unnatural conditions occurring in the structural data acquisition procedure that affect this flexible part of the enzyme. Two of the helices forming the bottleneck are in direct contact with the subunit (ND3) that was recently demonstrated to be involved in conformational changes during the redox proton pumping cycle, which indicates flexibility of that part of the enzyme. We conclude that the published structures are all locked in the unfunctional states and do not represent correctly the functional enzyme; we discuss possible ways to open the structure in the context of possible mechanisms of the enzyme.

3.1 Introduction

NADH:ubiquinone oxidoreductase, also known as respiratory complex I, is the first enzyme of the respiratory chain and a key component of energy generation machinery in the cell [1]. It couples the electron transfer from NADH to a quinone molecule to the pumping of protons across the mitochondrial or bacterial membrane, thus generating the proton-motive force required to drive ATP synthesis and active membrane transport.

Recent structural studies [2–8] have revealed important molecular details suggesting possible mechanisms of the enzyme functionality; however, the structure also poses new questions. One such question concerning the ubiquinone-binding cavity will be discussed in this paper. Complex I is an L-shaped structure, with a hydrophilic domain where the electron transport occurs, and a membrane domain that performs the proton translocation [2,9]. In the hydrophilic domain, NADH transfers 2 electrons to flavin mononucleotide (FMN), which then transfers electrons to a chain of iron sulfur (FeS) clusters and then to the quinone molecule (Q), reducing it to a quinol [10]. The transfer of electrons to quinone [11] is a key exergonic step, which is believed to drive the conformational changes [12] that transmit to the membrane domain of the complex where the protons are pumped. The proton coupling between the half channels of anti-porter subunits of the membrane domain was suggested to happen through key Lys and Glu residues in the middle of the membrane [2,13], which play a role of Proton Loading

Sites (PLS), analogous to PLS of cytochrome c oxidase complex IV, with alternative access from both sides of the membrane.

The presumed conformational change should operate in such a way as to change access to PLS and regulate their pKa's in a concerted manner [14,15]. Theoretical analysis suggests that there should be two independent parameters that control the status of a proton pump (access and pKa of PLS).

In all organisms, from bacteria to human, the structure of the core part of the enzyme reveals an almost 30 angstrom tunnel-like chamber for ubiquinone binding (Q-chamber) that leads from the N-edge of the membrane up to the N2 FeS cluster. Presumably, the quinone molecule migrates from the membrane into the binding chamber, diffuses up to the N2 cluster, receives two electrons and two protons and migrates back – tail first, from the binding cavity to the membrane. The round trip, including the search of the entrance of the quinone cavity, occurs within the enzyme turnover timescale, i.e. a few ms. It is not yet clear what are the driving forces for such a process, but computer simulations provide some insights into these questions [6,14,16–21].

Thus, recent simulations have revealed two binding sites inside the quinone cavity of bacterial T. thermophilus structure and described the energy profile along the tunnel and estimated diffusion coefficient of the order of 10^{-8} cm^2/s, Ref. [17]. Recent structure [6] shows one quinone molecule bound inside the cavity at the position of the head group close to that predicted by theory.

Here we characterize a geometric bottleneck at the entrance of the quinone reaction chamber in complex I from five organisms: bacterial T. thermophilus [2], yeast Y. lipolytica [6], and three mammalian structures, ovine [3], mice [7], and human [8,22]. The core part of the enzyme in all organisms is very similar to the bacterial enzyme; here, the entrance to Q-chamber is formed by a specific crossing of TM1, AH1, and TM6 in Nqo8, and the bottleneck is located in the vicinity of site 2′ of Ref. [17], toward the membrane. In fact, it is this bottleneck that forms the real entrance to the Q-tunnel, providing access to sites 2 and 2′ and the rest of the cavity with sites 1 and 1′ of Ref. [17] (see SI Fig. A0).

The bottleneck was identified in the structure early on [2,23], and it was speculated that conformational changes are needed to open it. Recently the issue was brought up again in Ref. [24]. Qualitatively, the narrow entry point appears to be too small to accommodate the head group of either ubiquinol or ubiquinone. Here we characterize the entrance bottleneck more rigorously. First, we provide detailed geometry analysis; second, we use Molecular Dynamics (MD) simulations to quantify the energy barrier formed by the narrow bottleneck. The structures of five organisms were analyzed, bacterial, yeast, and three mammalian structures, including human.

Computer simulations of quinone/quinol passage through the bottleneck suggest that in all structures available, from bacterial to human, this bottleneck is too narrow for the quinone or quinol to pass - both for the head group and even for the isoprenoid tail, and that a conformational change is required to open the channel. We conclude that the closed structure is an artifact of the crystallization packing forces, low temperature, or other specific conditions occurring in the structural data acquisition procedure that affect this flexible part of the enzyme. Two of the helices forming the bottleneck are in direct contact with the subunit (ND3) that was

recently demonstrated to be involved in conformational changes in the proton pumping cycle [12], which indicates flexibility of that part of the enzyme. We conclude that the published structures are all locked in the unfunctional states and do not correctly represent the functional enzyme. We then discuss possible ways to open the structure and predict some structural changes that may occur in the functional state.

Even though the conformational opening of the quinone chamber is clearly needed, it is not clear to what extent the structure is opened in the functional enzyme. One possibility is that it would allow free passage only of the tail but not the headgroup, and thus, one quinone molecule could be always locked inside of the Q-chamber, suggesting a piston-like mechanism proposed recently, Ref. [17]; however, our analysis indicates this scenario to be unlikely. The opening of the bottleneck to an extent so as to allow only isoprenoid tail free passage but not the head group of the quinone appears to be unlikely. This indicates a need for a major opening of the structure to avoid additional energy barriers for the isoprenoid tail passage.

However, based on the analysis of the literature kinetic data [21], we also conclude that when the structure is in its native open functional state, the entrance still remains narrow. Moreover, as the exit of the reduced quinone requires more space, as indicated by our simulations, it may still require additional flexibility transition to allow for the reduced quinone to exit, which may be part of the catalytic cycle.

The plan of the paper is as follows. First the bottleneck itself is characterized geometrically; we then present results of molecular dynamics simulations and conclude with the discussion of the results.

3.2 Methods and Results

Overall, five structures were analyzed: bacterial T. thermophilus [2], yeast Y. lipolytica [6], and three mammalian structures, ovine [3], mice [7], and human [8,22]. As the core part of the enzyme of 14 subunits is almost identical or very similar (in the part relevant to this discussion) to bacterial complex, and the results are qualitatively similar for all structures analyzed, here we first describe in detail the results for the bacterial structure, or use it to illustrate the methods and results for the whole set; we then comment on the other structures. Additional results are given in the Supplementary Information file, SI.

For the analysis of bacterial complex I, we use the crystal structure T. thermophilus, 4HEA [2] with highest resolution of 3.1 Å. All other enzyme structures were obtained with cryo-EM, which naturally assume different conditions of structure data acquisition; this point will be included in the following discussion.

The quinone binding cavity, the entrance, and the amino acids comprising the orifice of the entrance of quinone, i.e. the bottleneck, are shown in Figs. 3.1 and 3.2.

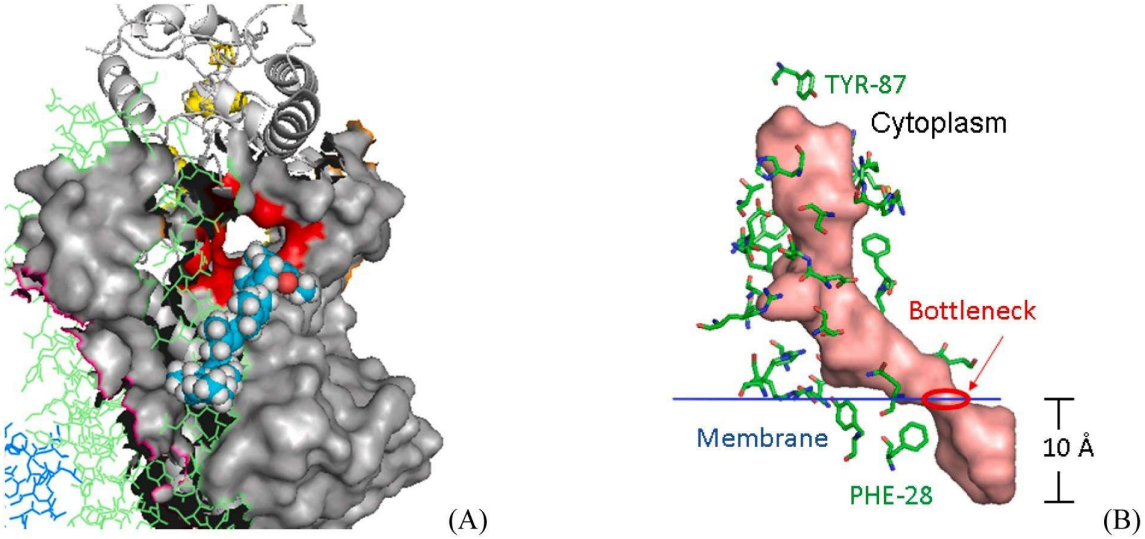

Fig. 3.1. (A) The entrance into the Q-binding cavity, shown in red; gray surface refers to subunit ND1(H), green lines refer to subunit A, and cyan spheres refer to quinone, from MD simulations described in the text. (B) The quinone binding cavity with the location of the bottleneck is shown with respect to the membrane surface. The residues Tyr-87 and Phe-28 are discussed in the text.

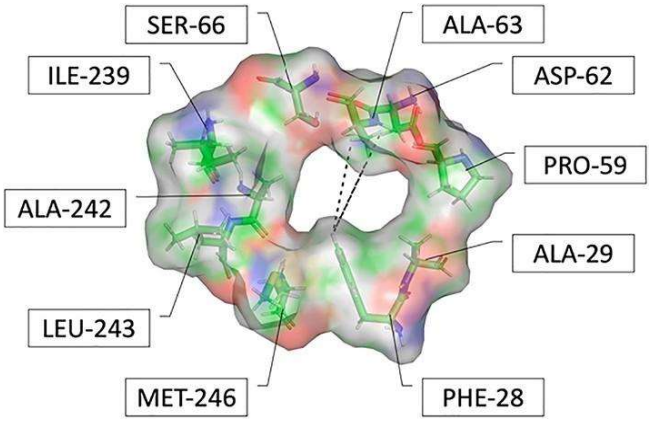

Fig. 3.2. 10 residues that form the entrance of complex I quinone cavity in bacterial enzyme. The shortest axis discussed in the text is indicated by dashed lines

The bottleneck, Fig. 3.2, is localized at the crossing formed by three helices: Nqo8_TM1, Nqo8_AH1, and Nqo8_TM6 [2], see also Supplementary Fig. A5.

Recently, [16,17], the energy profile inside of the bacterial cavity was characterized using MD methods. These studies refer mainly to a region entirely behind the bottleneck shown in Fig. 3.2. Fig. A0 shows the bottleneck and the region behind it – so-called sites 2 and 2′. According to Refs. [16,17] the region just behind the bottleneck has a dip in energy profile of some 8 kcal/mol. A key point of the present paper is that there is a bottleneck in accessing the binding sites 2 and 2′ and the rest of the cavity.

Recently, Zickermann et al. [6] have determined the structure of complex I from aerobic yeast Y. lipolytica by cryo-EM at 3.2-A resolution, and a ubiquinone molecule was identified in the Q-tunnel. The binding position of the head group of Q corresponds roughly to

a region of sites 2 and 2′ of Ref. [17] behind the bottleneck entrance. Here we show that without conformational change, the barrier of the bottleneck separating the Q-tunnel from the membrane part prevents the exit of the quinone molecule from the Q-tunnel.

In the following, we first characterize the geometry of the bottleneck; then MD simulations are used to probe the energy barrier associated with the passage of the bottleneck.

3.2.1 Geometry Analysis

In order to characterize the internal geometry of the ubiquinone cavity, a specific computational tool was developed to calculate the precise cross-sectional geometry of the entire reaction chamber. The algorithm first calculates a spline along the length of the cavity, and then at each point along the spline a sweep of cross-sections is probed. The full set of cross-sections along this spline, shown in SI Fig. A1, provides a detailed geometrical characteristic of the entire ubiquinone reaction cavity. Fig. A1 clearly shows the minimum cross-section at the bottleneck. A simple initial geometry analysis indicates that the cross section of quinone does not fit that of the bottleneck, see Fig. A2.

In order to probe the energetics of the quinone chamber, the configurational entropy was estimated by the difference in the area be- tween the cross-section of the ubiquinone head group1 and that of the Q-chamber along the binding coordinate. The difference between these areas was converted to a free energy entropy term and, together with the hydropathy analysis [25,26], is shown in Fig. A3. This initial analysis formally results in the infinitely high barrier at the bottleneck. The static geometry of the entrance is simply too small to accommodate the head group of the ubiquinone. The menaquinone group gives similar results, i.e. the bottleneck is too small.

This initial analysis was supplemented with the analysis of variations due to B-factors. To this end, approximately 10 thousand structures of the bottleneck (Fig. 3.2) were generated with uncertainties given by the B-factors [2] of the residues making up the bottleneck. The upper bound uncertainty was calculated using the standard deviations taken directly from the B-factors (the actual uncertainty is smaller, and for a given resolution of 3.1 Å is about half of the upper bound). The uncertainty in the structure geometry adds about 1 Å in the boundary of the cross sections (see SI Fig. A12), and still is not enough for a passage of the headgroup of ubiquinone through the bottleneck.

The key finding of the geometry analysis is that the head group of quinone cannot pass through the static bottleneck without some elastic expansion or change in its conformation.

Next, we included flexibility of the opening, and using MD methods studied the energetics of the passage of quinone through the bottleneck, Fig. 3.3.

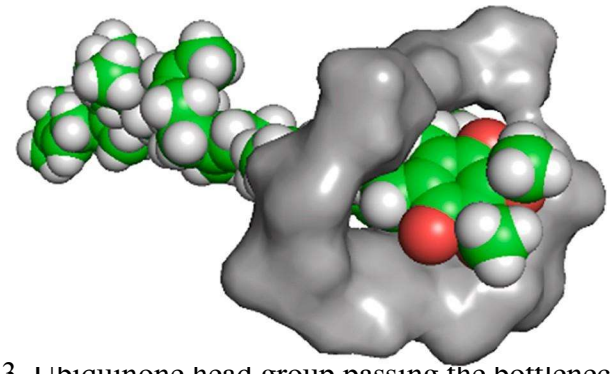

Fig. 3.3. Ubiquinone head group passing the bottleneck. The headgroup barely fits the bottleneck entrance of the quinone cavity. The energy barrier for the passage is discussed in the geometry analysis section. In the bacterial enzyme, menaquinone, decylubiquinone, and ubiquinone were all probed.

3.2.2 Molecular Dynamics Simulation

Here, four structures were MD-probed: bacterial T. thermophilus [2], yeast Y. lipolytica [6], and two mammalian structures - ovine [3], and human [8,22]. For mice [7] structure, in both so-called Active and Deactive states, the entrance to the Q-chamber is too small by visual and geometric analyses and was not further probed in MD simulations. However, we use all five structures in the discussion.

MD Simulation Details

As in the geometry analysis, we use complex I from T. thermophilus as an example of calculations, and comment on other structures when needed. The MD simulation details are given in SI. Briefly, the protein was incorporated into the POPC membrane. The quinone was placed near the entrance of Complex I, and after equilibration, was pulled into the quinone cavity. We also used simulations where quinone is pulled out of the quinone cavity. The energy was measured along the pulling trajectory.

To improve statistics, focused MD simulations on a restricted system that involved only the residues of the bottleneck were used. In this case the simulation box was filled with an artificial hydrophobic (LJ)medium consisting of water with switched-off charges. The Q was pulled with a speed of 0.1 Å per ps; this is about ten times slower than the rate of water molecule diffusion in bulk water ($D_w = 10^{-5}$ cm^2/s) [27]. In a focused MD the pulling speed was further reduced by a factor of ten to simulate adiabatic conditions for free energy evaluation. Other MD simulation details are given in SI.

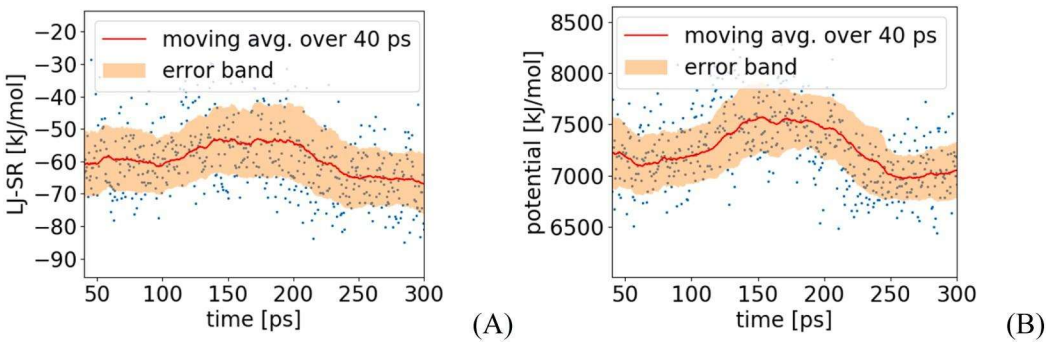

Fig. 3.4. A. The Lennard-Jones potential energy for a typical pulling trajectory. B. The total potential energy for the same trajectory.

Gromacs energies of the bottleneck

The potential energy components including bond energies, dihedral energies, Lennard-Jones energies, and Coulomb energies, as evaluated by the Gromacs MD simulation package, were evaluated along the Q-pulling trajectories for the residues representing the bottleneck, as shown in Fig. 3.2 for bacterial enzyme (see also SI Fig. A5). A typical energy profile for Gromacs Energy is shown in Fig. 3.4.

The Lennard-Jones (LJ) potential shows a bump of 10 kJ/mol between 100 ps and 225 ps, whereas the total potential energy – which includes bond energy, LJ energy and Coulomb energy, shows a bump of 250 kJ/mol between 100 ps and 225 ps. These bumps correspond to an increase of potential energy of the system at the passage of the ubiquinone head group of the bottleneck in the pulling trajectory. (The surprisingly small contribution of LJ is of theoretical interest but outside the scope of this paper and will not be discussed here.) The total energy shows significant fluctuations because of the large number of atoms involved; thermal energy fluctuations scale approximately as $k_b T\sqrt{3N}$, where N is the number of atoms.

The energy bump is a measure of the height of the barrier for the headgroup to pass the bottleneck. In this case it is about 250 kJ/mol or about 2.5 eV. This is an exceedingly high energy, which shows that spontaneously this transfer is not possible. In other words, the passage of the bottleneck is impossible. We explored several trajectories with different speed of pulling and different initial conditions, the qualitative result is the same for all trajectories. Some additional examples are given in SI.

We next explored a different measure of the elastic energy resulting from the forced passage of the headgroup through the bottleneck. This was necessary to see that the protein structure does deform as the quinone is forced through the bottleneck.

Deformation of the bottleneck. Empirical elastic energies

Here we monitored the deformation of the bottleneck and the variation of the associated phenomenological elastic energy. The idea is to trace the average geometry deformation of the bottleneck structure along the pulling trajectory and to evaluate associated elastic energy. Here 8 residues were chosen to represent the entrance of Q-tunnel: ALA63, PHE28, ALA29, SER66, PRO59, MET246, ALA242 and LEU243 shown in Fig. 3.2. Three different measures of deformation Δ of the structure were used:

Relative Deformation

$$\Delta_{rel} = \sum_{i,j}^{N_p} \frac{(d_{ij} - d_{ij}^{(0)})^2}{d_{ij}^{(0)}} \qquad (3.1.1)$$

Here summation is over all pairs of atoms N_p of the selected amino acids. The associated elastic energy E_{el} can be described as a value proportional to the square of the above distance, Δ. The proportionality coefficient is assigned according thermal average (k_BT per pair) of energy fluctuations:

$$E_{el} = k_B T \frac{<\Delta^2>}{<\Delta_{th}{}^2>} \qquad (3.1.2)$$

Short Axis Distance

Here Δ is the short axis distance between ALA63 and PHE28. Three distances between three methyl hydrogens of ALA63 and the single hydrogen of the benzene ring of PHE28 were used to evaluate the average distance. Ala63 is an important conserved residue, its mutation results in a dysfunctional enzyme with severe biomedical implications [1].

Root mean square distance

$$\Delta_{RMSD} = \sqrt{\sum_{ij}(d_{ij} - d_{ij}^{(0)})^2} \qquad (3.1.3)$$

Here, for every pair of atoms, the square of the difference between current distance and crystal structure distance was calculated along the trajectory. The square root of the sum of all 28 squared differences gives the RMS distance. The associated elastic energy was evaluated using Eq.(3.1.2).

Fig. 3.5 shows a typical result for relative deformation along the pulling trajectory.

The bump in Fig. 3.5 from 70 ps to 100 ps, corresponds to a passage of the head group through the bottleneck. Given the magnitude of thermal fluctuations, shown as a width of the band around the average value, an estimate of the elastic energy associated with the deformation of the structure around the bottleneck is about 100kT (N = 28). Clearly, this is a too high barrier to cross in a reasonable time.

The other two measures of deformation energy yield the same qualitative result. More data are shown in SI.

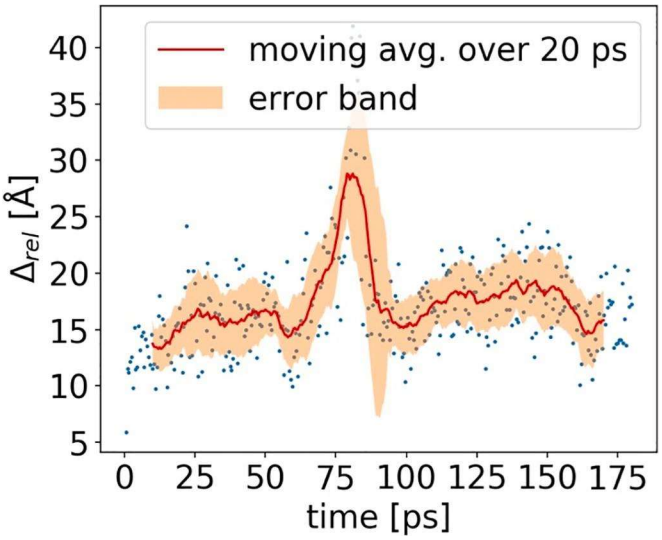

Fig. 3.5. Relative deformation along a typical pulling trajectory. Vertical axis is relative deformation, defined by Eq. 3.1.1. The energy bump corresponds to a passage of the headgroup through the bottleneck.

Finally, the most comprehensive characteristic of the process is the Helmholtz work (or Helmholtz free energy, W) to cross the bottleneck. This work is determined by the average force needed for an isothermal reversible change of the system; in our case this is the force applied to pull the quinone through the bottleneck, along the pulling coordinate λ:

$$\left(\frac{\partial W}{\partial \lambda}\right)_T = < F >$$

$$\Delta W = \int_{(i)}^{(f)} < F > d\lambda \qquad (3.1.4)$$

The above relations assume a reversible or quasi-equilibrium (in practice very slow) change of the system. For this reason, the pulling rate was further decreased to 0.01 Å per ps, which is now about hundred times slower than the diffusion rate of water. This is taken to be a sufficiently slow process, so the quasi-equilibrium condition for application of the above is satisfied. The force 〈F〉 is assumed to be averaged over thermal fluctuations (for a given λ), and over a set of different initial conditions in the initial state (i). In our calculations, the pulling force F(t) is measured along the MD pulling trajectory and averaged locally (moving average) over a short interval of 100 ps, for a typical pulling trajectory of some 1500 ps. In addition, the averaging was done over some 30–60 pulling trajectories with different initial conditions. The Helmholtz work ΔW gives the energy barrier along the trajectory.

If the final state of quinone (f) is defined as a region at the top of the barrier, i.e. position of the quinone head group inside the bottleneck,and the initial state (i) is a region inside the Q-chamber, the work described above is related to both decrease of entropy (as in isothermal contraction of gas) and increase of potential energy (elastic spring) energy of the system due to geometric restriction of putting the over-sized quinone head group into a relatively narrow

bottleneck of the cavity entrance. Both, the entropy decrease and elastic energy increase that occur during this process were approximately evaluated separately in the previous sections; here the measure that combines the two is described as Helmholtz work. The results are shown in the following figures.

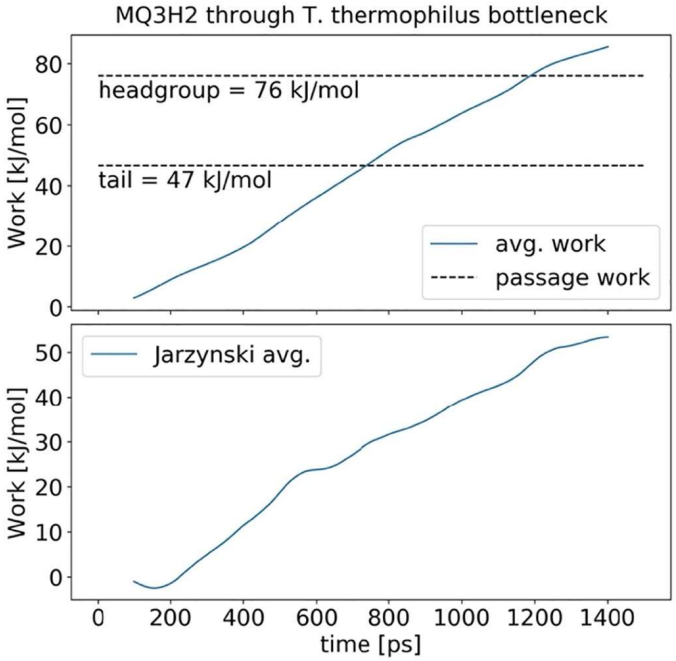

Fig. 3.6. Upper panel: average work of bottleneck crossing by the reduced menaquinone, MQH2, in bacterial T. thermophilus enzyme. The upper dotted line corresponds to work required to find and enter the bottleneck by the headgroup of MQ, and the lower one corresponds to moving (two) methyl groups through the bottleneck. Lower panel: Jarzynski averaged work along the trajectory. The bumps on the curve correspond to the passage of the head group and methyl groups of the tail through the bottleneck.

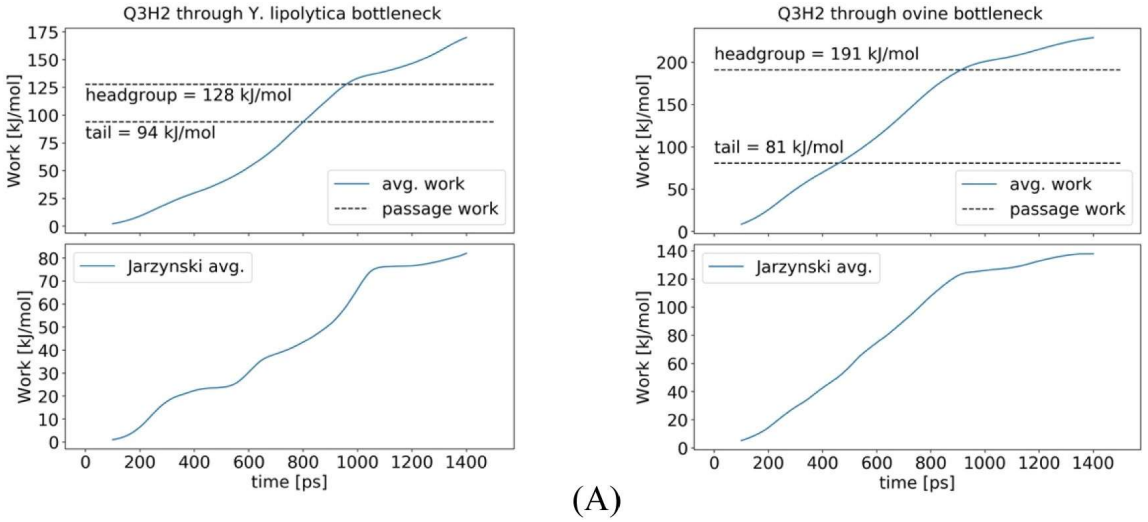

(A) (B)

Fig. 3.7. The average work along the pulling trajectory of ubiquinone (reduced, Q3H2, with 3 isoprenoid units) through the bottleneck of the Q-chamber in Y. lipolytica (A) and ovine (B) enzymes. The values under dotted lines give corresponding energy barriers for the headgroup and the two isoprenoid units of the tail passage. Lower panels show JA work along the pulling trajectory.

In the literature, often instead of Eq. (3.1.4) a different relation between the work and thermodynamic free energy is employed. Namely, if the pulling work were calculated for a non-equilibrium process at a constant energy, as opposed to constant temperature and quasi-equilibrium process considered here, the Jarzynski equality (JE) would be used [28],

$$< \Delta W >_J = -RTln\left(< e^{-\frac{\Delta w}{RT}} >\right) \qquad (3.1.5)$$

where Δw is the work for a given pulling trajectory, and the averaging shown by brackets is assumed over different trajectories. We need to note that the conditions of our calculation are different from what is assumed in the JE, and thus the above relation is not directly applicable here; however, we find it useful to consider this type of averaging (Jarzynski Average (JA)) as it emphasizes trajectories with minimal work and thus selects (or filter) the "optimal" trajectories. As such, JA is sensitive to qualitative changes along the trajectory, such as the entrance of the headgroup into the bottleneck or the passage of individual methyl groups of isoprenoid tail of ubiquinone, which show up as small bumps on the JA curves, see Fig. 3.6. Therefore, here in addition to the usual thermodynamic averaging we also calculated the Jarzynski averaged work along the pulling trajectories, which is shown together with the usual thermodynamic averaged work, Figs. 3.6 and 3.7.

Two sets of calculations were carried out: one with a geometry restricted to that in the pdb structures (results shown in SI), and the second with a weak restraint on the structure.

If weak restraints are applied, namely keeping backbone atoms restrained by 50 kJ/mol $Å^{-2}$, and 10 kJ/mol $Å^{-2}$ for side chain atoms (a hydrogen bond is about 20 kJ/mol), the barriers become lower than in the rigid structure (see SI), but still too high to allow reasonable timescale of free passage even for the tail. It is useful to keep in mind that a barrier of 30 kJ/mol gives a factor of 10^{-5} in the barrier-crossing rate expression (where the prefactor is of the order of maximum 108 s^{-1}). Same factor appears in the effective diffusion constant for tail movement through the entrance.

Fig. 3.6 shows the average work (or free energy) of bottleneck crossing by the reduced menaquinone, MQH2, in bacterial T. thermophilus enzyme. The dotted lines in the figure correspond to so-called "first passage" work, i.e. work required to find and enter the bottleneck by the headgroup of MQ and moving the methyl groups of the tail through the narrow entrance. In this case two methyl groups were passing the bottleneck. The reduced form of MQH2 requires some 20 kJ/mol more energy to pass the bottleneck barrier (see SI). The average work of the order of 100 kJ/mol is similar to what we found in previous calculations, and obviously is too high to pass the bottleneck without conformational opening of the structure. The passage of the head group and the methyl groups of the tail through the bottleneck are reflected as small bumps on the Jarzynski averaged work shown on the lower panel of the Figure.

Fig. 3.6 gives a typical result of calculated work along the pulling trajectory. In SI we show results for decylubiquinone, and ubiquinone passage. These quinone variations give similar

values, and all barriers are in the range of 100-140 kJ/mol for the restrained structures. It is interesting that decylubiquinone is somewhat more easily passes the bottleneck, despite the presence of two methoxy groups in the headgroup, and somewhat more easily than ubiquinol – obviously due to a difference in the structure of the tail of the molecule.

Results for Y. lipolytica, ovine, mice, and human enzymes

Results for mt enzymes are qualitatively no different than for the bacterial enzyme. For mt ovine and yeast Y. lipolytica enzymes key results are shown in Fig. 3.7. In the latter case, the pulling of quinone was simulated using the cryo-EM structure showing one quinone molecule locked inside, see SI figure. As can be seen, the barriers are again too high for the bottleneck passage both for the headgroup and for the tail.

Additional results, including those for ovine and human enzymes, shown in SI yield the same qualitative conclusion as for the yeast enzyme – the bottleneck is too narrow for both the headgroup and even the tail passage. The visual and geometric analyses of the mice structure readily indicate that the entrance to Q-chamber is closed (both in Active and Deactive states [7]) as it is significantly smaller than in all other enzymes considered. Thus, there was no need to do any additional calculations on the mice structure.

We conclude that the size of the entrance is prohibitively small for the quinone molecule to pass either in oxidized or in the reduced form. Yet the bottleneck is largest in the bacterial T. thermophilus enzyme. The structure of the bacterial enzyme was solved with X-ray, while the other structures were solved using cryo-EM. For mt enzymes, the bottleneck is largest for yeast, and decreases for ovine, human, and mice structures.

There are slight variations in all structures examined, but in all structures the bottleneck is too narrow to be operational to admit quinone to the binding site.

3.3 Discussions and Conclusions

3.3.1 The bottleneck is too narrow to be operational

In five published structures of complex I - bacterial T. thermophilus, yeast Y. lipolytica, and three mammal, mice, ovine, and human, the bottleneck at the entrance of the quinone chamber is too narrow for a quinone or quinol to pass. This follows from our detailed geometry analysis of the structures (including B-factors) and MD simulations of the barrier formed by the narrow entrance. As the issues is critical, and the conclusion depends on variations in structure of just a few angstroms, several different methods were used to solidify the conclusion that if taken as in the available structures, the channel is inaccessible from outside; or, if a molecule of ubiquinone is inside, it will not be able to exit the Q-chamber. Moreover, the bottleneck is too narrow even for a passage of the isoprenoid tail of ubiquinone. Essentially, taken as is the structures represent a non-functional enzyme. This can be a result of artificial, out of the membrane conditions [29] and/or low cryogenic temperatures of structural data acquisition, both in X-ray or cryo-EM.

It is surprising to see the same conclusion in all structures analyzed– both obtained with X-ray and cryo-EM, despite some notable variations in the structures. For example, in the mouse [7] enzyme the differences between the active and deactive structures are clearly seen; but in both cases the opening of the Q-tunnel is closed. It looks like both structures are somehow

compressed (presumably by de-solvation forces) so that the soft opening part, the bottleneck, is closed up. It is tantalizing to speculate on the general nature of the phenomenon, i.e. the structures of all membrane proteins taken out of their natural membrane environment are under additional stress of de-solvation forces, or low temperature, and the flexible enzymes, such as complex I, may be deformed to assume unfunctional forms.

In order to open the entrance of the quinone chamber, some conformational change (discussed below) is needed. However, it is not clear to what extent the structure should be opened [24]. The bottleneck is formed by three helices of ND1, two of which are in direct contact with TM1 and the loop between TM1 and TM3 of subunit ND3 that was shown recently to be essential in functional conformational changes of the enzyme [12]. Obviously, this part of the enzyme is conformationally labile, and it is not surprising that under unnatural conditions the structure is locked in one of the deformed unfunctional states.

That the narrow bottleneck may depend on the conformation of the protein is supported by recent data of Zickermann et al. [6]. In SI Fig. A13 we compare the position of UQ9 found in their Y. lipolytica structure with that of the Q-cavity in T. thermophilus structure. Some key residues of the middle and upper part of the Q-cavity almost perfectly overlap; however the tail of the quinone molecule is shifted from the position of T. thermophilus bottleneck, which indicates that in the structure of Ref. [6] the bottleneck is deformed, which points to its conformational flexibility. The bottleneck of the yeast enzyme is slightly modified (due to the presence of two new residues Ser18, and Val19), and Phe17, which is equivalent to Phe28 (see Fig. 3.2) is now shifted. The distance between Phe17 and Ala 54 (equivalent of Ala63) is 9.4 Å instead of 5.6 Å in the bacterial structure. What is interesting is that the narrow bottleneck is still formed by a slightly different set of residues (see SI Fig. A13), which may point to a conserved feature necessary for enzyme functionality. Yet the bottleneck in Y. lipolytica structure is also too narrow for a head group or even the tail to pass through it.

3.3.2 The quinone shuttle model is unlikely

One may think that with minor changes, the published structures do represent the actual geometry in which the headgroup cannot pass the bottleneck, but one molecule of quinone is locked (most of the time) inside the binding cavity and works as a shuttle carrying electrons between the two ends of the 30 angstrom-long channel [17,18,30]. Indeed, a recent structure of yeast enzyme does show one molecule of quinone inside of the binding cavity [6]. Another interesting recent report probed the function of oversized alternative quinones and found that in sub-mitochondrial particles (SMP) the reduction was possible, but not so in proteo-liposomes (PL). This may be too argued in favor of a shuttle model – assuming that in native membrane of SMP one molecule still remains in the enzyme shuttling electrons between N2 and bulky modified quinones that need not enter the narrow channel themselves; however, in PL such a molecule is removed by the detergents, and the reduction is not possible. The explanation based on the assumption of a residual quinone in the SMP membrane would be supported by the residual activity of cryo-EM single particles observed in Ref. [4]. However, based on our simulations results and the analysis of bi-molecular rates below, the model with one quinone molecule inside of the chamber appears to be unrealistic, supporting the earlier conclusion of Ref. [29].

3.3.3 The bottleneck is too narrow even for isoprenoid tail to pass

The barrier crossing rate by a quinone molecule at the bottleneck can be estimated from the transition state theory; namely, the rate of a single barrier crossing – be it a headgroup, or one of the methyl groups of the isoprenoid tail, is given by the following expression:

$$k \approx \frac{D_q}{L_0^2} 10^{-\frac{V_b}{ln(10)RT}} \qquad (3.1.6)$$

where Dq is the diffusion coefficient of quinone in the membrane environment, Dq ~ 10^{-7} – 10^{-8}cm^2/s [17], and L0 is a characteristic length of the barrier width [32]. The first factor (assuming barrier width 1–3 Å) is of the order of 10^8 s^{-1}. The exponential factor (ln(10)RT = 6 kJ/mol, at room temperature) should be greater than 10^{-5}, thus $V_b \approx$ 30kJ/mol or less. All our energy barriers are in gross excess of this critical value, thus in the functional state the structure should be opened.

Although it is not clear to what extent the structure is opened in the functional enzyme, it appears unlikely that the structure would be open only for a free tail passage while blocking the headgroup. This is because the methyl groups of isoprenoid tail also present a challenge of passing a narrow bottleneck, as our calculations suggest. The effective diffusion constant for isoprenoid tail movement through the bottleneck is modified by the same exponential factor discussed above (barrier counted per one methyl group, Figs. 3.6, 3.7) and is too small to be operational in all structures examined.

Thus, taken as is in the structures, the bottleneck is too narrow to be operational even for the shuttle model.

3.3.4 In the open state the entrance to Q-chamber remains narrow

As some conformational change is needed to open the bottleneck, it appears that the entrance remains to be relatively narrow in the open functional state based on the available kinetic data. This conclusion is based on the activity of the enzyme in artificial proteo-liposomes (PL) and K_m and k_{cat} of the quinones of different types in complex I [21]. The argument is as follows.

Consider the efficiency parameter defined as $\kappa_{BM} = k_{cat}/K_m$. Under the condition of $k_{cat} >> k_{dis}$, the efficiency parameter is the pseudo-second-order rate constant that can be estimated as follows. In 3D diffusional model [27]

$$\kappa_{BM} = 4\pi r_0 \, D_q \, (N_A/10^3) P_r \qquad (3.1.7)$$

Here we consider the diffusion of quinone headgroup from the membrane interior medium to the entrance of Q-tunnel of the enzyme H- subunit as a 3D process, see Fig. 3.1A. It is assumed that the binding site is a 3D half-sphere of radius r_0, diffusion coefficient (for center of mass) of substrate is Dq, the factor with Avogadro number is introduced for convenient units M^{-1} s^{-1}, and CGS for r_0 and D_q. The factor P_r describes the probability that a substrate arriving at the binding site via diffusion will have a right orientation for binding. The more intricate binding site configuration is, the smaller the probability P_r.

An equivalent expression for 2D diffusion [33,34] in the membrane plane gives qualitatively similar results. Here,

$$\kappa_{BM} = \frac{\pi D_q d_m (N_A/10^3) P_r}{ln(R_0/r_0)} \qquad (3.1.8)$$

where d_m is the membrane width (of the order of 50 Å), and R_0 is the typical distance between substrate molecules in the membrane (for [Q] = 10 mM, R_0 = 10 nm). The factor in the denominator is never too large, and realistically is in the range of 5–7 for realistic r_0 = 1 Å, or somewhat less, assuming order of magnitude values. Given these values the two expressions give qualitatively similar results for r_0 = 1 Å. (Radius r_0 characterizes the position of center of mass of a diffusing molecule in the binding process, whereas the fitting orientation is described statistically by the probability parameter P_r.)

The diffusion coefficient Dq is assumed to be in the range [17,27] of 10^{-7} to 10^{-8} cm^2/s for the substrates of our interest, but can be modified by the barrier at the bottleneck, as described earlier.

The above expressions describe the available data rather well. For example, for the NADH oxidation reaction of Ref. [21] both theory and experiment give $k_{cat}/K_m = 10^7$, for r_0 = 1 Å and Pr = 1. Similar values are obtained for AOX of Ref. [21]. However, for Q-reduction k_{cat}/K_m in Ref. [21] is much smaller and depending on the length of isoprenoid tail is in the range of 10^4 to 10^5. This significant reduction can be readily explained by an additional small factor P_r in the range of 10^{-2} to 10^{-3} or even smaller. This could be rationalized by the difficulty of passing through a narrow entrance of the Q-channel. (Admittedly, other less obvious scenarios cannot be entirely ruled out; e.g., the case $k_{cat} << k_{dis}$. In this case $k_{cat}/K_m = \kappa_{BM} \cdot (k_{cat}/k_{dis})$, i.e. the above parameter κ_{BM} is multiplied by a small ratio (k_{cat}/k_{dis}). One could speculate that a small k_{cat} would be expected in the Q-shuttle model due to an intricate and slow exchange of two electrons between the shuttle Q molecule and the quinones of the pool.)

3.3.5 Possible conformational changes in the bottleneck during the pumping cycle

In our calculations we simulated the exit of a quinol molecule from the cavity pulling it out by the tail. This was done in order to provide the natural funnel for the headgroup to find the narrow exit. As QH_2 headgroup is geometrically larger than Q, we naturally find that it takes some 20 to 40 kJ/mol extra energy for QH_2 to cross the bottleneck barrier for the structures we examined. A possibility remains open that the bottleneck changes its size during the enzyme cycle. Indeed, the selective admission of Q vs QH_2 to the reduction chamber would be beneficial for the function; but once in the reduced form, QH_2 would need an opening of the narrow selectivity filter, which the bottleneck can provide. Given the strong conformational coupling with other parts of the enzyme that are involved in conformational changes [12] during the cycle, such a scenario is possible. Such a coupling would explain the effect of distant mutations in the membrane ND5 that both shut down the proton pumping and reduce redox activity of the enzyme [31]. Although more recent data [12] indicating that locking the loop of ND3 that shuts the pumping still retains the redox activity appears to contradict this idea.

3.3.6 The structure of the open state of the bottleneck

Finally, it is interesting to speculate how the structure might look like in the open state. In Fig. A14 in the SI we suggest that the scissor- like cross motion of TM1 and TM6 and the coupled movement of AH1 helices are needed to open the structure. It is noticed that TM1 and AH1 of ND1 are both coupled to TM1 of ND3 involved in conformational changes [12] in

proton pumping. Thus, in the open (and functional) state the whole structure will look somewhat differently from what the current pdb structures show. The deformed state is likely due to both the flexibility of the enzyme in this part of the structure, and the unnatural artificial forces (in the conditions in which the structure was resolved) deforming the enzyme. The proper phospholipid environment and room temperatures would return the enzyme into its native functional state; the results of Ref. [29] appear to support this conclusion.

A detailed study of possible conformations that open the bottleneck is currently underway in this group. Here we notice that in all structures, TM1 helix forming the bottleneck is bent in the upper three turns, obviously due to pressing forces of the surrounding structure. This may be also an artifact of the structure, as there is no chemical reason for the bend. In MD simulations, the free helix becomes straight in 100 ps, Fig. A14. Thus, in the open state, the helix can be straight; this would push AH1 (through the loop coupling TM1 and AH1) and would open the bottleneck. The collective motion of the whole structure that is coupled to the movement of the bottleneck is of interest as a similar movement is expected to be involved in the functional conformational change of the enzyme.

3.4 Declaration of competing interest

The authors declare that they have no known competing financial interests or personal relationships that could have appeared to influence the work reported in this paper.

3.5 Acknowledgements

This work has been supported in part by the NIH research grant GM054052 and BSF Grant No. 2018239 A19-3374 (AAS). We wish to acknowledge contribution of Dr. Kevin Demarco who took part in early studies of the subject and helped to create Fig. A4. We are grateful to Dr. James Letts and Dr. Leo Sazanov for stimulating discussion of complex I, and Dr. Guilherme Arantes for a valuable comment. Finally, we should thank our reviewers for stimulating comments and questions that helped this paper to take its final shape.

3.6 Supplementary Data

Supplementary data to this article can be found online at https://doi.org/10.1016/j.bbabio.2020.148326. In this reproduction the supplementary data is also in Appendix A of this dissertation.

3.7 References

1. L.A. Sazanov, A giant molecular proton pump: structure and mechanism of respiratory complex I, Nat. Rev. Mol. Cell Biol. 16 (2015) 375–388.
2. R. Baradaran, J.M. Berrisford, G.S. Minhas, L.A. Sazanov, Crystal structure of the entire respiratory complex I, Nature 494 (2013) 443–448.
3. K. Fiedorczuk, J.A. Letts, G. Degliesposti, K. Kaszuba, M. Skehel, L.A. Sazanov, Atomic structure of the entire mammalian mitochondrial complex I, Nature 538 (2016) (406-+).

4. J.A. Letts, K. Fiedorczuk, G. Degliesposti, M. Skehel, L.A. Sazanov, Structures of respiratory supercomplex I+III2 reveal functional and conformational crosstalk, Mol. Cell 75 (1131–1146) (2019) e1136.
5. V. Zickermann, C. Wirth, H. Nasiri, K. Siegmund, H. Schwalbe, C. Hunte, U. Brandt, Structural biology. Mechanistic insight from the crystal structure of mitochondrial complex I, Science 347 (2015) 44–49.
6. K. Parey, O. Haapanen, V. Sharma, H. Kofeler, T. Zullig, S. Prinz, K. Siegmund, I. Wittig, D.J. Mills, J. Vonck, W. Kuhlbrandt, V. Zickermann, High-resolution cryo-EM structures of respiratory complex I: mechanism, assembly, and disease, Sci. Adv. 5 (2019) eaax9484.
7. A.A. Agip, J.N. Blaza, J.G. Fedor, J. Hirst, Mammalian respiratory complex I through the lens of cryo-EM, Annu. Rev. Biophys. 48 (2019) 165–184.
8. R. Guo, S. Zong, M. Wu, J. Gu, M. Yang, Architecture of human mitochondrial respiratory megacomplex I2III2IV2, Cell 170 (1247–1257) (2017) e1212.
9. R.G. Efremov, R. Baradaran, L.A. Sazanov, The architecture of respiratory complex I, Nature 465 (2010) 441–445.
10. L.A. Sazanov, P. Hinchliffe, Structure of the hydrophilic domain of respiratory complex I from Thermus thermophilus, Science 311 (2006) 1430–1436.
11. M.A. Tocilescu, V. Zickermann, K. Zwicker, U. Brandt, Quinone binding and reduction by respiratory complex I, Biochim. Biophys. Acta 1797 (2010) 1883–1890.
12. A. Cabrera-Orefice, E.G. Yoga, C. Wirth, K. Siegmund, K. Zwicker, S. Guerrero-Castillo,
Zickermann, C. Hunte, U. Brandt, Locking loop movement in the ubiquinone pocket of complex I disengages the proton pumps, Nat. Commun. 9 (2018) 4500.
13. R.G. Efremov, L.A. Sazanov, Structure of the membrane domain of respiratory complex I, Nature 476 (2011) 414–420.
14. A.A. Stuchebrukhov, Redox-driven proton pumps of the respiratory chain, Biophys. J. 115 (2018) 830–840.
15. A.A. Stuchebrukhov, Kinetics and efficiency of energy-transducing enzymes, J. Phys. Chem. B 123 (44) (2019) 9456–9465.
16. M.H. Teixeira, G.M. Arantes, Balanced internal hydration discriminates substrate binding to respiratory complex I, BBA - Bioenergetics 1860 (2019) 541–548.
17. J. Warnau, V. Sharma, A.P. Gamiz-Hernandez, A. Di Luca, O. Haapanen, I. Vattulainen, M. Wikstrom, G. Hummer, V.R.I. Kaila, Redox-coupled quinone dynamics in the respiratory complex I, Proc. Natl. Acad. Sci. U. S. A. 115 (2018) E8413–E8420.
18. M. Wikstrom, V. Sharma, V.R. Kaila, J.P. Hosler, G. Hummer, New perspectives on proton pumping in cellular respiration, Chem. Rev. 115 (2015) 2196–2221.
19. V. Sharma, G. Enkavi, I. Vattulainen, T. Róg, M. Wikström, Proton-coupled electron transfer and the role of water molecules in proton pumping by cytochrome c oxidase, Proc. Natl. Acad. Sci. U. S. A. 112 (2015).
20. M.A. Hagras, A.A. Stuchebrukhov, Concerted two-electron reduction of ubiquinone in respiratory complex I, J. Phys. Chem. B 123 (2019) 5265–5273.
21. J.G. Fedor, A.J.Y. Jones, A. Di Luca, V.R.I. Kaila, J. Hirst, Correlating kinetic and structural data on ubiquinone binding and reduction by respiratory complex I, Proc. Natl. Acad. Sci. U. S. A. 114 (2017) 12737–12742.

22. J. Gu, M. Wu, M. Yang, Cryo-EM Structure of Human Respiratory Complex I, (2017), https://doi.org/10.2210/pdb5XTD/pdb.
23. A.A. Agip, J.N. Blaza, H.R. Bridges, C. Viscomi, S. Rawson, S.P. Muench, J. Hirst, Cryo-EM structures of complex I from mouse heart mitochondria in two biochemically defined states, Nat. Struct. Mol. Biol. 25 (2018) 548–556.
24. S. Uno, T. Masuya, K. Shinzawa-Itoh, J. Lasham, O. Haapanen, T. Shiba, D.K. Inaoka, Sharma, M. Murai, H. Miyoshi, Oversized ubiquinones as molecular probes for structural dynamics of the ubiquinone reaction site in mitochondrial respiratory complex I, J. Biol. Chem. 295 (2020) 2449–2463.
25. K. Berka, O. Hanák, D. Sehnal, P. Banáš, V. Navrátilová, D. Jaiswal, C.-M. Ionescu, R. Svobodová Vařeková, J. Koča, M. Otyepka, MOLEonline 2.0: interactive web-based analysis of biomacromolecular channels, Nucleic Acids Res. 40 (2012) W222–W227.
26. J. Kyte, R.F. Doolittle, A simple method for displaying the hydropathic character of a protein, J. Mol. Biol. 157 (1982) 105–132.
27. A. Stuchebrukhov, J. Schafer, J. Berg, P. Brzezinski, Kinetic advantage of forming respiratory supercomplexes, Biochim. Biophys. Acta Bioenerg. 1861 (2020) 148193.
28. J. Liphardt, S. Dumont, S.B. Smith, I. Tinoco Jr., C. Bustamante, Equilibrium information from nonequilibrium measurements in an experimental test of Jarzynski's equality, Science 296 (2002) 1832–1835.
29. S. Drose, K. Zwicker, U. Brandt, Full recovery of the NADH:ubiquinone activity of complex I (NADH:ubiquinone oxidoreductase) from Yarrowia lipolytica by the addition of phospholipids, Biochim. Biophys. Acta 1556 (2002) 65–72.
30. O. Haapanen, V. Sharma, A modeling and simulation perspective on the mechanism and function of respiratory complex I, Biochim. Biophys. Acta Bioenerg. 1859 (2018) 510–523.
31. E. Nakamaru-Ogiso, M.C. Kao, H. Chen, S.C. Sinha, T. Yagi, T. Ohnishi, The membrane subunit NuoL(ND5) is involved in the indirect proton pumping mechanism of Escherichia coli complex I, J. Biol. Chem. 285 (2010) 39070–39078.
32. S. Hammes-Schiffer, A.A. Stuchebrukhov, Theory of coupled electron and proton transfer reactions, Chem. Rev. 110 (2010) 6939–6960.
33. Y. Georgievskii, E.S. Medvedev, A.A. Stuchebrukhov, Proton transport via the membrane surface, Biophys. J. 82 (2002) 2833–2846.
34. Y. Georgievskii, E.S. Medvedev, A.A. Stuchebrukhov, Proton transport via coupled surface and bulk diffusion, J. Chem. Phys. 116 (2002) 1692–1699.

4. Second Paper on Squeeze in Mechanism

This chapter is a reproduction of prior work published. "Quinone binding in respiratory complex I: Going through the eye of a needle. The squeeze-in mechanism of passing the narrow entrance of the quinone site", Nithin Dhananjayan, Panyue Wang, Igor Leontyev, Alexei A. Stuchebrukhov. The supplemental information will also be provided in Appendix B of the dissertation.

Abstract

At the joint between the membrane and hydrophilic arms of the enzyme, the structure of the respiratory complex I reveals a tunnel-like Q-chamber for ubiquinone binding and reduction. The narrow entrance of the quinone chamber located in ND1 subunit forms a bottleneck (eye of a needle) which in all resolved structures was shown to be too small for a bulky quinone to pass through, and it was suggested that a conformational change is required to open the channel. The closed bottleneck appears to be a well-established feature of all structures reported so-far, both for the so-called open and closed states of the enzyme, with no indication of a stable open state of the bottleneck. We propose a squeeze-in mechanism of the bottleneck passage, where dynamic thermal conformational fluctuations allow quinone to get in and out. Here, using molecular dynamics simulations of the bacterial enzyme, we have identified collective conformational changes that open the quinone chamber bottleneck. The model predicts a significant reduction—due to a need for a rare opening of the bottleneck—of the effective bi-molecular rate constant, in line with the available kinetic data. We discuss possible reasons for such a tight control of the quinone passage into the binding chamber and mechanistic consequences for the quinone two-electron reduction.

Graphic Abstract

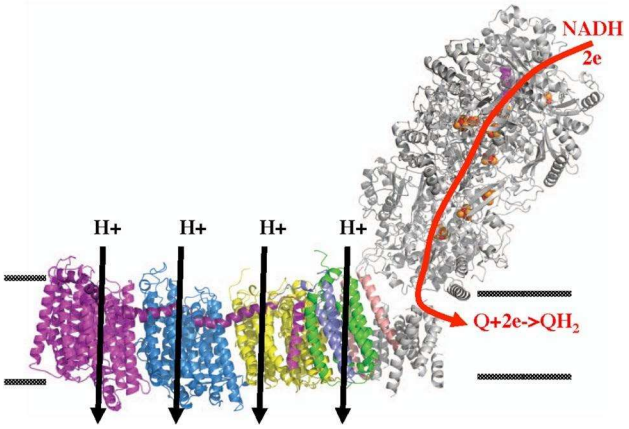

4.1 Introduction

NADH:ubiquinone oxidoreductase, or respiratory complex I, is a key proton-pumping enzyme of the energy-generating machinery in the cell [1, 2]. Recent structural studies[3–13] of the enzyme have revealed molecular details that suggest possible molecular mechanisms of its redox-driven proton pumping. Complex I is an L-shaped structure with a hydrophilic domain where electron transport takes place and a membrane domain that performs proton translocation [4, 14]. In the hydrophilic domain, NADH transfers 2 electrons to flavin mononucleotide (FMN), which then transfers electrons via a chain of seven iron sulfur (FeS) clusters to a quinone molecule (*Q*) reducing it to a quinol [15]. The transfer of two electrons to quinone [16] is a key exergonic step, which is believed to drive local conformational changes [2, 11, 17] that transmit to the membrane domain of the complex and help to drive the proton pumping [18, 19]. The new structures have also opened a new intriguing question about the mechanism of quinone binding to the enzyme, which is addressed in this paper.

In all organisms, from bacteria to human, the structure of the core part of the enzyme reveals an almost 30 angstrom tunnel-like chamber for ubiquinone binding (Q-chamber) that leads from the N-edge of the membrane up to N2 FeS cluster. Presumably, the quinone molecule migrates from the membrane into the binding chamber, diffuses up to N2 cluster, receives two electrons and migrates back – tail first, from the narrow binding cavity to the membrane [8, 18, 20–25].

In all organisms, the core part of the enzyme is very similar to bacterial enzyme; here, the entrance to Q-chamber is formed by a specific crossing of TM1, AH1, and TM6 in Nqo8 (mtND1/H *E.coli*) [4] and forms a narrow bottleneck that restricts the access to the Q-tunnel. The bottleneck was identified in the structure early on [4, 26], and it was speculated that conformational changes are needed to open it; however, the molecular mechanism of quinone passing the narrow bottleneck remains to be obscure, see Ref. [27] Recently [28], we characterized the entrance bottleneck more rigorously using Molecular Dynamics (MD) simulations to quantify the energy barrier formed by the narrow bottleneck. Computer simulations of quinone passage through the bottleneck suggest that in all structures available, from bacterial to human (including most recent structures [3, 11–13], see below), this bottleneck is too narrow for the quinone or quinol to pass and that a conformational change is indeed required to open the channel. Moreover, in yeast *Y. lipolytica* [8] structure, the quinone is seen bound in the cavity, with a half of the isoprenoid tail crossing the bottleneck. However, here too the bottleneck (taken as in the reported pdb structure) was found to be too narrow for the head group, or even for the isoprenoid tail, to freely move through the narrow entrance of the quinone chamber, indicating the quinone molecule is stuck in the position seen in the structure and suggesting that dynamic or static opening of the bottleneck is needed to allow movement of the quinone. Thus, the question arises as to how the bulky substrate is going through a narrow passage, as if through the eye of a needle?

Previously we concluded that the apparent bottleneck closed structure could be explained by two possibilities: in one, the closed structure is an artifact of the crystallization packing forces, cryo-EM low temperature, or other specific conditions occurring in the structural data acquisition that affect this flexible part of the enzyme, assuming that a functional open bottleneck structure exists in the natural membrane environment of the enzyme, yet unseen in the available structures. Another possibility is that the stable open bottleneck state in enzyme does not actually exist, and only rare thermal fluctuations of the enzyme structure would open the bottleneck and allow admission of the quinone molecule to the quinone chamber, with tightly

controlled overall passage of the quinone to the binding site by some intricate mechanism.

Most recent data [3, 11] indicate that in all available structures (twenty-three analyzed so far) including both so- called “open” and “closed” states [3, 11] (not to be confused with open and closed bottleneck of this paper), involving well-resolved structural changes of other parts of the enzyme seen both in X-ray and cryo-EM, the bottleneck is about the same and is in the closed state as we identified it. Thus, the new data suggest that the stable open bottleneck state (or quasi-stable state with significant thermal population to be captured in the plunge-freezing of cryo-EM) does not seem to exist. Therefore, it now appears more likely that the bottleneck opening occurs dynamically in the course of thermal fluctuations, suggesting a specific intricate mechanism of the passage of the quinone through the bottleneck.

Here, using molecular dynamics simulations (both all- atomic and coarse grained) of the bacterial enzyme we have identified collective conformational changes (Principal Component Analysis, PCA, modes) that dynamically open the quinone chamber bottleneck. The changes involve mostly TM1 helix, which straightens up, AH1 helix, which moves to open the structure, and the loop between them; but in general, the changes involve rearrangement of a larger part of the enzyme. We propose a specific “squeeze-in” mechanism of the bottleneck passage, where the rare conformational fluctuations along the identified PCA mode allow quinone in and out.

The simulations indicate that the most flexible part of the enzyme Nqo8 subunit involves structural elements that form the bottleneck; this suggests that if external forces— e.g., from the bound adjacent subunits—were applied, the entrance into Q-chamber would be affected most, possibly to be squeezed and locked in a closed state. This could explain the closed bottleneck state in all the resolved structures. The model predicts a significant reduction—due to a need for a rare opening of the bottleneck—of the effective bi-molecular binding rate constant, which is in line with the available kinetic data. We discuss possible reasons for such a tight control of the passing of the quinone into the binding chamber, which remain to be obscure at present.

4.2 Method and Results

4.2.1 The bottleneck of the Q-chamber

Previously [28], five structures were analyzed: bacterial *T. thermophilus* [4], yeast *Y. lipolytica* [8], and three mammalian structures, ovine [5], mice [9], and human [10, 29]. As the core part of the enzyme is almost identical to the 14 subunits of the bacterial complex, and the results are qualitatively similar for all structures analyzed, here we consider first the bacterial structure. The entrance of the quinone chamber is formed in ND1 subunit (Nqo8/H subunit of bacterial enzyme); the elastic properties of this subunit, considered within the enzyme context, define the static and dynamic properties of the bottleneck.

For the analysis of the bacterial complex I, we use the structure *T. thermophilus,* 4HEA [4] with the highest resolution of 3.1 Å. The entrance to quinone binding cavity and the amino acids comprising the orifice of the entrance, i.e. the bottleneck, are shown in Fig. 4.1.
The bottleneck is localized at the narrow crossing framed by three helices: TM1, AH1, and TM6 [4] of ND1/Nqo8 subunit (see below); the properties of the bottleneck is the focus of the MD simulations in this paper.

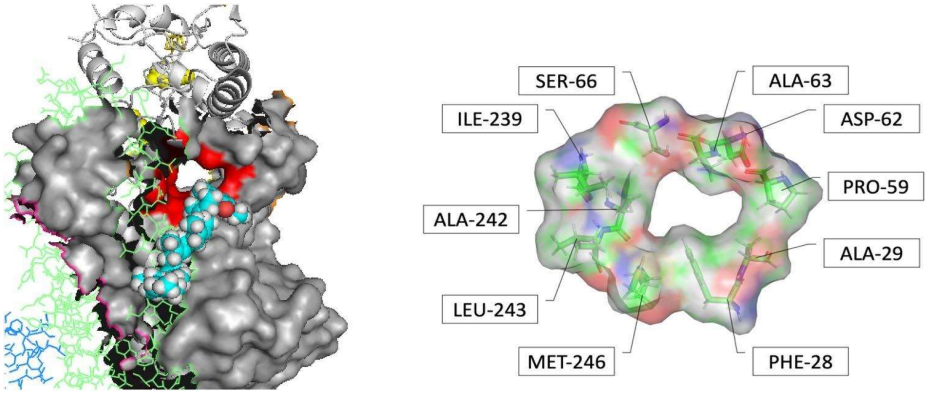

Fig. 4.1 A Left. The entrance into the Q-binding cavity is shown in red. Gray surface refers to subunit ND1, green lines— subunit A, and cyan spheres represent the quinone (from MD simulations in Ref. [28]). B Right. 10 residues that form the entrance of complex I Q-cavity in bacterial enzyme; the bottleneck is in the opening in the middle of the structure

4.2.2 The bottleneck is about the same in all structures available

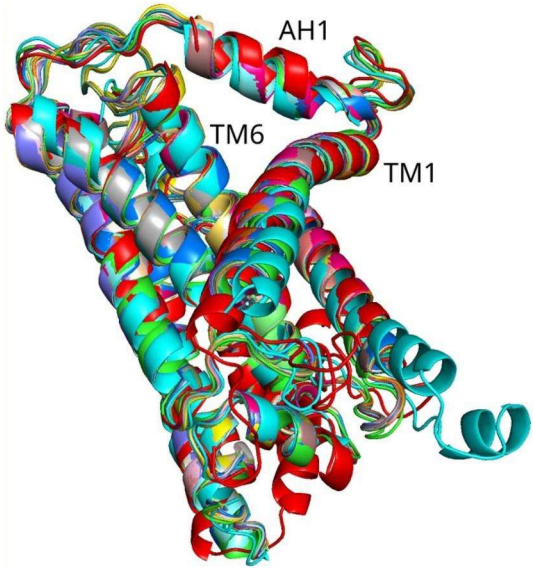

Fig. 4.2 Overlap of all 23 chain-H structures. The bottleneck is formed by the crossing of three helices: TM1, AH1, and TM6 of ND1/H/ Nqo8 subunit. The crystal structure of bacterial (T. thermophilus) is shown in red and appears to be the most open among all structures analyzed. The shown structures include different organisms and different so-called “open” and “closed” states of the enzyme [3, 11]

Recently, the range of the available structures has been significantly expanded [3, 11–13]; several structures, both X-ray and cryo-EM, now indicate different conformational states that the enzyme assumes during its catalytic cycle [3,11]. Presumably, the structures capture quasi-stable states, with significant thermal population fraction that reflect different conformations; for example, in some structures the angle between the membrane and the peripheral arms changes as much as 6°–7°, or significant changes are observed inside of the Q-binding cavity. Yet, the bottleneck in all structures available (we analyzed twenty-three such structures) are about the same, as shown in Fig. 4.2.

4.2.3 The bottleneck is closed in all resolved structures

We showed previously that taken as in the pdb structure, the bottleneck is essentially closed. We demonstrate this by calculating the barrier of crossing the bottleneck structure. This is done in the following manner. (Additional probes were explored in Ref. [28]).

Barrier Simulations

The MD simulation details are given in SI and are the same as in Ref. [28] Briefly, the protein was incorporated into POPC membrane. The quinone was placed near the entrance of Complex I, and after equilibration, was pulled into quinone cavity. We also pulled quinone out of the quinone cavity. The energy and the pulling force were measured along the pulling trajectory. Both ubiquinone and menaquinone with various tail lengths were simulated, see details in Ref. [28]. To improve statistics, focused MD simulations on a restricted system that involved only the residues of the bottleneck (Fig. 4.1) were used. (For additional simulation details, see MD Methods in SI.)

Using pulling trajectories, we calculated the Helmholtz work (or Helmholtz free energy, W) to cross the bottleneck. In addition, we calculated so-called Jarzynski Averaged (JA) work [30]. Here the conditions of simulation are different from what is assumed in the JA work; however, we find it useful to consider this type of averaging as it emphasizes trajectories with minimal work and thus selects (or filter out) the "optimal" trajectories. As such, JA is sensitive to qualitative changes along the trajectory, such as the entrance of the headgroup into the bottleneck or the passage of individual methyl groups of isoprenoid tail of ubiquinone, which show up as small bumps on the JA curves, see Fig. 4.3 below.

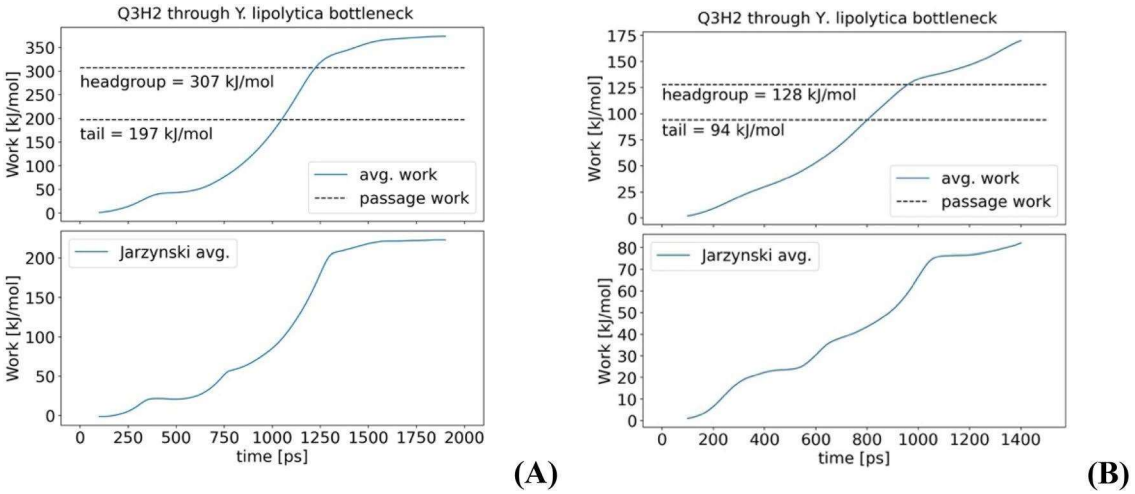

(A) **(B)**

Fig. 4.3 The average work along the pulling trajectory of ubiquinone (reduced, Q3H2, with 3 isoprenoid units) through the bottleneck of the Q-chamber in Y. lipolytica enzyme. The values under dotted lines give corresponding energy barriers for the headgroup and the two isoprenoid units of the tail passage. Lower panels show JA work along the pulling trajectory. A All atoms are strongly restrained as in pdb structure. B Backbone atoms are weakly restrained by 50 kJ mol−1 Å−2, and side-chain atoms by 10 kJ mol−1 Å−2 (a hydrogen bond, for comparison, is about 20 kJ/mol)

Here the goal was to probe the bottleneck passage in the structures given directly by the reported X-ray or cryo-EM pdb and to see if conformational changes are needed for the passage.

Therefore, the backbone atoms were restrained to the positions given by the pdb structures, and different strengths of restraint were probed. Asp of the bottleneck was protonated in our simulations. Typical results are shown in the following figure.

Figure 4.3 shows a typical example of the average work of bottleneck crossing by the reduced quinone, Q_3H_2, in yeast *Y. lipolytica* enzyme. (Most simulations were done with 3-isoprenoid unit tail ubiquinone, half-inserted in the Q-chamber; due to repetition of the tail structure, the Q_{10} results could be inferred from the data.) Here the cryo-EM structure gives the initial position of the quinol (reduced) in the Q-cavity. We calculate the barrier to move the quinone in the structure captured by cryo-EM. The dotted lines in the figure correspond to so-called "first passage" work, i.e. work required to find and enter the bottleneck by the headgroup of QH_2 and moving the methyl groups of the tail through the narrow entrance. In this case, two methyl groups were passing the bottleneck. The reduced form of QH_2 requires some 20 kJ/mol more energy to pass the bottleneck barrier. The found average work is obviously too high to pass the bottleneck without conformational opening of the structure.

As can be seen, the barriers are too high for the bottleneck passage both for the headgroup and for the tail. The weaker restraints on the structure were also probed, Ref. [28], but the barriers still remained too high to allow a suitable timescale of passage. A reasonable barrier that would give a *ms* timescale should produce a barrier no higher than some 30 kJ/mol, see Discussion.

The results for all other enzymes, including bacterial, mt ovine, and human enzymes, yield the same qualitative conclusion—the bottleneck is too narrow for the headgroup and even for the tail passage (yeast), as the barrier to cross the bottleneck is too high.

We conclude that as seen in the resolved structures, the size of the entrance is prohibitively small for the quinone molecule to pass either in oxidized or in the reduced form. There are slight variations in all structures examined, but in all structures the bottleneck is too narrow to be operational to admit quinone to the binding site. There are two possibilities: one is that quinone may never get out of the quinone cavity and works as an electron shuttle, another is that dynamic conformational changes open the bottleneck and allow quinone in and out. After exploring details of conformational dynamics below, we will discuss both possibilities in the last section of the paper.

4.2.4 Bottleneck opening in ND1 subunit

We now turn to exploring possible conformational openings of the bottleneck in ND1 subunit (without quinone, assuming binding by an empty enzyme). The idea is to first use the most accurate all-atomic force field and explore the elastic properties of isolated ND1 subunit itself; we then extend simulations to include other subunits adjacent to ND1 using a less accurate coarse-grained force field.

MD Simulations

In MD simulations, we use Gromacs [31] simulation package with CHARMM36 forcefield [32]. The initial coordinates of ND1 (Nqo8) subunit were extracted from the whole structure of *T. thermophilus* [4], and ND1 was simulated as described in MD Methods of SI. The Principal Component Analysis detailed below was applied to analyze the trajectories.

Principal Component Analysis (PCA) of MD Trajectories

The PCA method is described in Ref. [33]. Here we briefly summarize our approach. The PCA normal modes are collective coordinates $Q1$, $Q2$, … that are linear combinations of the usual (mass- weighted) Cartesian displacements of the protein atoms xi from their average positions: $Q_\lambda = \sum_i \ x_i S_{i\lambda}$ where $i = (a, \sigma)$, - a atom/site number, $\sigma = \ x, y, z$. The expansion coefficients $S_{i\lambda}$ are found by diagonalization of the correlation matrix $M_{ij} =< x_i x_j >$, where averaging $<\ldots>$ is assumed along the MD trajectory. After diagonalization, the diagonal elements of the correlation matrix give PC variances – the average values of squared amplitudes of PCA modes: $(diagM)_{\lambda\mu} = \sigma_{\lambda\mu} < Q_\lambda^2 >$.

The expansion coefficients $S_{i\lambda}$ are eigenvectors of the correlation matrix. The square values $P_{i\lambda} = (S_{i\lambda})^2$ can be considered as "probabilities" (after proper normalization) and $S_{i\lambda}$ as "amplitudes" for a given eigenvector. Atom participation value is defined by summing up $P_{i\lambda}$ for a given atom a over x, y, z components. The PCA modes are formally equivalent to familiar normal modes of an artificial harmonic system with the same displacement correlation matrix.

Each normal mode can be thought as describing coherent motion of all coordinates x involved in it:

$x_i(t) = S_{i\lambda}\, Q_\lambda$

$Q_\lambda = Q_{\lambda 0} cos(\omega_\lambda t\,)$

The picture of coherent motion is only qualitative because there is significant damping of the oscillations and the low-frequency modes are mostly in the overdamped regime. However, the picture of normal modes is a convenient way to think about the collective or correlated motions of a big system.

The frequency of each mode can be found from

$$\omega_\lambda = \sqrt{\frac{k_\lambda}{M_\lambda}}$$

The force constant $k_\lambda = \frac{k_B T}{<Q_\lambda^2>}$ and from kinetic energy (m_i are atomic masses):

$M_\lambda = \sum_i \ m_i S_{ij}^2$.

When the mass-weighted coordinates are used, the effective masses are all the same and can be normalized to unity. The timescales of the low-frequency modes (periods $T_\lambda = \omega_\lambda$) can be large and therefore difficult to access via direct MD. One can use these modes for probing possible large amplitude motions of the protein by artificially moving along one or several low-frequency modes, guiding direct MD, and thus more efficiently sample phase space. Also, it was suggested [34] that the functional or essential conformational changes of proteins most likely occur along with the low-frequency collective coordinates, as a low energy path for large change.

4.3 Results

4.3.1 The bottleneck opening is related to the soft collective modes of ND1

The Principal Component Analysis of an MD trajectory results in several collective modes Q_λ, which are graded and ordered by the magnitude of their elasticity-strength constant k_λ and frequency ω_λ; several such modes are listed in Table B1–B4 in SI (Appendix B). Different modes involve different types of collective motions (see selected mode animations in SI) and represent different types of collective deformations under external stress on the protein structure. Surprisingly, we find the very first mode, with the lowest elastic constant, involves structural elements of the bottleneck; namely, helices TM1, AH1, and TM2 and the two loops connecting them, as seen in Fig. 4.4 and corresponding animation, Movie B1, in SI. The involvement (or participation value) of specific amino acids in a given PCA mode is found as described in the Methods section, and the structural elements with the highest participation are represented by the color intensity in Fig. 4.4 (see also related figures and animations in SI). The animation of this mode opening the bottleneck is shown in Movie B1 in SI.

It is seen in Fig. 4.4 and Movie B1 in SI that the deformation along with the first PCA mode Q0 mainly involves helices TM1, AH1, and TM2 and the two loops connecting them. The unbending deformation of TM1 helix and the increased size of the bottleneck are the two most prominent features of the softest deformation mode of ND1. This mode also involves the opening of the so-called E-channel in H/ ND1-subunit, see S1 in SI. The timescale of this collective motion is 0.3 ns, Table B1; this is a slow motion, about thousand times slower than the usual molecular vibrations (e.g., CC bond). Details of several other modes are discussed later in the text, and further details are given in SI. Generally, we find that many low-frequency modes involve the motion of TM1 and AH1 helices, but their contribution is scaled by their amplitudes—the higher the frequency the lower the amplitude, and so is the contribution.

As the structural elements of the bottleneck—TM1, AH1, and TM6—correspond to the softest mode, it is clear that if external forces were applied to deform ND1 subunit, the deformation would firstly affect the bottleneck structure. Thus, the closure of the bottleneck can be expected if one assumes compressing, desolvation forces acting on the protein in the structure-resolution conditions or low temperature, which is particularly clearly seen in Movie B1 in SI.

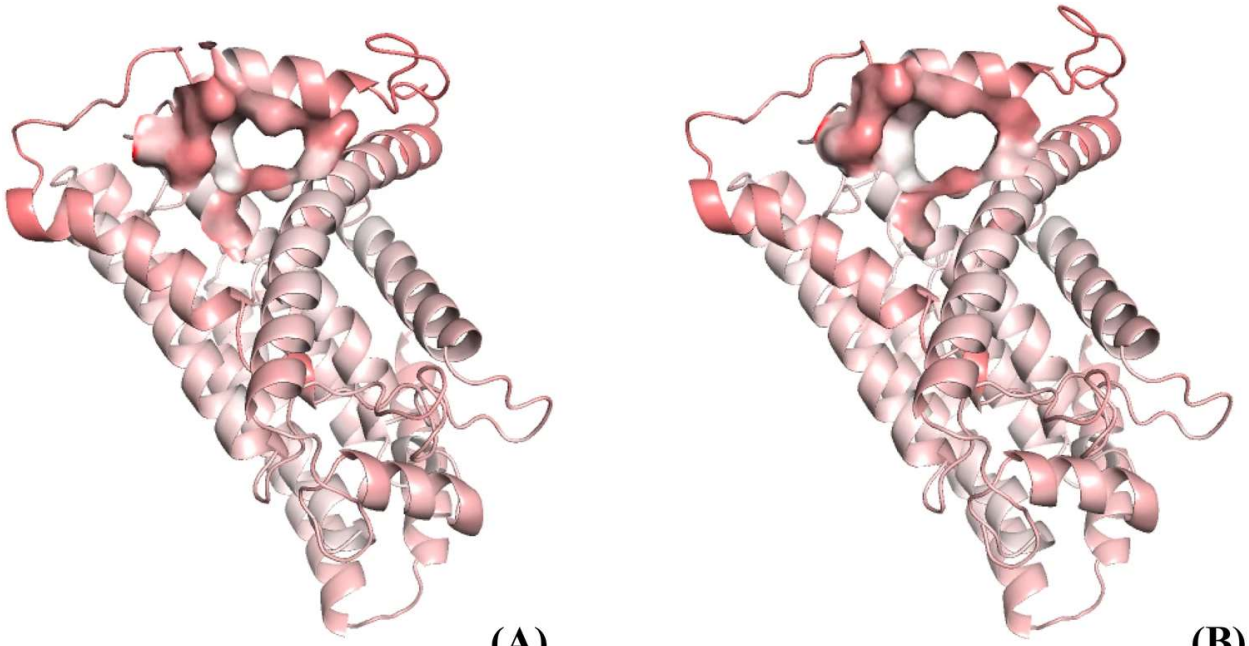

Fig. 4.4 The helix structure representation of H-subunit (ND1) of complex I and the entrance into Q-binding cavity. A Left, closed structure; B Right, open bottleneck structure. The open- ing occurs in deformation along the lowest frequency collective PCA mode (Q0), see Movie B1 in SI. The red color represents atoms and residues that con- tribute most to PCA mode Q0. The unbending deformation of TM1 helix and the increased size of the bottleneck are two most prominent features of Q0. Details of several other modes are discussed in the text, and further details are given in SI

4.3.2 The bottleneck participation spectra

To evaluate quantitatively the involvement of the bottleneck residues in a given collective mode, we calculate the so- called participation value; namely, for the bottleneck residues, A29, F28, P59, D62, A63, S66, I239, A242, L243, and M246, shown in Fig 4.1, we calculate the total probability of all atoms involved as $I_\lambda = \sum_{a \in bottleneck} P_{a\lambda}$. The resulting values then are scaled according to thermal amplitudes of the modes (eigenvalues of the PCA) and normalized to unity. Each mode thus is assigned the total bottleneck participation value, by which its contribution to the bottleneck conformations can be evaluated. For a group of modes, these data provide a spectrum of bottleneck participation. Alternatively, we directly calculate the variation of the size of the bottleneck (measured by its shortest dimension) for each mode, assuming the average thermal amplitudes of the modes.

Figure 4.5 shows the spectrum of the first 40 (out of more than 8000) modes. It is clear that the first few low-frequency modes are most important, based both on formal participation and in their variation of the bottleneck size. In SI (S2–S4) several animations of typical modes with high participation in the bottleneck are shown.

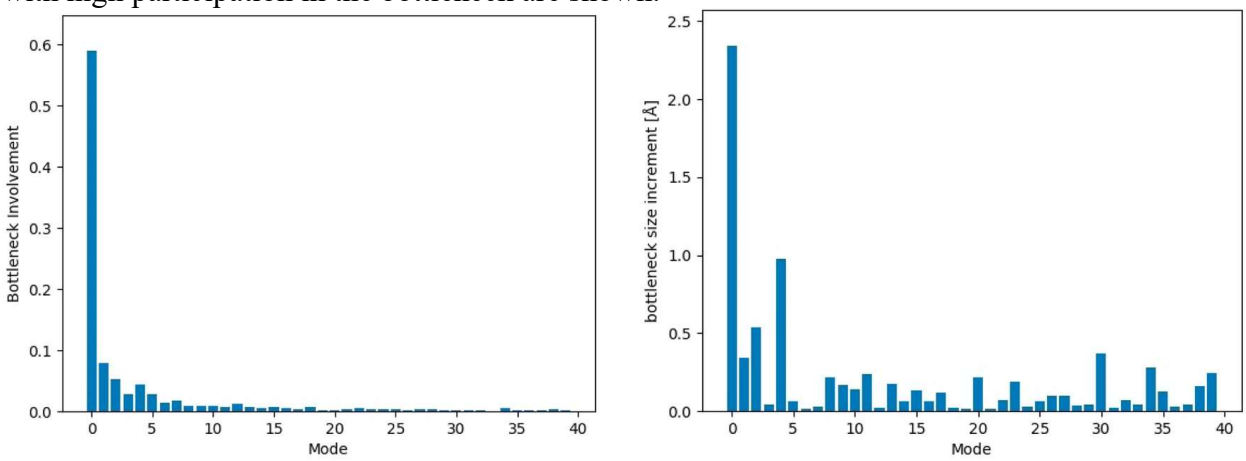

Fig. 4.5 Left: Bottleneck involvement in the first 40 modes. The higher modes are increasingly stiffer in character with less relevance to large-scale structural changes. Right: Bottleneck size increments for the first 40 modes

It is of interest to characterize the qualitative differences between different modes. If we neglect the difference in amplitudes and only focus on how coordinates are mixed in a collective mode (see Fig. B1), Modes 0, 4 and 5 show a higher bottleneck involvement than the rest of the first 10 low-frequency modes. Those modes are shown in animations in SI, Movies B1a-b. These examples clearly illustrate the different characters of the collective motions involved; surprisingly, many of them involve some elements of the bottleneck. We need to remember, however, that participation of different modes is scaled by their thermal amplitudes, and thus in practice we can focus only on a few first low-frequency modes, with the first mode clearly dominating, Fig. 4.5, left panel.

Indeed, the first mode Q0 shown in Fig. 4.4 already tells most of the story; namely, it is TM1 straightening and the related upside AH1 motion that are mostly responsible for the opening of the bottleneck. For a system involving tens of thousands of coordinates, to find only a few functionally relevant collective coordinates is quite remarkable. In the following section, we will explore how adjacent subunits affect this conclusion.

4.3.3 Structure of the open bottleneck state

An open bottleneck structure under Q0 deformation, see Fig. 4.4 and animation S1 in SI, can be envisioned as a possible open state of the bottleneck. On average, the changes are relatively small, but they involve rearrangement of essentially the whole subunit ND1 (as is particularly clearly seen in all-atom animation of Q0 in SI). As this subunit is in contact with other parts of the enzyme, including membrane subunit A (ND3), some changes in the equilibrium structure of the whole membrane part are expected in the open functional state. It is interesting that deformation under Q0 mode also opens the so-called E-channel in the ND1 subunit, see SI, Movie B1C. In simulations, the open state (maximum amplitude of Q0 quasi-harmonic deformation) occurs only in the course of thermal fluctuations, i.e. it is not a stable

state. This is in line with most recent structural data where no open state was detected, see Fig. 4.2; thus, the bottleneck open state occurs as a rare thermal fluctuation.

4.3.4 Stressed conditions of ND1 subunit

By design, in this section our simulations involved isolated ND1 subunit with no specific external forces acting on it (except for hydrophobic solvent—to model the inner part of the membrane, external pressure from the surrounding environment, including adjacent subunits, and some restriction of the terminal residues. This is still not an accurate representation of the enzyme context, which is examined in greater detail in coarse-grained simulations later.) This is done in part to explore the effect of the stress conditions [35] on the subunit when it is part of the whole enzyme structure; the stress conditions are due to inter-subunit forces, proper membrane solvation [35], etc. To evaluate the effect of boundary conditions imposed by the neighboring subunits, here we artificially remove the external forces that keep the ND1 subunit in the constrained configuration in the enzyme structure and monitor changes occurring in structural evolution.

In MD simulations of an isolated ND1, the overall global structural changes are already seen in the trajectories of the order of 100 ns (SI Fig. B5); but most prominently the change occurs already in the first 1–3 ns of the trajectories, which indicates the release of the stressed conditions of ND1 subunit in the enzyme structure. The SI provides detailed data that illustrate the overall evolution of the entire ND1 subunit upon release of the restraints. The main qualitative result is shown in SI Fig. B6. It turns out that already in the first few nanoseconds of the trajectory the helices forming the bottleneck are moving, with TM1 straightening up, and AH1 moving up to open the bottleneck. The further evolution results in structures with an overall greater opening of the bottleneck due to movement of the helices involved.

A clear tendency in the expansion of the structure to open the bottleneck is also seen in the low-frequency modes at different time-segments of a long trajectory, see SI Movies B2–B4, with corresponding data in SI Table S1–S4.

Having these insights, we next explore in greater detail how the ND1-surrounding enzyme structure affects the results described in this section.

4.4 Bottleneck in ND1 subunit in the context of the enzyme structure. Coarse-grained simulations

Here we put the ND1 subunit in the context of the entire enzyme structure. The question is how the adjacent subunits of ND1 are affecting its fluctuations. As simulations with all-atomic force-field are limited in timescales, here we apply less accu- rate but more efficient coarse-grained (CG) simulations using Martini force field [36, 37]. These simulations can be expected to yield a reasonable qualitative picture. The simulated system includes all subunits that can directly affect the motion of ND1 structure and include subunits ND1/Nqo8, Nqo6, 4, 9, and A, simulated in the membrane and solvent environment. (One should keep in mind that the bottleneck opening can in principle involve the whole structure of the protein; however, the available structure of the enzyme with the bound quinone, does not show such clear global con-formational changes. We, therefore, focused on the local changes—ND1 and surrounding subunits). The simulation details are given in SI MD methods.

Here we first compared the all-atomic simulations of an isolated ND1 subunit with the same simulations using Martini coarse-grained force field. Numerical comparison was done by

calculating the overlap of the lowest frequency PCA modes of both force-fields. Not surprisingly, quantitatively the PCA modes are quite different in the two force fields(the overlap is low); however, the qualitative comparison is still possible. Namely, the bottleneck opening in the low- frequency modes is clearly seen in both force-fields simulations and involves the same elements: TM1, AH1, and the loop between them among others. However, the amplitudes of motion of different elements are regulated by the details of the force fields, which are quite different in the two cases. In particular, the coarse-grained Martini involves the phenomenological pairwise rubber band restraints on the sites (5 kJ/mol/Å [2]) within each subunit, which in the long-term simulation keeps the overall structure as it appears in the initial pdb; but at the same time there is no direct analogy to such terms in the all-atomic force field. We explored different possibilities in the variation of this parameter, recognizing that in any case the results should be taken only as a qualitative indication of possible dynamic behavior of the system. We then explored PCA modes of a multi-subunit system.

A typical qualitative picture is shown in Fig. 4.6; it is seen that the lowest frequency PCA mode, as indicated by our participation value rendered in color, mostly involves the structural elements of the bottleneck: TM1, AH1, and TM2, essentially the same as in all-atomic simulations. This is interesting and unexpected, at first sight, as neighboring subunits do restrict ND1 motions—but obviously not as much as could be expected. Therefore, these simulations confirm and validate results from the previous section of all-atomic simulations of isolated ND1 with an “effective” artificial environment of ND1.

Overall, these results indicate that thermal fluctuations indeed mostly affect the bottleneck structure, even in the enzyme context, providing the needed opening states along the dynamic trajectory. In the following, we discuss the mechanism of the bottleneck passage that involves these rare fluctuations.

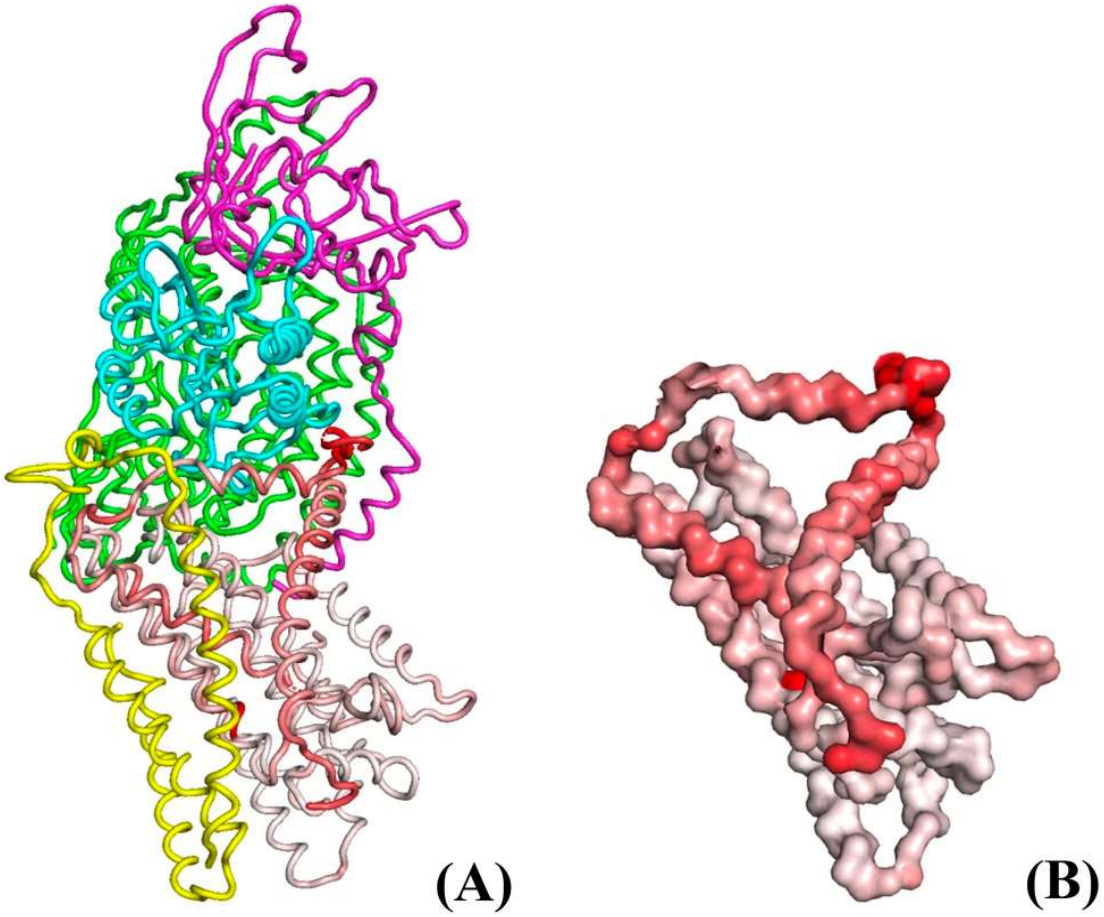

Fig. 4.6 CG PCA lowest-frequency mode of the structure of ND1 (B), and (A) with additional subunits: A (yellow), 6 (cyan), 4 (green), and 9 (magenta), all shown in (A). Red color intensity corresponds to elements with high participation in the Q0 PCA mode. The open structure resulting from the full amplitude Q0 PCA mode is shown

4.5 Discussion and conclusions

4.5.1 The bottleneck is too narrow for a free passage. The eye of a needle

Here and previously [28], we showed that in five published structures of complex I—bacterial T. thermophilus, yeast Y. lipolytica, and three mammal, mice, ovine, and human, the bottleneck at the entrance of the quinone chamber is too narrow for a quinol or quinone to pass through it. Most recent additional structures of different conformational states show that the bottleneck in all available structures (twenty-three analyzed so far) is about the same and, therefore, impossible for the quinone to get in or out of the binding cavity unless driven by a conformational changes that presumably occur in the course of thermal fluctuations of the enzyme. This is confirmed by MD simulations of the barrier formed by the narrow entrance in an intact pdb structure. Moreover, the bottleneck appears to be too narrow even for a passage of the isoprenoid tail of ubiquinone in the case of the yeast enzyme, although one quinone molecule is seen as stuck half-way to the binding site in the yeast structure. The shuttle model, where one quinone molecule never gets out of the binding cavity appears to be unlikely, as we discussed previously [28].

The conclusion is that fluctuations of the structure not reflected in the pdb structures have to be included in the complete picture. In addition, minor deformations may also result from artificial, out of the membrane conditions [38], both in X-ray or cryo-EM, as the lack of proper membrane solvation of the enzyme [38] can deform the molecule in such a way that the intrinsically narrow entrance path becomes even smaller, impossible for actual passage of quinone and render enzyme appear to be non-functional. To open the entrance of the quinone chamber, some conformational changes are needed; however, the nature of these changes given their collective character is not trivial.

Here, using PCA modes of the MD trajectories of the bacterial enzyme, we have identified collective conformational changes that open the quinone chamber bottleneck. The main qualitative result is shown in Fig. 4.4, and in animation S1 in SI. The changes involve mostly TM1 helix, which straightens up, AH1 helix, which moves up to open the structure, and the loop between them; but in general, the changes involve rearrangement of a larger part of the enzyme. The simulations allow to reconstruct to some extent the elusive structure of ND1 in which the bottleneck is open. It is now clear (given most recent structural data) that the open state is unstable, producing a very low population, which is not readily captured in plunge-freezing of cryo-EM.

4.5.2 Quantitative estimates of timescales and barriers

The barrier crossing rate by a quinone molecule at the bottleneck can be estimated from the transition state theory; namely, the rate of a single barrier crossing—be it a headgroup, or one of the methyl groups of the isoprenoid tail, is given by the following expression:

$$k \approx \frac{D_q}{L_0^2} 10^{-\frac{V_b}{ln(10)RT}}$$

where D_q is the diffusion coefficient of quinone in the membrane environment, $D_q \sim 10^{-7} - 10^{-8}$ cm^2/s [21], and L_0 is a characteristic length of the barrier width [39]. The first factor (assuming barrier width 1–3 Å) is of the order of 10^8 s^{-1}. The exponential factor should be greater than 10^{-5}; as ln10RT=6 kJ/mol, Vb ≈ 30 kJ/mol or less. All our energy barriers are in gross excess of this critical value, thus in the functional state the bottleneck structure should be opened.

Although it is not clear to what extent the structure is opened in the transition state, it appears unlikely that the structure would be open only for a free tail passage while

blocking the headgroup. This is because the methyl groups of isoprenoid tails present almost the same challenge of passing the narrow bottleneck as the headgroup, as our calculations suggest. The effective diffusion constant for isoprenoid tail movement through the bottleneck is modified by the same exponential factor discussed above and is too small to be operational in all structures examined. Thus, taken as is in pdb structures, the bottleneck is too narrow to be operational even for the shuttle model [40].

4.5.3 The squeeze-in model and the kinetic analysis

It is clear that conformational changes are needed to open the bottleneck for the diffusion-like motion of the quinone through the bottleneck; presumably, they occur in thermal fluctuations along the low-frequency PCA modes described above. These fluctuations would allow individual random-walk steps to occur in the overall diffusion- like motion. In such a squeeze-in mechanism, of getting through the eye of a needle, the overall entrance remains to be relatively narrow, which allows for tight control of the entrance of the binding cavity. This could provide desirable selectivity of admission of quinone vs quinol, or vs other bulky molecules by the quinone cavity.

The available kinetic data [25] appear to support this conclusion. Consider the efficiency parameter defined as $\kappa_{BM} = k_{cat}/K_m$ for quinone binding and reduction, assuming Michaelis–Menten kinetics. Under the condition of $k_{cat} >> k_{dis}$, the efficiency parameter is the second-order rate constant that can be estimated as follows. (Alternative case $k_{cat} << k_{dis}$, i.e. the opposite to what we assumed in the above, is an unlikely scenario [28]) In 3D diffusion model [28, 41]

$$\kappa_{BM} = 4\pi r_0 \, D_q \, (N_A/10^3) P_r$$

Here the diffusion of the quinone head-group from the membrane internal medium to the entrance of the Q-tunnel is envisioned as a 3D process, see Fig. 4.1A. It is assumed that the binding site is a 3D sphere of radius r_0 (the rate is half of the above for a half-sphere), diffusion coefficient (for center of mass) of substrate is D_q, the Avogadro number is introduced for conventional units M^{-1} s^{-1}, and CGS units are assumed for r_0 and D_q. The factor P_r describes the probability that a substrate arriving at the binding site via diffusion will have a right orientation for binding, and/or that the binding site is open. The more intricate binding site configuration is, the smaller the probability P_r; this could be combined with the effective capture radius, r_0. However, the remaining part of probability P_r is the probability that the binding site is open.

An equivalent expression for 2D diffusion [42, 43] in the membrane plane gives qualitatively similar results. Here,

$$\kappa_{BM} = \frac{\pi \, D_q d_m \, (N_A/10^3) P_r}{ln(R_0/r_0)}$$

where d_m is the membrane width (of the order of 50 Å), and R_0 is the typical distance between substrate molecules in the membrane (for [Q]=10 mM, R0=10 nm). The factor in the denominator is never too large, and realistically is in the range of 5–7 for realistic r_0=1 Å, or somewhat less, assuming order of magnitude values. Given these values, the two expressions give qualitatively similar results for r_0=1 Å, and the expression is not sensitive to this parameter.

The diffusion coefficient D_q is assumed to be in the range [21, 41] of 10^{-7} to 10^{-8} cm^2/s for the substrates of our interest, but can be modified by the barrier at the bottleneck, as discussed earlier.

The above expressions predict rates that are in line with the available kinetic data. For example, for NADH oxidation reaction of Ref. [25] both theory and experiment give $k_{cat}/K_m = \kappa_{BM} \sim 10^7$, for r_0=1 Å and P_r=1 (no need to open the binding site). Similar values are obtained for AOX of Ref. [25].

However, for Q-reduction k_{cat}/K_m in Ref. [25] is much smaller and, depending on the length of isoprenoid tail, is in the range of 10^4 to 10^5. This significant reduction can be readily explained by an additional small factor P_r in the range of 10^{-2} to 10^{-3} or even smaller (effective reduction of the capture radius, r_0, would not produce such an effect). This could be rationalized by the difficulty of passing through a narrow entrance of the Q-channel and be interpreted as a small probability of the bottleneck open state.

At the same time, the difficulty of quinone accessing the reduction catalytic site and the relatively fast reduction of the FeS chain by NADH (that provide electrons for quinone reduction) should result in a (partially) reduced state of FeS clusters in the chain, which then can serve as a buffer of electrons reducing quinone. In such conditions, the redox potential of the FeS chain would be in equilibrium with that of NADH pool, i.e. around -320 mV, and thus reduction of quinone to produce semiquinone state appears to be quite possible, despite that the redox potential of the last FeS cluster in the chain N2, which reduces quinone, by itself is much more positive [24].

Supplementary Information

The online version contains supplementary material available at https://doi.org/10.1007/s43630-021-00113-y.

Acknowledgements

This work has been supported in part by the NIH research Grant GM054052 and BSF Grant No. 2018239 A19-3374(AAS). We are grateful to Dr. James Letts for stimulating discussions.

Declarations

Conflict of interest The authors declare no conflict of interest.

References

1. Sazanov, L. A. (2015). A giant molecular proton pump: Structure and mechanism of respiratory complex I. Nature Reviews Molecular Cell Biology, 16, 375–388.

2. Parey, K., Wirth, C., Vonck, J., & Zickermann, V. (2020). Respiratory complex I - structure, mechanism and evolution. Cur- rent Opinion in Structural Biology, 63, 1–9.

3. Gutierrez-Fernandez, J., Kaszuba, K., Minhas, G. S., Baradaran, R., Tambalo, M., Gallagher, D. T., & Sazanov, L. A. (2020). Key role of quinone in the mechanism of respiratory complex Nature Communications, 11, 4135.

4. Baradaran, R., Berrisford, J. M., Minhas, G. S., & Sazanov, L.A. (2013). Crystal structure of the entire respiratory complex I. Nature, 494, 443–448.

5. Fiedorczuk, K., Letts, J. A., Degliesposti, G., Kaszuba, K., Skehel, M., & Sazanov, L. A. (2016). Atomic structure of the entire mammalian mitochondrial complex I. Nature, 538, 406.

6. Letts, J. A., Fiedorczuk, K., Degliesposti, G., Skehel, M., & Sazanov, L. A. (2019). Structures of Respiratory Supercom- plex I+III2 Reveal Functional and Conformational Crosstalk. Molecular Cell, 75, 1131–1146.

7. Zickermann, V., Wirth, C., Nasiri, H., Siegmund, K., Schwalbe, H., Hunte, C., & Brandt, U. (2015). Structural biology. Mechanistic insight from the crystal structure of mitochondrial com- plex I. Science, 347, 44–49.

8. Parey, K., Haapanen, O., Sharma, V., Kofeler, H., Zullig, T., Prinz, S., Siegmund, K., Wittig, I., Mills, D. J., Vonck, J., Kuhlbrandt, W., & Zickermann, V. (2019). High-resolution cryo-EM structures of respiratory complex I: Mechanism, assembly, and disease. Science Advance, 5, eaax9484.

9. Agip, A. A., Blaza, J. N., Fedor, J. G., & Hirst, J. (2019). Mammalian $$x I through the Lens of Cryo-EM. Annual Review of Biophysics, 48, 165–184.

10. Guo, R., Zong, S., Wu, M., Gu, J., & Yang, M. (2017). Architecture of Human mitochondrial respiratory megacomplex. Cell, 170, 1247–1257.

11. Kampjut, D., & Sazanov, L. A. (2020). The coupling mechanism of mammalian respiratory complex I. Science, 370, 6516.

12. Bridges, H. R., Fedor, J. G., Blaza, J. N., Di Luca, A., Jussupow, A., Jarman, O. D., Wright, J. J., Agip, A. A., Gamiz-Hernandez, A. P., Roessler, M. M., Kaila, V. R. I., & Hirst, J. (2020). Structure of inhibitor-bound mammalian complex I. Nature Com- munications, 11, 5261.

13. Grba, D. N., & Hirst, J. (2020). Mitochondrial complex I structure reveals ordered water molecules for catalysis and proton translocation. Nature Structural & Molecular Biology, 27, 892–900.

14. Efremov, R. G., Baradaran, R., & Sazanov, L. A. (2010). The architecture of respiratory complex I. Nature, 465, 441–445.

15. Sazanov, L. A., & Hinchliffe, P. (2006). Structure of the hydrophilic domain of respiratory complex I from Thermus thermophi- lus. Science, 311, 1430–1436.

16. Tocilescu, M. A., Zickermann, V., Zwicker, K., & Brandt, U. (2010). Quinone binding and reduction by respiratory complex Biochimica et Biophysica Acta, 1797, 1883–1890.

17. Cabrera-Orefice, A., Yoga, E. G., Wirth, C., Siegmund, K., Zwicker, K., Guerrero-Castillo, S., Zickermann, V., Hunte, C., & Brandt, U. (2018). Locking loop movement in the ubiquinone pocket of complex I disengages the proton pumps. Nature Communications, 9, 4500.

18. Stuchebrukhov, A. A. (2018). Redox-driven proton pumps of the respiratory chain. Biophysical Journal, 115, 830–840.

19. Stuchebrukhov, A. A. (2019). Kinetics and efficiency of energy- transducing enzymes. The Journal of Physical Chemistry B, 123, 9456–9465.

20. Kaila, V. R. I. (2018). Long-range proton-coupled electron trans- fer in biological energy conversion: towards mechanistic under- standing of respiratory complex I, J R Soc Interface 15, Article ID:20170916.

21. Warnau, J., Sharma, V., Gamiz-Hernandez, A. P., Di Luca, A., Haapanen, O., Vattulainen, I., Wikstrom, M., Hummer, G., & Kaila, V. R. I. (2018). Redox-coupled quinone dynamics in the respiratory complex I. Proceedings of the National Academy of Sciences of the United States of America, 115, E8413–E8420.

22. Wikstrom, M., Sharma, V., Kaila, V. R., Hosler, J. P., and Hum- mer, G. (2015) New perspectives on proton pumping in cellular respiration, Chem. Rev. (Washington, DC, U. S.) 115, 2196–2221.

23. Sharma, V., Enkavi, G., Vattulainen, I., Róg, T., & Wikström, M. (2015). Proton-coupled electron transfer and the role of water molecules in proton pumping by cytochrome c oxidase. Proceed- ings of the National Academy of Sciences of the United States of America, 112, 2040–2045.

24. Hagras, M. A., & Stuchebrukhov, A. A. (2019). Concerted two- electron reduction of ubiquinone in respiratory complex I. The Journal of Physical Chemistry B, 123, 5265–5273.

25. Fedor, J. G., Jones, A. J. Y., Di Luca, A., Kaila, V. R. I., & Hirst, J. (2017). Correlating kinetic and structural data on ubiquinone binding and reduction by respiratory complex I. Proceedings of the National Academy of Sciences of the United States of America, 114, 12737–12742.

26. Agip, A. A., Blaza, J. N., Bridges, H. R., Viscomi, C., Rawson, S., Muench, S. P., & Hirst, J. (2018). Cryo-EM structures of complex I from mouse heart mitochondria in two biochemically defined states. Nature Structural & Molecular Biology, 25, 548–556.

27. Uno, S., Masuya, T., Shinzawa-Itoh, K., Lasham, J., Haapanen, O., Shiba, T., Inaoka, D. K., Sharma, V., Murai, M., & Miyoshi, H. (2020). Oversized ubiquinones as molecular probes for structural dynamics of the ubiquinone reaction site in mitochondrial respiratory complex I. Journal of Biological Chemistry, 295, 2449–2463.

28. Wang, P., Dhananjayan, N., Hagras, M., & Stuchebrukhov, A.A. (2021). Respiratory complex I: Bottleneck at the entrance of quinone site requires conformational change for its opening. BBA- Bioenergetics, 1862, 148326.

29. Gu, J., Wu, M., & Yang, M. (2017). Cryo-EM structure of human respiratory complex I. PDB. https://doi.org/10.2210/pdb22 15XTD/pdb

30. Liphardt, J., Dumont, S., Smith, S. B., Tinoco, I., Jr., & Bustamante, C. (2002). Equilibrium information from nonequilibrium measurements in an experimental test of Jarzynski's equality. Science, 296, 1832–1835.

31. Abraham, M. J., Murtola, T., Schulz, R., Páll, S., Smith, J. C., Hess, B., & Lindahl, E. (2015). GROMACS: High performance molecular simulations through multi-level parallelism from lap- tops to supercomputers. SoftwareX, 1–2, 19–25.

32. Huang, J., & MacKerell, A. D., Jr. (2013). CHARMM36 all-atom additive protein force field: Validation based on comparison to NMR data. Journal of Computational Chemistry, 34, 2135–2145.

33. David, C. C., & Jacobs, D. J. (2014). Principal component analysis: A method for determining the essential dynamics of proteins. Methods Molecular Biology, 1084, 193–226.

34. Amadei, A., Linssen, A. B., & Berendsen, H. J. (1993). Essential dynamics of proteins. Proteins, 17, 412–425.

35. Vanegas, J. M., Longo, M. L., & Faller, R. (2011). Crystalline, ordered and disordered lipid membranes: Convergence of stress profiles due to ergosterol. Journal of the American Chemical Society, 133, 3720–3723.

36. Bruininks, B. M. H., Souza, P. C. T., & Marrink, S. J. (2019). A practical view of the martini force field. Methods in Molecular Biology, 2022, 105–127.

37. Periole, X., & Marrink, S. J. (2013). The Martini coarse-grained force field. Methods in Molecular Biology, 924, 533–565.

38. Drose, S., Zwicker, K., & Brandt, U. (2002). Full recovery of the NADH:Ubiquinone activity of complex I (NADH:Ubiquinone oxidoreductase) from Yarrowia lipolytica by the addition of phos- pholipids. Biochimica et Biophysica Acta, 1556, 65–72.

39. Hammes-Schiffer, S., & Stuchebrukhov, A. A. (2010). Theory of coupled electron and proton transfer reactions. Chemical Reviews, 110, 6939–6960.

40. Sharma, V., Belevich, G., Gamiz-Hernandez, A. P., Rog, T., Vattulainen, I., Verkhovskaya, M. L., Wikstrom, M., Hummer, G., & Kaila, V. R. (2015). Redox-induced activation of the proton pump in the respiratory complex I. Proceedings of the National Academy of Sciences of the United States of America, 112, 11571–11576.

41. Stuchebrukhov, A., Schafer, J., Berg, J., & Brzezinski, P. (2020). Kinetic advantage of forming respiratory supercomplexes. Bio- chimica et Biophysica Acta (BBA) Bioenergy, 1861, 148193.

42. Georgievskii, Y., Medvedev, E. S., & Stuchebrukhov, A. A. (2002). Proton transport via the membrane surface. Biophysical Journal, 82, 2833–2846.

43. Georgievskii, Y., Medvedev, E. S., & Stuchebrukhov, A. A. (2002). Proton transport via coupled surface and bulk diffusion. The Journal of Chemical Physics, 116, 1692–1699.

A. Supplementary Information for first paper (Chapter 3)

Respiratory complex I: Bottleneck at the entrance of quinone site requires conformational change for its opening

Panyue Wang, Nithin Dhananjayan, Muhammad A. Hagras, and Alexei A. Stuchebrukhov*

Relation to a paper by Kaila et. al.[1]

The figure below shows the bottleneck and the region behind it – so called sites 2 and 2'. According to Ref. [1] the site just behind the bottleneck region has a dip in energy profile of some 8kcal/mol. The key point of the present paper is that there is a bottleneck in accessing the binding sites 2 and 2' inside the cavity

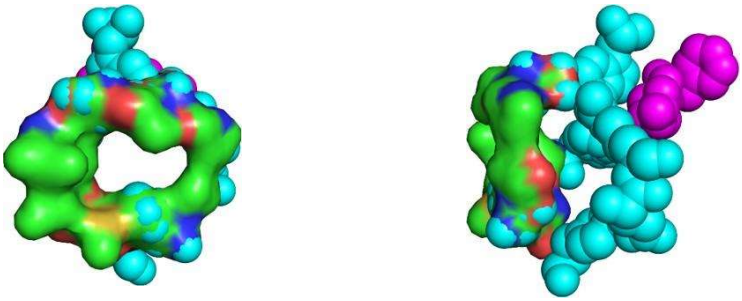

(A) (B)

Figure A0. The entrance bottleneck identified in this work (green surface), and the side chains of site 2 and 2' of Ref. [1], magenta (site 2) and cyan (site 2'). (A) front view from the membrane, (B) 90° - rotated around the vertical (z-) axes.

T. thermophilus results

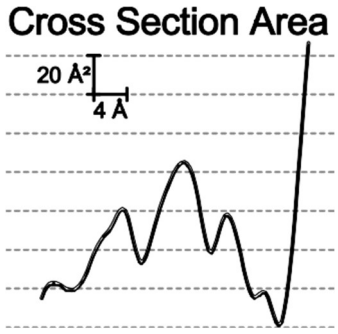

Figure A1: Cross section area along the quinone channel obtained by detailed calculation. The minimum of this cross-sectional analysis shows a singular global bottleneck in the geometry. (The last minimum on the right-hand side of the figure.)

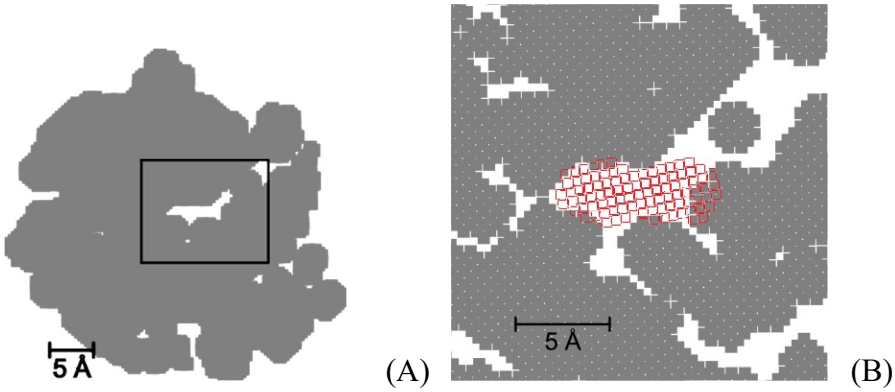

Figure A2: (A), simplified geometry analysis of the smallest opening cross section within the quinone chamber; white color refers to open space in that cross-section, gray is the protein body. (B), the cross section of quinone, open light red squares, is overlaid with that of the bottleneck, indicating that quinone does not fit the bottleneck.

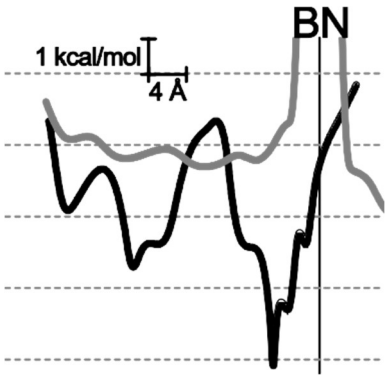

Figure A3: In black is the hydropathy curve based in kcal/mol. In gray is energy associated with configuration entropy. This term goes to infinity at the bottleneck, marked “BN”.

Additional Mole 2.0 analysis

In order to verify the results, the MOLE 2.0[2] tool was also used to independently probe and characterize the complex I ubiquinone cavity. As shown in Fig. A4, the MOLE2.0 cavity looks like a low-resolution representation of the cavity produced by our advanced analysis (see Fig. 3.1 in the text, and Fig. A13). Similar results are obtained with other commercially available programs, such as Caver Pymol plugin.

The Mole 2.0 tool uses atoms with van der Waals radii taken from the AMBER forcefield[3]. The cavity is computed by removing all computed tetrahedra that are too big to contain the *probe sphere.* In addition, all tetrahedra which are too small for the *interior threshold* are also removed. The remaining *Voronoi edges* are ranked such that edges that are closer to being equidistant from any atom center are favored. Djikstra's shortest-path algorithm is then implemented on the remaining edges in the graph[4]. Finally, a smooth three-dimensional spline is calculated for the shortest path, which serves as the basis for the tunnel centerline. The results were visualized with PyMol[5,6].

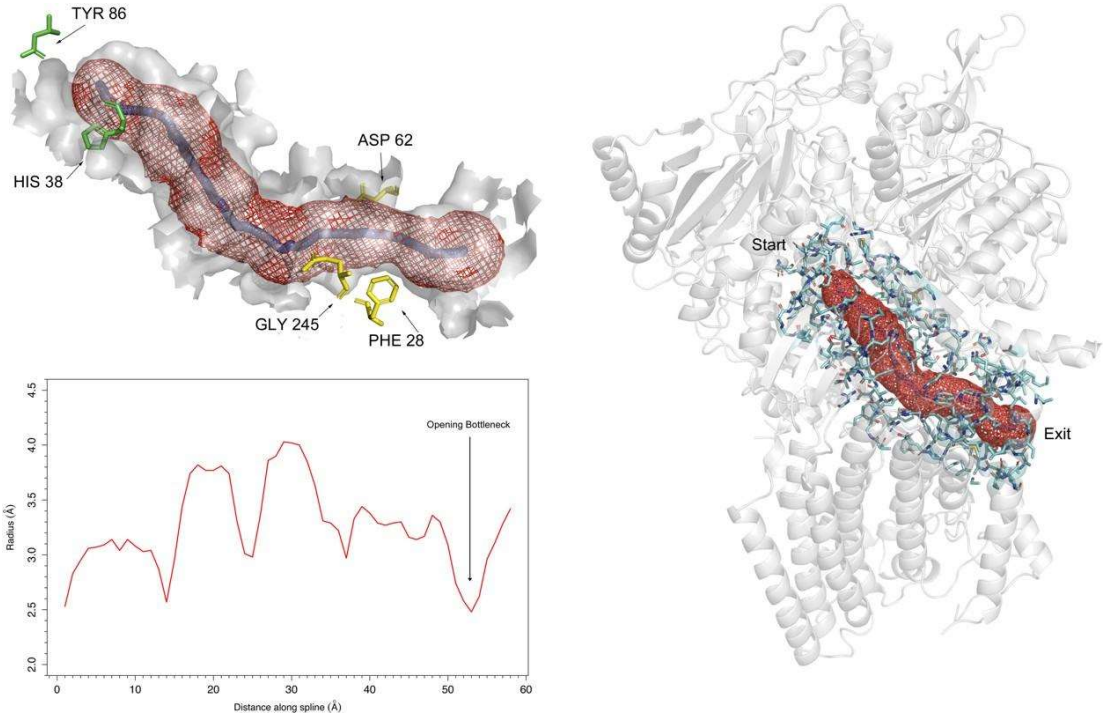

Figure A4: Visualization of the quinone reaction chamber in complex I as identified by MOLE2.0 and rendered with PyMol. Spline is rendered as a blue trace and the red mesh is a computed volume. Key residues near the binding site of the cavity are highlighted, as well as the constricting residues at the entrance to the cavity. A plot of the radius of the cavity clearly shows a bottleneck of ~2.5A near the opening.

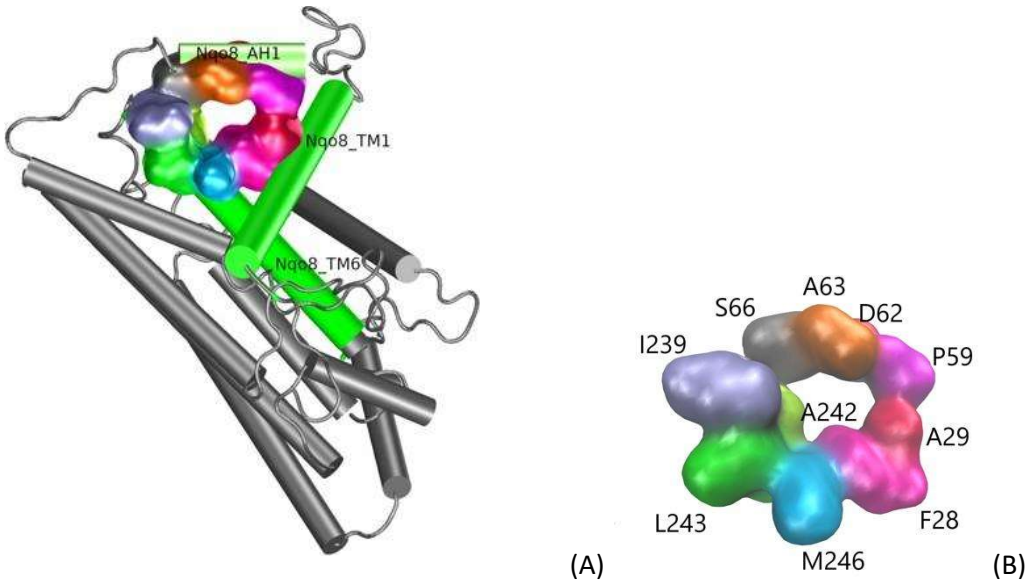

Figure A5: (A) The bottleneck is framed by the three helices Nqo8_TM1, Nqo8_AH1, Nqo8_TM6. (B) The 10 residues of the bottleneck shown by using surface rendering in VMD[7] and colored by residue.

MD Simulations details

In MD simulation, the pdb structure is first fed into CHARMM GUI an automated builder of protein membrane complexes [7]. The chains selected for building the model are the ones needed for modeling the Q-chamber. The membrane lipid chosen was POPC. Chimera[8] was used to place quinone near the entrance of Complex I. After the structure was built, using Gromacs[9], the system was energy minimized, temperature and pressure equilibrated with the CHARMM36 forcefield[10], and Swiss Param generated force field[11] for Q(n=1- 10)/DQ/MQ and their reduced analogues. During these equilibration steps the protein atoms were restrained to preserve as close to the crystal structure as possible. Keeping constraints in place Q was pulled into Q-chamber. The production simulations then pulled the Q out without restraints. To analyze the energy, the trajectories were rerun with the models constrained to the bottleneck of the entrance. To create the topology for the reruns the pdb2gmx utility using CHARMM36 forcefield was run on the residues identified for the bottleneck and modified to remove atoms that were not in the original simulation. The rerun trajectories were then analyzed for potential energies.

To improve statistics, focused MD simulations on a restricted system that involved only the residues of the bottleneck were used. In this case the simulation box is filled with an artificial hydrophobic (LJ) medium consisting of water with switched off charges. All the simulations were done under periodic boundary conditions and isotropic pressure coupling.

The pulling trajectories with slightly different conditions and different speed of pulling were used in the analysis. The restraints (20 to 40kJ $mol^{-1}Å^{-2}$) on the bottleneck residues were removed prior to pulling out, while keeping restrains on some atoms of the structure to prevent overall structure displacement. The Q was pulled out by the tail with a force of 25 kJ mol^{-1} $Å^{-2}$. This roughly corresponds to energetics of a hydrogen bond. Q was pulled out at 0.1 Å per ps; this is about ten times slower than the rate of water molecule diffusion in bulk water (D_w=10^{-5} cm^2/s)[12]. In a focused MD the pulling speed was further reduced by a factor of ten, to simulate adiabatic conditions for free energy evaluation.

Gromacs Energies

Several trajectories were analyzed. Below, results for THREE typical trajectories are shown.

Trajectory 1

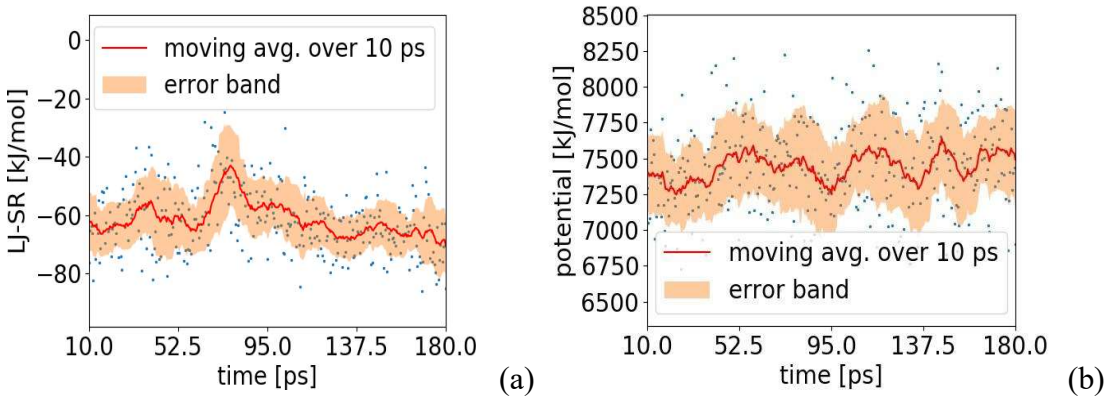

Figure A6. (a) Lennard-Jones potential energy along the 1st trajectory. The Lennard-Jones potential shows a bump of 20 KJ/mol between 60 ps and 120ps. (b) Total potential energy along the 1st trajectory. The total potential energy shows a bump of 250 KJ/mol from 40ps to 100ps. However, in addition there is a ringing of the total potential of roughly the same magnitude.

Trajectory 2

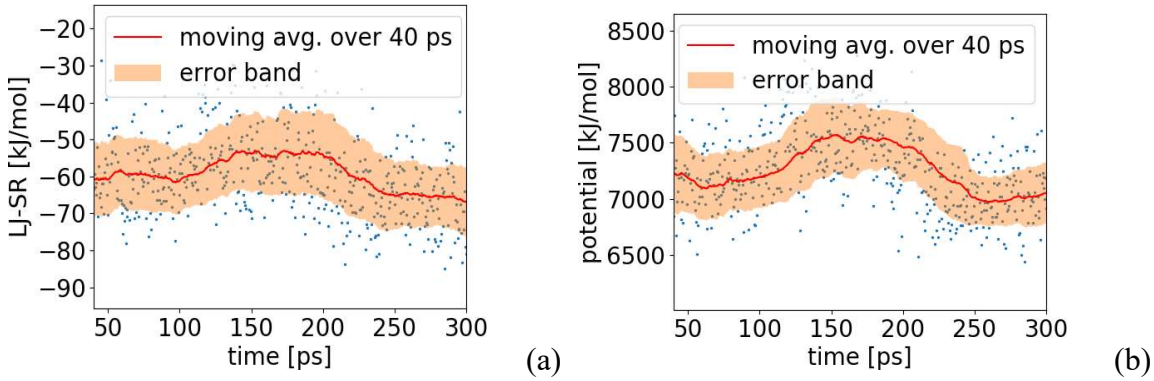

Figure A7. (a) Lennard-Jones potential energy along the 2nd trajectory. The Lennard-Jones potential shows a bump of 10 KJ/mol between 100 ps and 225ps. (b) The total potential energy along the 2nd trajectory. The total potential energy shows a bump of 250 KJ/mol between 100 ps and 225ps.

Trajectory 3

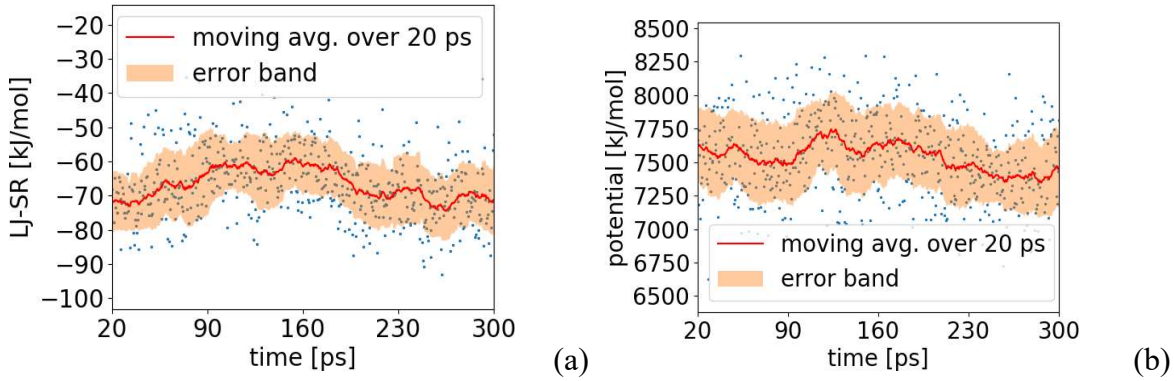

Figure A8. (a) The Lennard-Jones potential energy for the 3rd trajectory. The Lennard-Jones potential shows a bump of 10 KJ/mol between 50 ps and 250ps. (b) The total potential energy for the 3rd trajectory. The total potential energy shows a bump of 250 KJ/mol from 100ps to 250ps.

Relative deformation of the bottleneck along the quinone passage

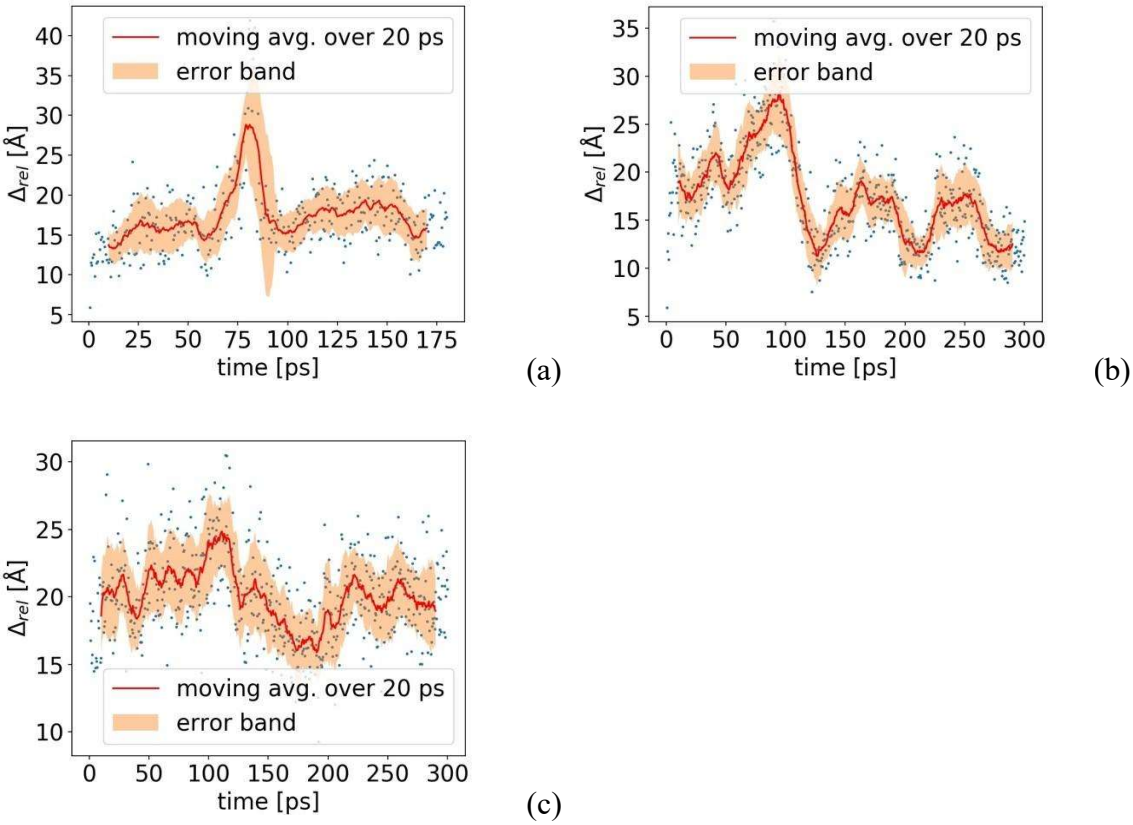

Figure A9.

(a) Relative deformation energy along the 1st trajectory. The bump is formed at 70 ps to 100 ps, where the relative energy increases from 15 to 29 then falls back to 15.

(b) 2nd trajectory. Three bumps are formed: first bump from 50 ps to 125 ps, second bump from 125 ps to 220 ps and third bump from 220 ps to 275 ps. The relative energy increases from 20 to 27 from 0 ps to 100 ps, then decreases to 12 at 125 ps. From 125 ps to 275 ps the relative energy fluctuates between 12 and 17.

Relative energy along the 3rd trajectory. A bump appears between 100 ps and 170 ps, with an increase in energy from 20 to 24, then the relative energy drops to 16.

Short axis distance along the pulling trajectory

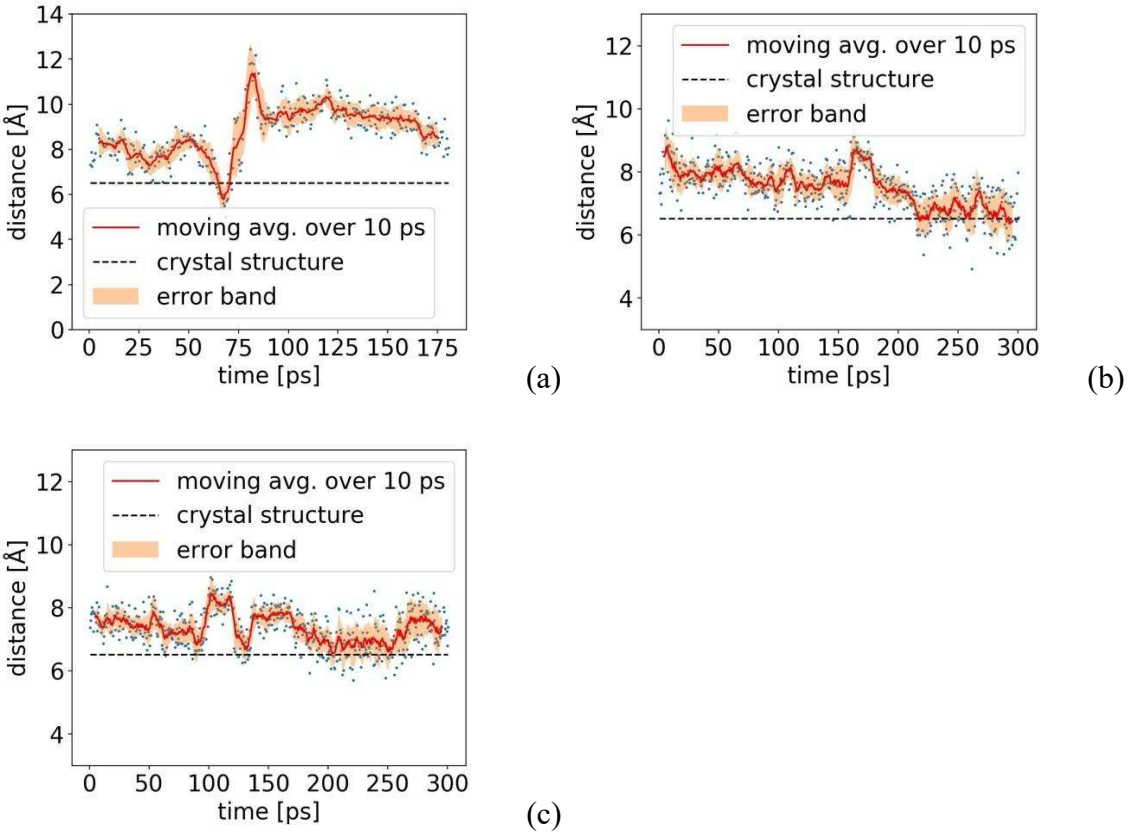

Figure A10.

(a) Short axis distance (see Fig. 3.2 in the main Text) along the 1st trajectory with a pulling rate of 200 Å/ns and no restraints on the system. At 74 ps, there is a sharp increase from around 6 Å to around 12 Å. Then the short axis relaxes to about 10 Å.

(b) Short axis distance analysis of the 2nd trajectory with pulling rate of 100 Å/ns and no restraints on the system. There is a small bump from 150 ps to 225 ps. Then the short axis recovers to about crystal structure level.

(c) 3rd trajectory with pulling rate of 100 Å/ns and no restraints on the system. Two bumps appear from 90 ps to 200 ps.

Root mean square distance along the pulling trajectory

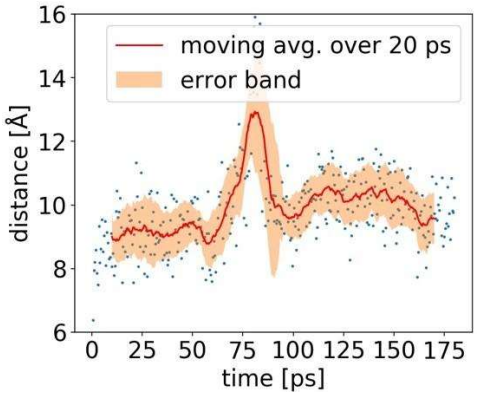

(a)

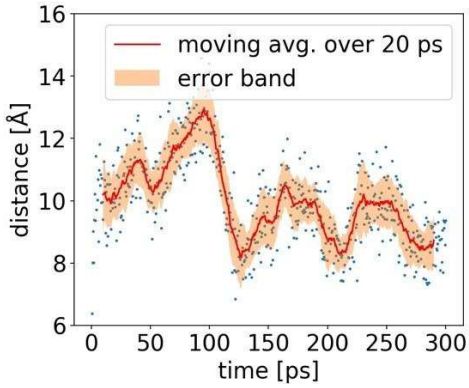

(b)

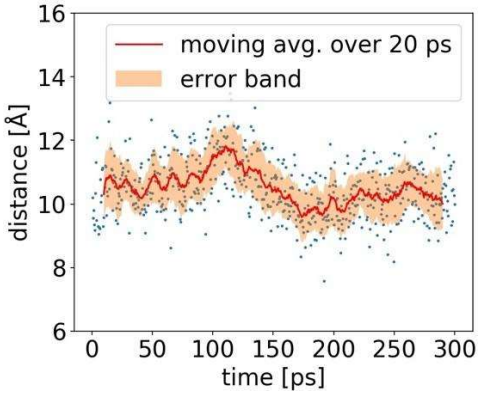

(c)

Figure A11.

(a) Root mean square distance (RMSD) along the 1st trajectory. A bump is formed from 70 ps to 100 ps, where the RMSD increases from 9 Å to 13 Å.

(b) RMSD of the 2nd trajectory. Three bumps are formed: first bump from 50 ps to 125 ps, second bump from 125 ps to 220 ps and third bump from 220 ps to 275 ps. The RMSD increases from 10 Å to 13 Å from 0 ps to 100 ps, then decreases to 8 Å at 125 ps. From 125 ps to 275 ps the RMSD fluctuates between 8 Å and 10 Å.

(c) RMSD of the 3rd trajectory. A bump appears between 100 ps and 170 ps, with an increase in RMSD from 10 Å to 12 Å, then the RMSD drops to 9 Å.

Inclusion of B-factors in the geometry analysis

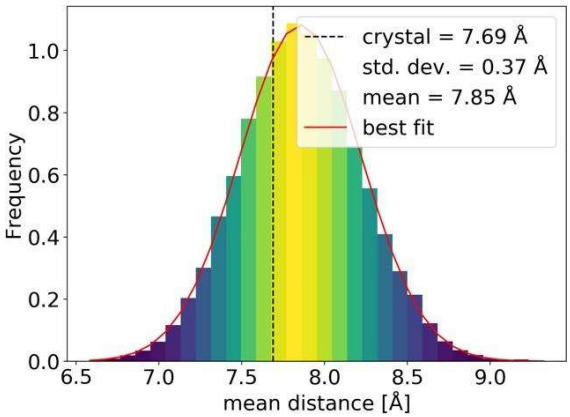

Figure A12. Distribution of the average of 28 distances between the bottleneck atoms from 10,000 configurations.

Each configuration is generated using NumPy, where the positions of atoms are randomly varied according to their B-factors. The mean distance calculated using the crystal structure coordinates is 7.69 Å. The mean distance from the randomly generated distribution is 7.85 Å, and the standard deviation is 0.37 Å. The mean distance ranges from 6.58 Å to 9.32 Å with a very low probability at the extremes.

Analysis of Y. lipolytica structure

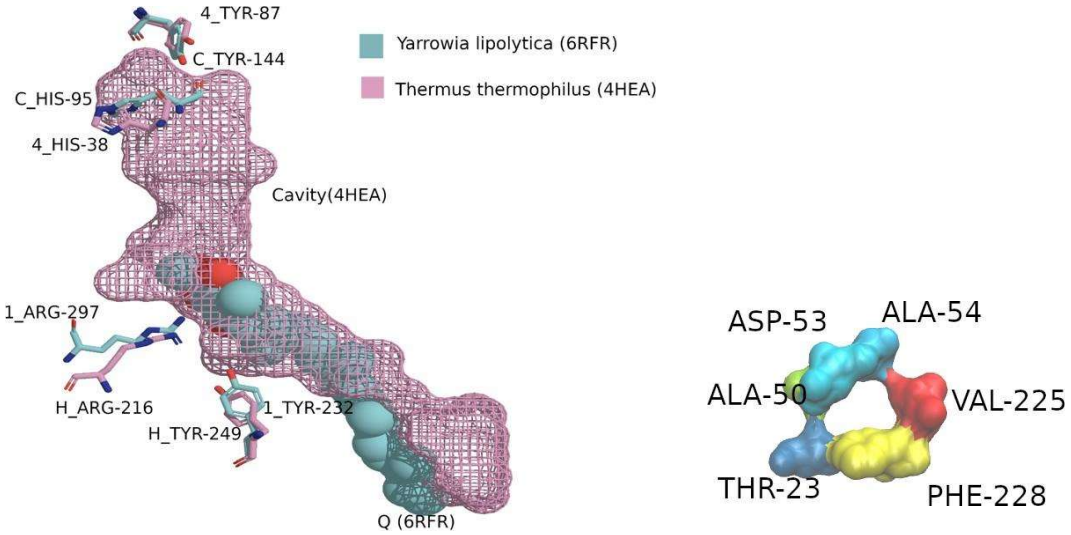

Figure A13. Left: Alignment of Yarrowia lipolytica(6RFR)[13] to Thermus thermophilus (4HEA)[14] taken from OPM15 database shows that the quinone molecule deposited in 6rfr.pdb lines up well with the cavity calculated from 4hea.pdb. Thermus thermophilus is colored in pink, while Y. lipolytica is colored in cyan. The alignment was done to best match C_TYR-144 to 4_TYR-87 and 1_TYR-232 to H_TYR-249 using a standard rigid body alignment algorithm16 implemented in Python[17]. The numpy[18], pandas[19], and BioPandas[20] packages were used to aid in numerically processing pdbs. The labeling of residues in the figure uses the scheme <chain_id>_<residue_name>-<residue_id> based on the pdb in this database. Hydrogens were not added to the structures for this picture. Pymol6 and POV-ray21 were used for rendering. Right: Bottleneck of Yarrowia enzyme from inside of the protein (opposite to Fig. 3.2). The bottleneck is too narrow to accommodate the head group or the free passage of isoprenoid tail of ubiquinone.

Force-work relation in the pulling simulations: T. thermophilus, Y. lipolytica, ovine, and human enzymes.

All structures are restrained as in the original pdb's using restraining force constant 250 kJ mol^{-1} $Å^{-2}$.

Average work and Jarzynski averaged work along the pulling trajectories. The dotted lines correspond to the barriers of the first passage of the headgroup or methyl groups of the isoprenoid tail. All energies are exceedingly high for a free passage of ubiquinone through the bottleneck. The quinone is either reduced (QnH2) or oxidized (Qn).

Y. lipolytica headgroup

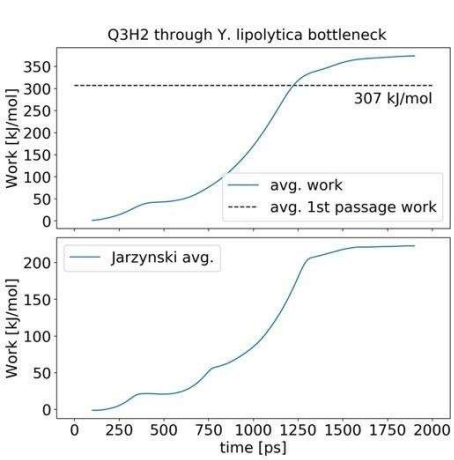

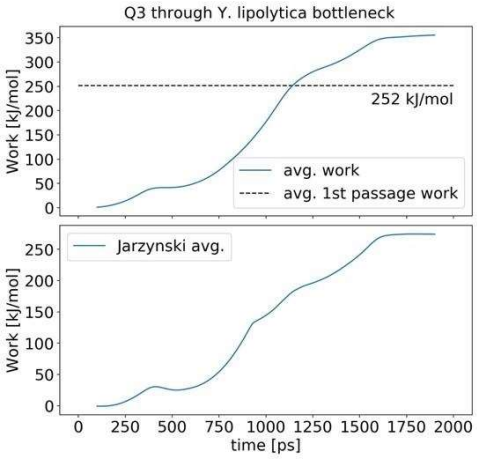

Y. lipolytica tail

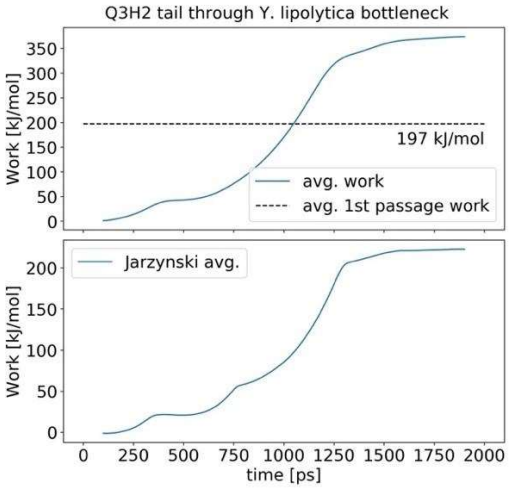

T. thermophilus

Menaquinone, MQ

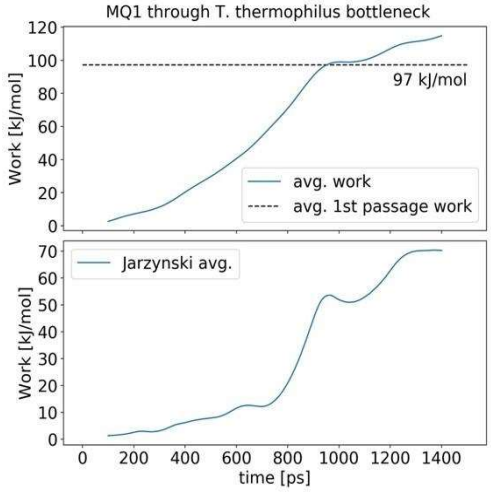

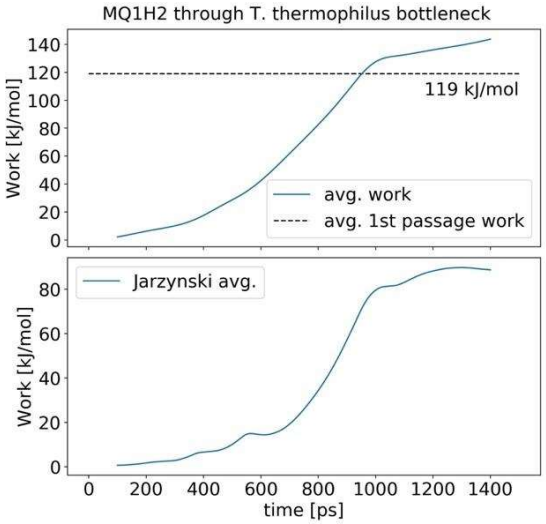

Decylubiquinone, DQ

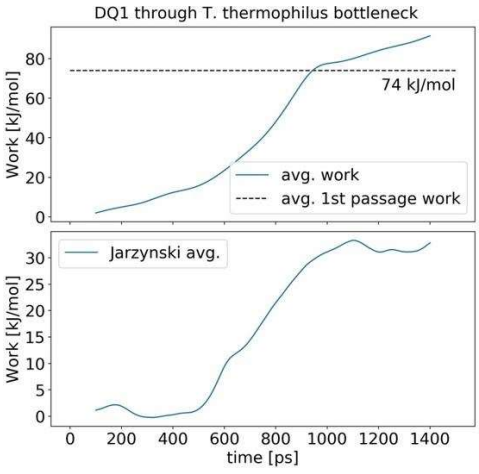

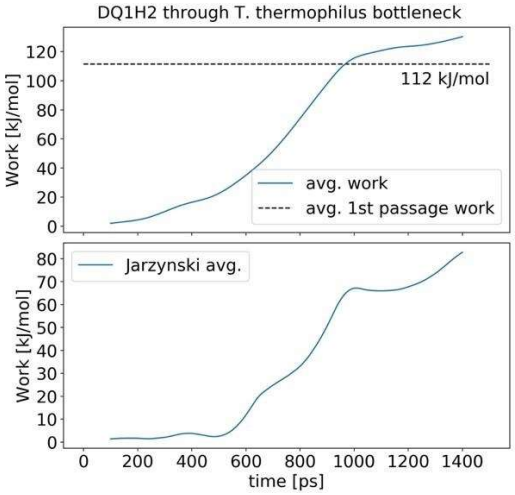

Ubiquinone, UQ

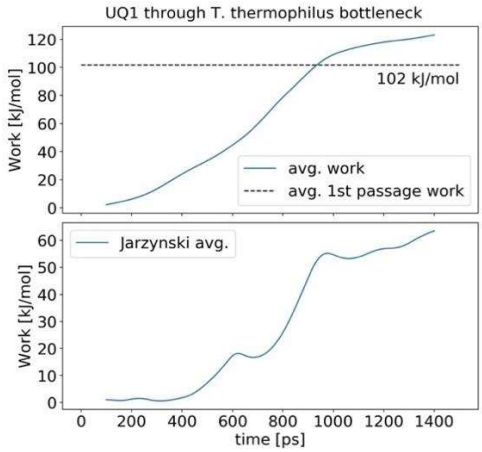

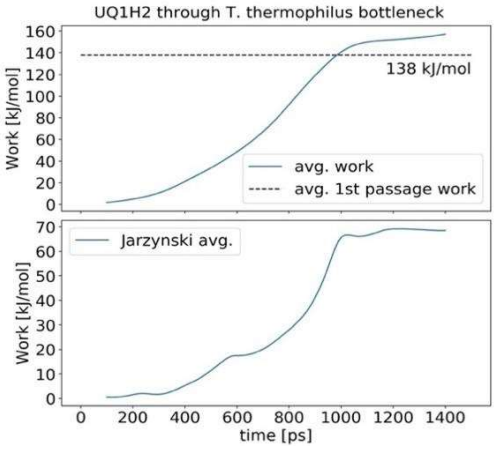

UQ Tail

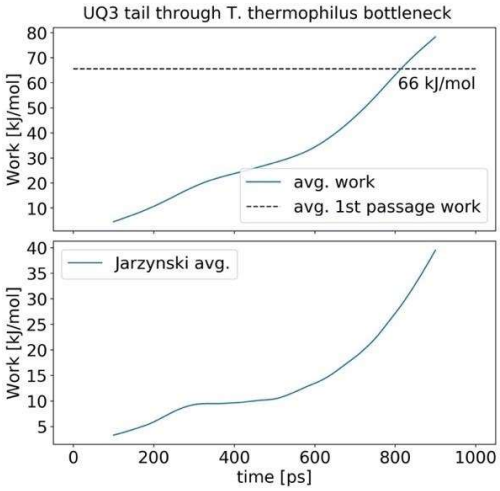

Ovine and Human enzymes

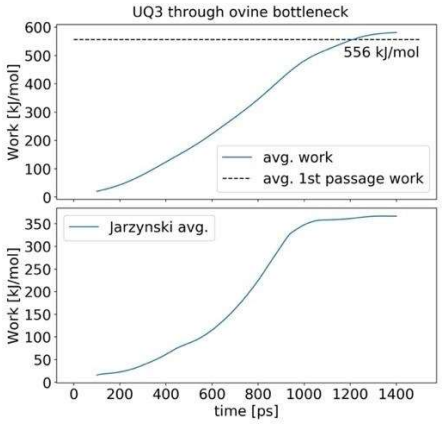

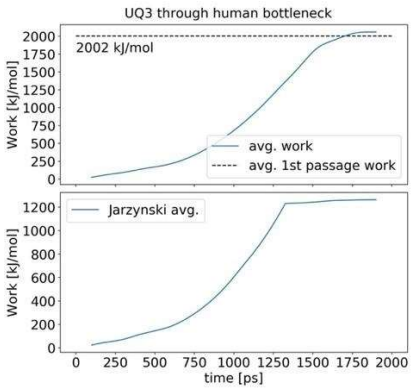

Bottleneck opening proposal

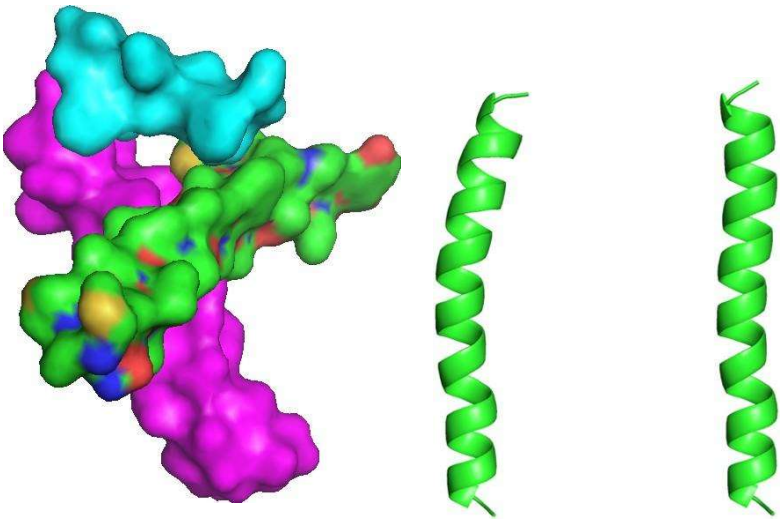

Figure A14. Left: three helices forming entrance (bottleneck) to Q-chamber, TM1 (green), AH1(cyan), TM6 (magenta). Right: TM1 helix is bent in the structure (left); when allowed to relax in molecular dynamics simulations, it straightens up (right) in about 100ps. The figure shows that the mutual scissor-like rotational motion of TM1 and TM6 would push AH1 up, via a loop between TM1 and AH1, and result in the opening of the bottleneck of the Q-chamber. In the open structure, TM1 is expected to take straight configuration shown on the far right.

SI References

[1] Warnau, J., Sharma, V., Gamiz-Hernandez, A. P., Di Luca, A., Haapanen, O., Vattulainen, I., Wikstrom, M., Hummer, G., and Kaila, V. R. I. (2018) Redox- coupled quinone dynamics in the respiratory complex I, Proc. Natl. Acad. Sci. U. S. A. 115, E8413-E8420.

[2] Berka, K., Hanák, O., Sehnal, D., Banáš, P., Navrátilová, V., Jaiswal, D., Ionescu, C.- M., Svobodová Vařeková, R., Koča, J., and Otyepka, M. (2012) MOLEonline 2.0: interactive web-based analysis of biomacromolecular channels, Nucleic Acids Research 40, W222-W227.

[3] Case, D. A., Cheatham, T. E., 3rd, Darden, T., Gohlke, H., Luo, R., Merz, K. M., Jr., Onufriev, A., Simmerling, C., Wang, B., and Woods, R. J. (2005) The Amber biomolecular simulation programs, Journal of computational chemistry 26, 1668-1688.

[4] Skiena, S. S. (2008) The Algorithm Design Manual, Springer Publishing Company, Incorporated.

[5] Schrodinger, LLC, The AxPyMOL Molecular Graphics Plugin for Microsoft PowerPoint, Version 1.0. (2010) The AxPyMOL Molecular Graphics Plugin for Microsoft PowerPoint, Version 1.0.

[6] Schrodinger, LLC, The PyMOL Molecular Graphics System, Version 1.3r1. (2010) The PyMOL Molecular Graphics System, Version 1.3r1.

[7] Jo, S., Kim, T., and Im, W. (2007) Automated builder and database of protein/membrane complexes for molecular dynamics simulations, PLoS One 2, e880.

[8] Pettersen, E. F., Goddard, T. D., Huang, C. C., Couch, G. S., Greenblatt, D. M., Meng, E. C., and Ferrin, T. E. (2004) UCSF Chimera--a visualization system for exploratory research and analysis, J. Comput. Chem. 25, 1605-1612.

[9] Abraham, M. J., Murtola, T., Schulz, R., Páll, S., Smith, J. C., Hess, B., and Lindahl, E. (2015) GROMACS: High performance molecular simulations through multi- level parallelism from laptops to supercomputers, SoftwareX 1-2, 19-25.

[10] Huang, J., and MacKerell, A. D., Jr. (2013) CHARMM36 all-atom additive protein force field: validation based on comparison to NMR data, J. Comput. Chem. 34, 2135-2145.

[11] Zoete, V., Cuendet, M. A., Grosdidier, A., and Michielin, O. (2011) SwissParam: a fast force field generation tool for small organic molecules, J. Comput. Chem. 32, 2359-2368.

[12] Stuchebrukhov, A., Schafer, J., Berg, J., and Brzezinski, P. (2020) Kinetic advantage of forming respiratory supercomplexes, Biochim. Biophys. Acta, Bioenerg. 1861, 148193.

[13] Parey, K., Haapanen, O., Sharma, V., Kofeler, H., Zullig, T., Prinz, S., Siegmund, K., Wittig, I., Mills, D. J., Vonck, J., Kuhlbrandt, W., and Zickermann, V. (2019) High-resolution cryo-EM structures of respiratory complex I: Mechanism, assembly, and disease, Sci Adv 5, eaax9484.

[14] Baradaran, R., Berrisford, J. M., Minhas, G. S., and Sazanov, L. A. (2013) Crystal structure of the entire respiratory complex I, Nature 494, 443-448.

[15] Lomize, M. A., Pogozheva, I. D., Joo, H., Mosberg, H. I., and Lomize, A. L. (2012) OPM database and PPM web server: resources for positioning of proteins in membranes, Nucleic Acids Res 40, D370-376.

[16] Horn, A. (1954) Doubly Stochastic Matrices and the Diagonal of a Rotation Matrix, American Journal of Mathematics 76, 620–630.

[17] Van Rossum, G. a. D., Fred L. (2009) Python 3 Reference Manual, CreateSpace.

[18] van der Walt, S., Colbert, S. C., and Varoquaux, G. (2011) The NumPy Array: A Structure for Efficient Numerical Computation, Computing in Science & Engineering 13, 22-30.

[19] McKinney, W. (2010) Data Structures for Statistical Computing in Python, In 9th Python in Science Conference (Millma, S. e. v. d. W. a. J., Ed.), pp 56-61, Austin, Texas.

[20] Raschka, S. (2017) BioPandas: Working with molecular structures in pandas DataFrames, The Journal of Open Source Software 2.

[21] (2004) Persistence of Vision Raytracer, 3.6 ed., Persistence of Vision Pty. Ltd.

B. Supplementary Information for the second paper (Chapter 4)

Quinone binding in respiratory complex I: The squeeze-in model for passing the entrance of the quinone site

Nithin Dhananjayan, Panyue Wang, Igor Leontyev, and Alexei A. Stuchebrukhov*

Movie B1. Left, the helix structure representation of H-subunit (ND1) of complex 1 and the entrance into the Q-binding cavity. Middle, same in all atom representation. The opening of the entrance bottleneck occurs in deformation along the lowest frequency collective PCA mode (Q0). The red color represents residues that contribute most to PCA mode Q0. The un-bending deformation of TM1 helix and the increased size of the bottleneck are two most prominent features of Q0. Center, same in all atom-representation. Right, deformation of E-channel along Q0. Note: To play video double click on the icon, the video opens in YouTube. To loop the YouTube video: if on PC right-click and choose "Loop" to loop the video; if on MAC, click (Control^+one mouse click).

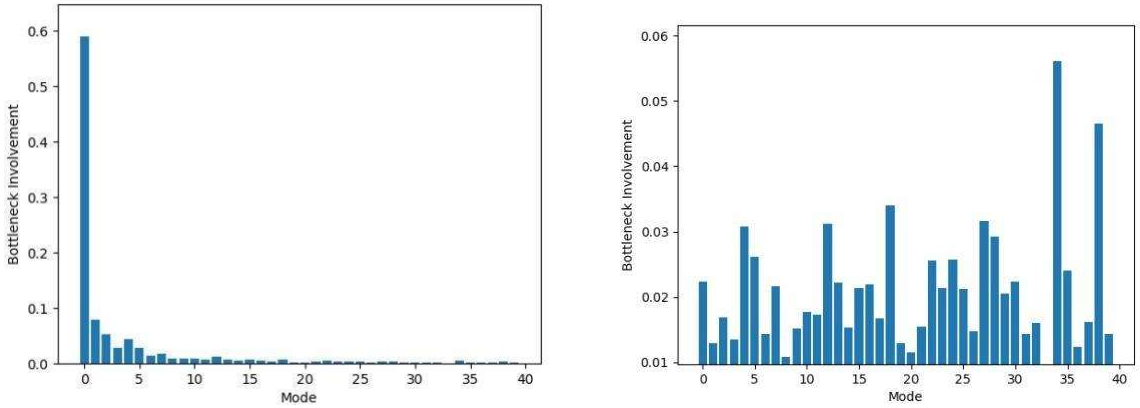

Figure B1. Left: Amplitude-scaled and normalized bottleneck involvement of PCA modes; Right: same without amplitude (eigenvalue) scaling and normalization – shown for better resolution of mode contribution. Spectrum of bottleneck involvement over first 40 modes of the 1ns run. To find the involvement of the bottleneck residues, A29, F28, P59, D62, A63, S66, I239, A242, L243, and M246, we calculate $I_\lambda = \sum_{a \epsilon \text{bottleneck}} P_{a\lambda}$. Then these values are amplitude(eigenvalue)-scaled and normalized. Higher modes are increasingly stiffer with less relevance to large scale structural changes. Mode 0, 4 and 5 show a higher bottleneck involvement than the rest of the first 10 modes, which indicates more prominent configuration changes of the bottleneck. These modes are shown in animation/Movies B1.

mode	eigenvalues (A^2)	spring constants (KJ/mol/A^2)	effective masses (g/mol)	angular frequencies (rads/s)	frequencies (Hz)	periods (s)
0	2.11E+03	1.16E-03	108.77	3.26E+10	5.19E+09	1.93E-10
1	4.87E+02	5.01E-03	110.60	6.73E+10	1.07E+10	9.34E-11
2	2.49E+02	9.78E-03	111.53	9.36E+10	1.49E+10	6.71E-11
3	1.65E+02	1.48E-02	109.31	1.16E+11	1.85E+10	5.40E-11
4	1.14E+02	2.15E-02	112.44	1.38E+11	2.20E+10	4.55E-11
5	8.71E+01	2.80E-02	113.14	1.57E+11	2.50E+10	4.00E-11
6	7.83E+01	3.11E-02	112.35	1.66E+11	2.65E+10	3.78E-11
7	6.58E+01	3.70E-02	110.71	1.83E+11	2.91E+10	3.44E-11
8	6.12E+01	3.98E-02	110.55	1.90E+11	3.02E+10	3.31E-11
9	4.76E+01	5.12E-02	111.07	2.15E+11	3.42E+10	2.93E-11

Table B1. First ten PCA modes characteristics of a 1ns MD trajectory.

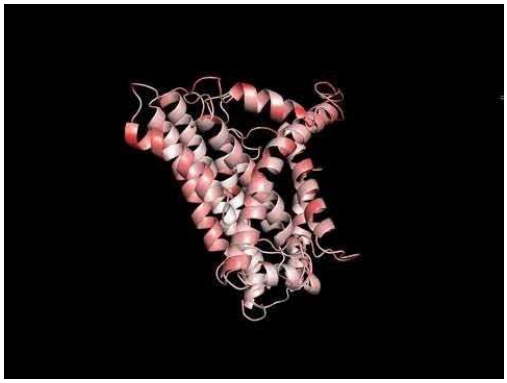

Movie B1ab. Mode 4 and Mode 5 of the 1ns run.

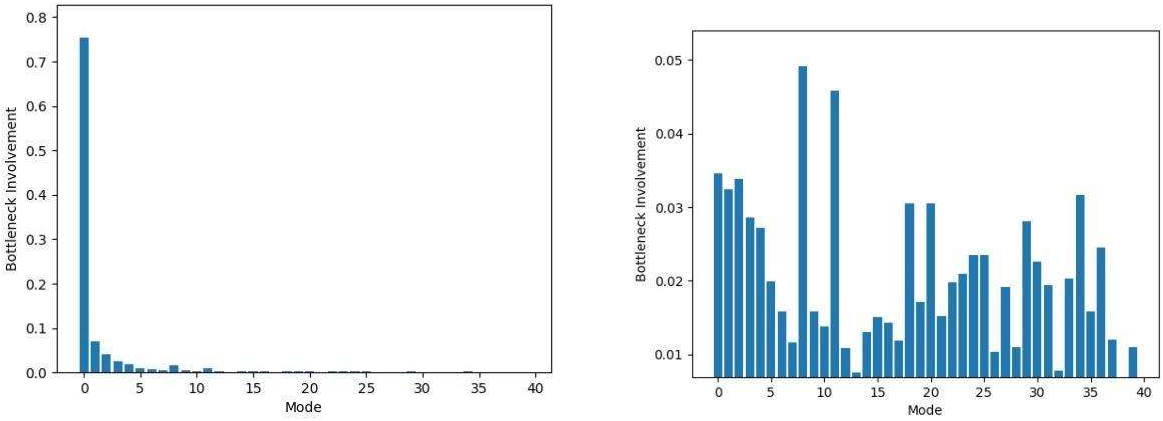

Figure B2. Similar to Fig. B1. Spectrum of bottleneck involvement over first 40 modes of the 3ns run. Mode 0, 8 and 11 show a higher bottleneck involvement than the rest of the first 40 modes, which are shown in animation/Movie B2 respectively.

mode	eigenvalue (A^2)	spring constants (KJ/mol/A^2)	effective masses (g/mol)	angular frequencies (rads/s)	frequencies (Hz)	periods (s)
0	4.41E+03	5.53E-04	106.78	2.27E+10	3.62E+09	2.76E-10
1	4.44E+02	5.49E-03	113.84	6.94E+10	1.11E+10	9.05E-11
2	2.43E+02	1.00E-02	108.45	9.61E+10	1.53E+10	6.54E-11
3	1.78E+02	1.37E-02	114.10	1.09E+11	1.74E+10	5.74E-11
4	1.37E+02	1.78E-02	110.59	1.27E+11	2.02E+10	4.95E-11
5	9.61E+01	2.53E-02	114.22	1.49E+11	2.37E+10	4.22E-11
6	8.00E+01	3.04E-02	114.90	1.63E+11	2.59E+10	3.86E-11
7	7.77E+01	3.14E-02	111.40	1.68E+11	2.67E+10	3.74E-11
8	6.80E+01	3.59E-02	118.01	1.74E+11	2.77E+10	3.60E-11
9	4.92E+01	4.95E-02	114.62	2.08E+11	3.31E+10	3.02E-11

Table B2. Computer output of the 3ns MD run. The periods of the modes show remarkable similarity to Table B1. Notice about same masses, as for mass-weighted coordinates (see text).

Movie B2a. Mode 0 of the 3ns run.

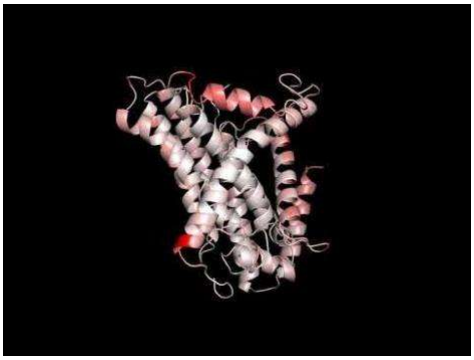

Movie B2b. Mode 8 of the 3ns run.

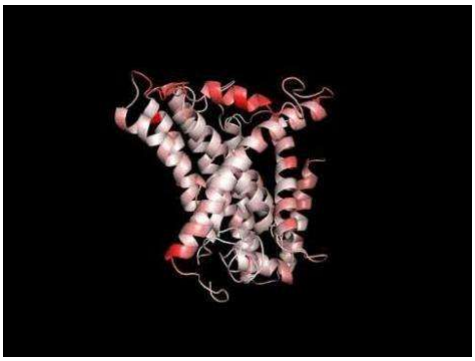

Movie B2c. Mode 11 of the 3ns run.

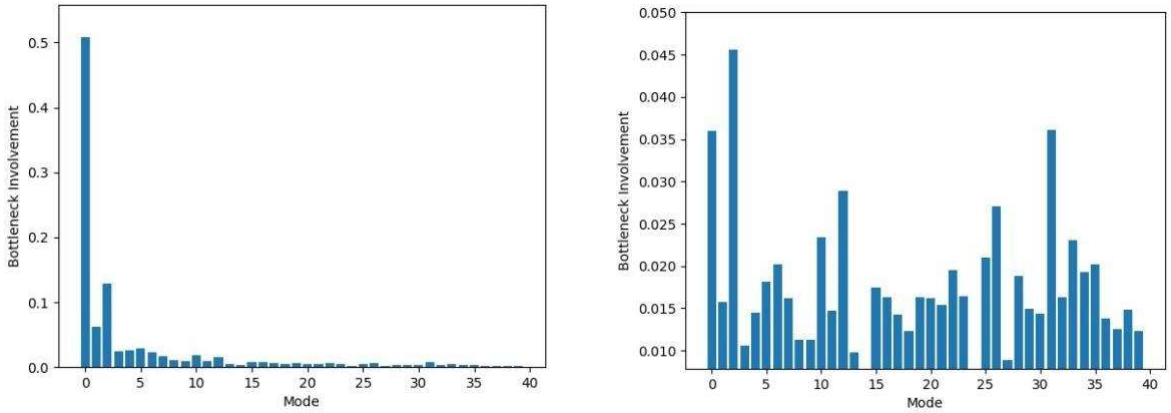

Figure B3. Spectrum of bottleneck involvement over first 40 modes of the 20-30ns window of the 60ns run. Mode 0 and 2 show a higher bottleneck involvement than the rest of the first 40 modes, which are shown in Movie B4a and B4b respectively.

mode	eigenvalues (A^2)	spring constants (KJ/mol/A^2)	effective masses (g/mol)	angular frequencies (rads/s)	frequencies (Hz)	periods (s)
0	8.31E+02	2.93E-03	108.26	5.21E+10	8.29E+09	1.21E-10
1	2.35E+02	1.04E-02	116.43	9.44E+10	1.50E+10	6.66E-11
2	1.66E+02	1.47E-02	110.05	1.15E+11	1.84E+10	5.44E-11
3	1.36E+02	1.79E-02	109.55	1.28E+11	2.03E+10	4.92E-11
4	1.05E+02	2.33E-02	112.38	1.44E+11	2.29E+10	4.36E-11
5	9.23E+01	2.64E-02	114.85	1.52E+11	2.41E+10	4.14E-11
6	6.58E+01	3.70E-02	119.18	1.76E+11	2.81E+10	3.56E-11
7	6.01E+01	4.06E-02	111.73	1.91E+11	3.03E+10	3.30E-11
8	5.69E+01	4.28E-02	122.40	1.87E+11	2.98E+10	3.36E-11
9	5.09E+01	4.79E-02	113.74	2.05E+11	3.27E+10	3.06E-11

Table B3. PCA analysis of the 20-30ns window of the 60ns MD run. The periods are close to the periods of the 1ns and 3ns runs.

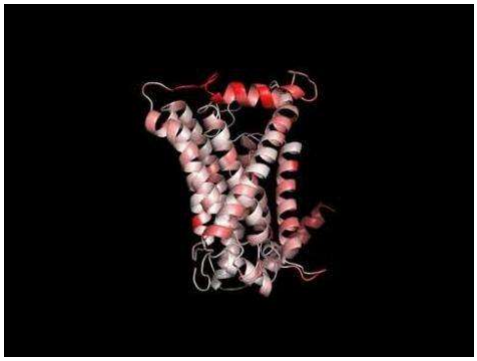

Movie B3a. Mode 0 of the 20-30ns window of the 60ns MD run.

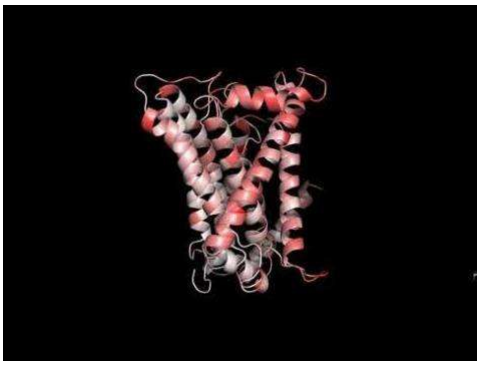

Movie B3b. Mode 2 of the 20-30ns window of the 60ns MD run.

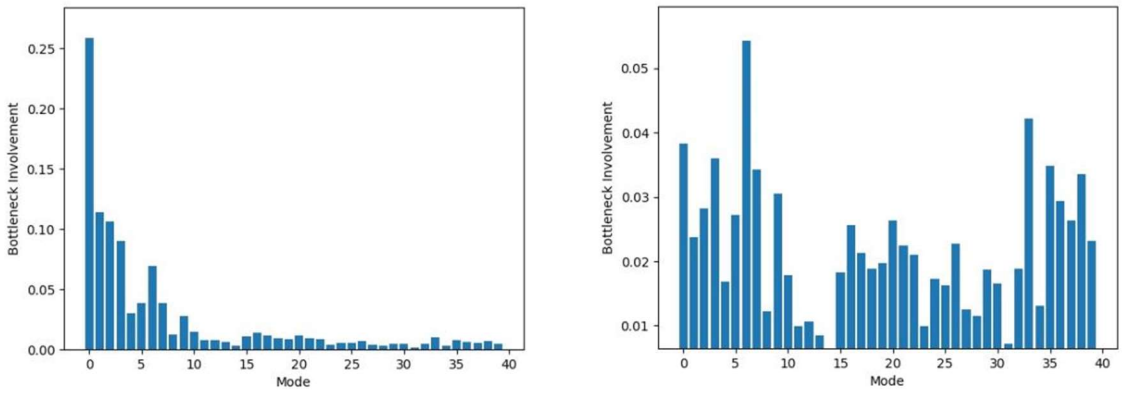

Figure B4. Similar to Fig. B1. Spectrum of bottleneck involvement over first 40 modes of the 50-60ns window of the 60ns run. Mode 0 shows a relatively higher bottleneck involvement, which is illustrated in animation/Movie B4.

mode	eigenvalues (A^2)	spring constants (KJ/mol/A^2)	effective masses (g/mol)	angular frequencies (rads/s)	frequencies (Hz)	periods (s)
0	2.69E+02	9.07E-03	111.87	9.00E+10	1.43E+10	6.98E-11
1	1.92E+02	1.27E-02	111.19	1.07E+11	1.70E+10	5.88E-11
2	1.49E+02	1.63E-02	116.04	1.19E+11	1.89E+10	5.30E-11
3	1.00E+02	2.44E-02	112.48	1.47E+11	2.34E+10	4.27E-11
4	7.07E+01	3.45E-02	113.26	1.74E+11	2.78E+10	3.60E-11
5	5.60E+01	4.35E-02	113.62	1.96E+11	3.11E+10	3.21E-11
6	5.08E+01	4.79E-02	115.33	2.04E+11	3.24E+10	3.08E-11
7	4.48E+01	5.44E-02	111.48	2.21E+11	3.51E+10	2.85E-11
8	4.06E+01	6.01E-02	114.56	2.29E+11	3.64E+10	2.74E-11
9	3.67E+01	6.64E-02	117.52	2.38E+11	3.78E+10	2.64E-11

Table B4. PCA analysis of the 50-60ns window of the 60ns MD run. The periods are close to the periods of the 1ns and 3ns runs. There is a gradual decline in eigenvalues across the first 10 modes comparing to the 20-30ns PCA analysis shown in Table B3.

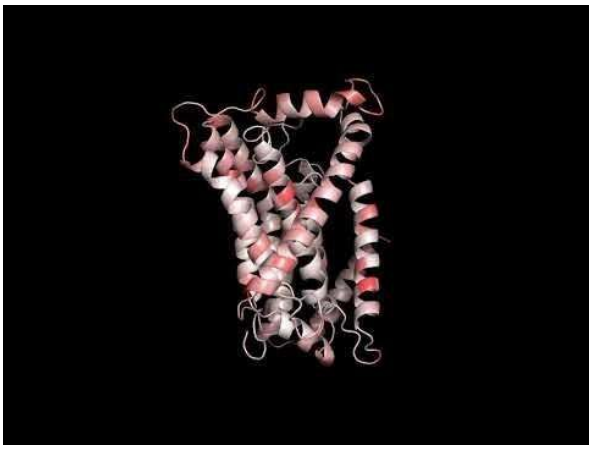

Movie B4. Mode 0 of the 50-60ns window of the 60ns MD run.

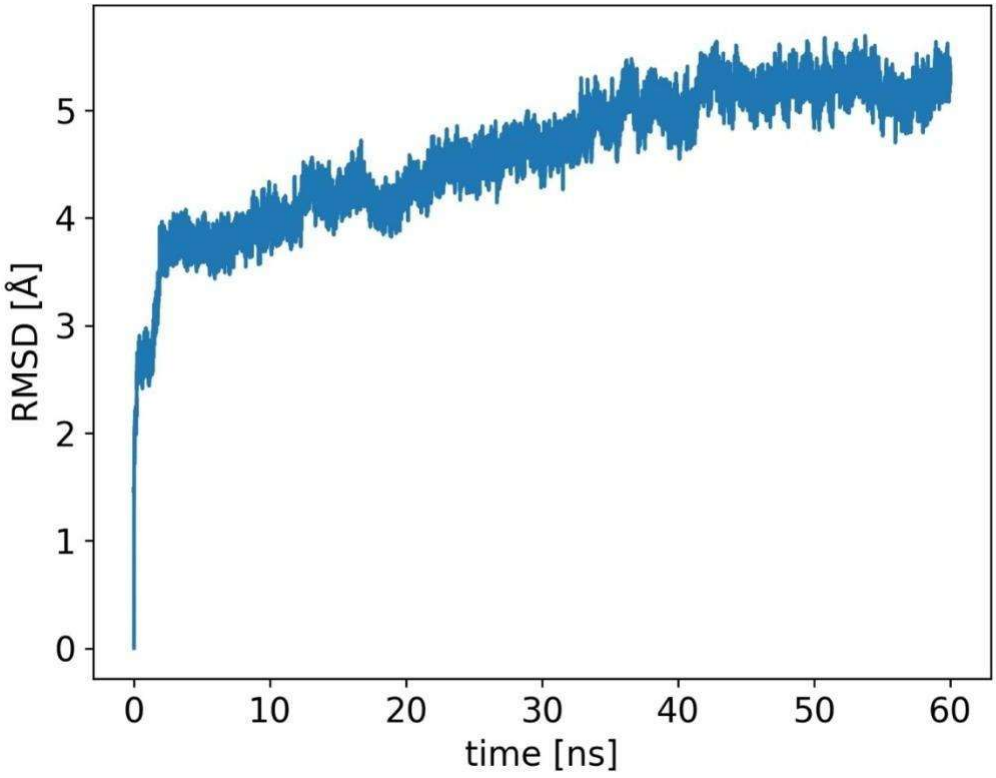

Figure B5. Overall structure expansion of ND1. Shown is the root-mean-square deviation (RMSD) in a 60ns MD simulation of chain H. From the starting point to 1ns, the RMSD increased from 0 Å to 2.6 Å. Another sharp increase happens from 3ns to 4ns, where RMSD increased from 2.6 Å to 3.7 Å. Then the RMSD slowly grows from 3.7 Å to 4.7 Å during the 10ns to 60ns period. From 10 to 40 ns, the drift is mainly due to drift in the center of mass, which was fixed in the segment 40 to 60ns. The PCA modes are adjusted along the trajectory as shown in the above data, B1-B4.

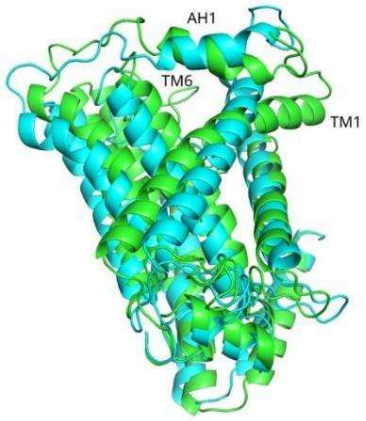

Figure B6a. Details of the expansion. Crystal structure (green) vs. structure after 1ns (cyan) of MD simulation. TM1 straightens up as AH1 bends upwards. TM2 and TM6 shift to the left.

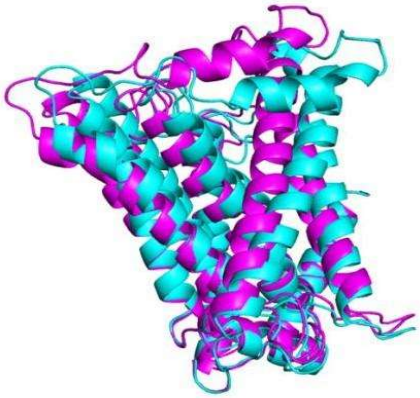

Figure B6b. structure after 1ns (cyan) vs. structure after 20ns (magenta) of MD simulation. AH1 continues to shift upward while TM1 shifts to the left. TM2 and TM6 slightly move to the left.

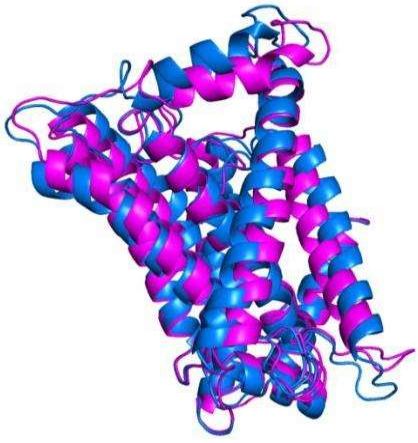

Figure B6c. structure after 20ns (magenta) vs structure after 50ns (navy blue) of MD simulation. AH1 continues to move upwards. TM1, TM2 and TM6 remain relatively stationary comparing to AH1.

Methods: MD Simulations

Coarse Grained Simulations

The Coarse Grained (CG) simulations were performed using Martini force field [1-3] and GROMACS simulation package. Setting up the coarse-grained protein simulation was done by converting the atomistic protein structure (pdb code 4HEA) into a coarse-grained model and generating suitable Martini topology by python script "martinize.py" (part of the Martini tool kit). The insertion of the protein into lipid membrane and solvation in water was done by another Martini tool "insane.py" and GROMACS utility "solvate". Our complex-I model includes subunits 4, 5, 6, 9, W, A and H. The iron-sulfur clusters were converted to a single sphere with a charge of -2 (oxidized state).

Keeping in line with the overall Martini philosophy, the coarse-grained protein model groups 4 heavy atoms together in one coarse-grained bead. Each residue has one backbone bead and zero to four side-chain beads depending on the residue type. In addition to bead representation of amino acids in protein simulations Martini Method implies application of elastic networks (distance restrains between certain multiple backbone beads within the same subunit). These restraints preserve the protein secondary structure from unfolding due to approximate nature of interactions in the coarse-grained force field. The elastic network restrains, however, are not applied between subunits, i.e. mutual dynamics of subunits in the complex-I is free. This standard for protein simulations Martini protocol is used in the present work unless otherwise is explicitly stated. We also performed one PCA test for the model in which some elastic network restraints were removed within subunit H in order to study the effect of conformational changes that involve changes in the secondary structure. More specifically in this test the elastic network restraints were removed between loops and helices AH1, TM1, TM2, TM6 and all within TM1.

In the CG simulations the time step 20 fs (which is a part of the CG force field) was used. The van der Waals interactions are smoothly shifted to zero between 0.9 and 1.2 nm, adhering to the standard Martini protocol. The electrostatic interactions are treated by the reaction-field method with the dielectric constant $\varepsilon_r = 15$ and are smoothly shifted to zero between 0.0 and 1.2 nm as recommended in ref [4]. The neighbor list of 1.4 nm is updated every 10 steps. Pressure (1 bar) and temperature (298.15 K) coupling parameters, τ_t and τ_p, are set to 1.0 and 12.0 ps. The length of simulations for different runs is specified explicitly for each test and varies from 10 to 100 μs.

All-atomic Bottleneck Opening simulations

Here we use GROMACS[5] simulation package with CHARMM36[6] forcefield. The initial coordinates of H-subunit were extracted from the whole structure 4HEA of *T. thermophilus*[7]; all charged residues were neutralized to emulate counter-ions of the solvent and those of the salt-bridges (indeed most charged residues of ND1 have salt-bridge counter-ions; however, different charge-schemes were also explored with similar qualitative results), and the structure was placed in a simulation box filled with artificial hydrophobic medium of Lennard-Jones spheres at ambient temperature of 310 Kelvin. The medium was also modeled using tip3p water, with the same qualitative results for PCA modes. The solvation of structure was then energy minimized with all H-subunit atoms restrained (with 5000 kJ/mol/nm^2 force constant) to preserve the original structure. The structure was then

simulated under periodic boundary conditions and stochastic dynamics[8, 9] to maintain temperature 310 Kelvin. The time step was 1fs, and τ_t was 2 ps. The Canonical ensemble (NVT) is used in these simulations. In the NVT simulations, only the terminal residues of H-subunit - 2, 3, 4, 5, 352, 353, and 354 were restrained with 500kJ/mol/nm^2 force constants and all other atoms were free. The van der Waals interactions were treated with Verlet [10] cut-off scheme with Verlet buffer tolerance of 0.005 KJ/mol/ps per atom and van der Waals cut-off of 1.2 nm. The electrostatics were handled by Particle-Mesh Ewald[11] with a Fourier spacing of 0.12 nm and a PME order of 4.

Up to 100ns trajectories were generated using the methods above. (The longer trajectories were not needed in our study.) The RMSD for a trajectory was generated using the GROMACS rmsd utility. The center of mass rotation and translation were removed.

Pulling Simulations

UQ/DQ/MQ Models:

The ubiquinone model UQ10 was generated using Swiss Param. The DQ/MQ and shorter tail and reduced analogues were all based on this model. To create UQ1 and UQ3 models, the UQ10 model was shortened by cutting of the tails to have either 1 or 3 isoprenoids, and a hydrogen placed where the tail was cut. The reduced models were created by taking the oxidized models and converting the ketones to enols in the headgroups. Specifically, hydrogens were bonded to the oxygens with bond length 0.096nm and strength of other single bonds in the forcefield, a bond angle of 108 degrees and force constant of 543.920 KJ/mol/rad^2. For each hydrogen, 2 proper dihedral angles (corresponding to the 2 carbons connected to the enol carbon) were added with dihedral angles of 180 degrees (trans), force constant of 4.142 KJ/mol and multiplicity of 2. Carbon-carbon single and double bonds in the ring of the head group were then shifted to match the standard ubiquinol structure using existing carbon-carbon single and double bond parameters in the headgroup. The MQ models were created by taking the corresponding UQ models, removing the methoxy groups and adding a ring corresponding to the head group of the standard menaquinone structure using the parameters that already existed in the model for similar bonds, angles, and dihedrals. The DQ models were made from the corresponding UQ models, replacing the isoprenoid tails with a simple saturated hydrocarbon chain, once again using the parameters that already existed in the model for corresponding bonds, angles, and dihedrals.

Simulations within the membrane:

The structure was constructed using charm GUI[12-14] using 4HEA (keeping chain D, F, G, I and P), POPC lipid (315 upper leaflet, 300 lower leaflet). Pre-MD equilibration was done using energy minimization, followed by NVT equilibration at 310 Kelvin, then NPT equilibration at 310 Kelvin and 1 bar. The Berendsen[15] thermostat and the Berendsen barostat were used to maintain temperature and pressure. These were maintained while pulling the quinone through the bottleneck. The Coulomb and LJ interactions have a cutoff radius of 1.2 nm.

Three trajectories were generated using GROMACS 2020. The pulling rate of the three

trajectories are 0.01 nm/ps, 0.01 nm/ps and 0.02 nm/ps respectively. The simulation time is 300 ps, 300 ps and 180 ps respectively. The pulling force constant for all three trajectories is 2500 kJ/mol/nm^2.

Simulations with hydrophobic medium:

The models of bottlenecks were taken from the crystal structures and neutral charge states chosen for all residues so that the bottleneck had zero net charge. The bottleneck models were placed into artificial hydrophobic media of LJ spheres, equivalent to tip3p water with all charges set to zero. The system was then energy minimized with the bottleneck model positions restrained with 2500 KJ/mol/nm^2. The pulling simulations were then done with NVT using stochastic dynamics at 310 Kelvin.

Ligand	Bottleneck	Sim. Length	# runs
UQ1	t. Thermophilus	1.5 ns	53
UQ1H2	t. Thermophilus	1.5 ns	59
UQ3-tail	t. Thermophilus	1 ns	29
UQ3	ovine	1.5 ns	15
UQ3	human	2 ns	15
UQ3	y. Lipolytica	2 ns	15
UQ3H2	y. Lipolytica	2 ns	15
MQ1	t. Thermophilus	1.5 ns	31
MQ1H2	t. Thermophilus	1.5 ns	30
DQ1	t. Thermophilus	1.5 ns	31
DQ1H2	t. Thermophilus	1.5 ns	31

Table B5: List of all pulling simulations through simplified bottleneck in hydrophobic media. Data shown to demonstrate statistical averaging over trajectories used in free energy calculations.

Barrier Simulations

The MD simulation details are the same as in Appendix A. of main text. Briefly, the protein was incorporated into POPC membrane. The quinone was placed near the entrance of Complex I, and after equilibration, was pulled into and then out of the quinone cavity. The energy and the pulling force were measured along the pulling trajectory. Both ubiquinone and menaquinone with various tail lengths were simulated, see details in Appendix A.

To improve statistics, focused MD simulations on a restricted system that involved only the residues of the bottleneck (Fig. 4.1 of the main text) were used. In this case the simulation box was filled with an artificial hydrophobic (LJ) medium. Typically, Q was pulled with a speed of 0.1 Å per ps; this is about ten times slower than the rate of water molecule diffusion in bulk water (D_w=10^{-5} cm^2/s). In a focused MD the pulling speed was further reduced by a factor of ten to simulate adiabatic conditions for free energy evaluation.

Thermodynamic work to cross the bottleneck

Using pulling trajectories, we calculated the Helmholtz work (or Helmholtz free energy, W) to cross the bottleneck. The work is defined by the average force needed to pull the quinone through the bottleneck along the pulling coordinate λ:

$$\left(\frac{\partial W}{\partial \lambda}\right)_T = < F > \tag{B.1}$$

$$\Delta W = \int_{(i)}^{(f)} < F > d\lambda$$

The above relations assume a reversible or quasi-equilibrium (in practice very slow) change of the system. For this reason, the pulling rate was set to 0.01 Å per ps, which is about hundred times slower than the diffusion rate of water. The force <F> is assumed to be averaged over thermal fluctuations (for a given λ , and over a set of initial conditions in the initial state (i)). In our calculations, the pulling force F(t) is measured along the MD pulling trajectory and averaged locally (moving average) over a short interval of 100 ps, for a typical pulling trajectory of some 1500ps. In addition, the averaging was done over some 30 to 60 pulling trajectories with different initial conditions. The Helmholtz work ΔW gives the energy barrier along the trajectory.

When the final state of quinone (f) is defined as a region at the top of the barrier, i.e. the position of the quinone head group inside the bottleneck, and the initial state (i) is a region inside the Q-chamber, the work described above is related to both decrease of entropy (as in isothermal contraction of gas) and increase of potential (elastic) energy of the system due to possible structure adjustment of putting the oversized quinone head group into a relatively narrow bottleneck of the cavity entrance.

In addition, we calculated so-called Jarzynski Averaged (JA) work

$$< \Delta W >= -RTln\left(e^{-\frac{\Delta W}{RT}}\right) \tag{0.2}$$

where Δw is the work for a given pulling trajectory, and the averaging (indicated by the brackets) is assumed over different trajectories. If the pulling work were calculated for a non-equilibrium process at constant energy, instead of constant temperature and quasi-equilibrium process considered here, the Jarzynski equality (JE) would give the proper free energy change. Here the conditions are different from what is assumed in the JE, and thus the above relation is not directly applicable; however, we found it useful to consider this type of averaging as it emphasizes trajectories with minimal work and thus selects (or filter out) the “optimal” trajectories. JA is sensitive to qualitative changes along the trajectory,

such as the entrance of the headgroup into the bottleneck or the passage of individual methyl groups of isoprenoid tail of ubiquinone, which show up as small bumps on the JA curves.

1. Marrink, S.J., et al., The MARTINI force field: coarse grained model for biomolecular simulations. J Phys Chem B, 2007. 111(27): p. 7812-24.

2. Marrink, S.J.F., M.; Risselada, H. J.; Periole, X. , In Coarse Graining of Condensed Phase and Biomolecular Systems, in The MARTINI Force Field, G.A. Voth, Editor. 2009, CRC Press , 2009: Boca Raton, FL.

3. Periole, X.M., S. J., The Martini Coarse-Grained Force Field, in Biomolecular Simulations: Methods and Protocols, E.S. Luca Monticelli, Editor. 2013, Springer International Publishing.

4. de Jong, D.H., et al., Martini straight: Boosting performance using a shorter cutoff and GPUs. Computer Physics Communications, 2016. 199: p. 1-7.

5. Abraham, M.J., et al., GROMACS: High performance molecular simulations through multi-level parallelism from laptops to supercomputers. SoftwareX, 2015. 1-2: p. 19-25.

6. Huang, J. and A.D. MacKerell, Jr., CHARMM36 all-atom additive protein force field: validation based on comparison to NMR data. J Comput Chem, 2013. 34(25): p. 2135-45.

7. Baradaran, R., et al., Crystal structure of the entire respiratory complex I. Nature, 2013. 494(7438): p. 443-8.

8. Van Gunsteren, W.F. and H.J.C. Berendsen, A Leap-frog Algorithm for Stochastic Dynamics. Molecular Simulation, 2007. 1(3): p. 173-185.

9. Goga, N., et al., Efficient Algorithms for Langevin and DPD Dynamics. J Chem Theory Comput, 2012. 8(10): p. 3637-49.

10. Páll, S. and B. Hess, A flexible algorithm for calculating pair interactions on SIMD architectures. Computer Physics Communications, 2013. 184(12): p. 2641-2650.

11. Darden, T.a.Y., Darrin and Pedersen, Lee Particle mesh Ewald: An N·log(N) method for Ewald sums in large systems. The Journal of Chemical Physics, 1993. 98: p. 10089-10092.

12. Jo, S., et al., CHARMM-GUI: a web-based graphical user interface for CHARMM. J Comput Chem, 2008. 29(11): p. 1859-65.

13. Brooks, B.R., et al., CHARMM: the biomolecular simulation program. J Comput Chem, 2009. 30(10): p. 1545-614.

14. Lee, J., et al., CHARMM-GUI Input Generator for NAMD, GROMACS, AMBER, OpenMM, and CHARMM/OpenMM Simulations Using the CHARMM36 Additive Force Field. J Chem Theory Comput, 2016. 12(1): p. 405-13.

15. Berendsen, H.J.C., et al., Molecular dynamics with coupling to an external bath. The Journal of Chemical Physics, 1984. 81(8): p. 3684-3690.